



Review

2D MOFs and their derivatives for electrocatalytic applications: Recent advances and new challenges



Liyuan Xiao, Zhenlu Wang*, Jingqi Guan*

Institute of Physical Chemistry, College of Chemistry, Jilin University, 2519 Jiefang Road, Changchun 130021, PR China

ARTICLE INFO

Article history:

Received 6 April 2022

Accepted 8 August 2022

Available online 19 August 2022

Keywords:

Metal-organic framework

Hydrogen evolution reaction

Oxygen reduction reaction

Carbon dioxide reduction reaction

Nitrogen reduction reaction

ABSTRACT

Metal organic frameworks (MOFs) are promising electrocatalysts due to their high porosity, large specific surface area and adjustable structure. Especially, two-dimensional (2D) MOFs with ultra-thin structure provide more active sites and shorter diffusion distance for heterogeneous catalytic reactions. However, the poor conductivity and poor stability of 2D MOFs impede their practical electrocatalytic applications greatly. Therefore, 2D MOF-derived transition metal carbides, sulfides, phosphides, oxides, and single-atom catalysts have been fabricated by carbonization, vulcanization, phosphorization or oxidation strategies, which improve the conductivity and stability significantly. Here, the synthesis strategies of 2D MOFs and their derivatives are summarized, and the factors affecting the geometries and electronic structures of active sites are commented in detail. The electrocatalytic applications of 2D MOFs and their derivatives in oxygen evolution reaction (OER), hydrogen evolution reaction (HER), oxygen reduction reaction (ORR), carbon dioxide reduction reaction (CO₂RR) and nitrogen reduction reaction (NRR) are reviewed. The effect of the geometric construction and electronic configuration of active sites (including metals, nonmetals, and defects) of 2D MOFs and their derivatives on the electrocatalytic performance is detailedly discussed by combining experimental achievements and theoretical analysis. Finally, the development prospects and challenges of 2D MOFs and their derivatives are proposed.

© 2022 Elsevier B.V. All rights reserved.

1. Introduction

Metal-organic frameworks (MOFs) are a kind of porous materials that combine organic and inorganic components by coordination bonds, presenting an infinite network structure of one, two, and three dimensions in space [1]. In recent years, MOFs have received extensive attention in gas storage and separation [2–4], catalysis [5–9], lithium metal batteries [10], and magnetic and molecular recognition [11–13]. MOFs are promising electrocatalysts [7], and their advantages are mainly manifested in the following aspects. First, the highly ordered periodic arrangement of massive cells favors the creation of pores [14], and thus MOFs have the advantages of high porosity and large specific surface area. Secondly, the unique structure of MOFs and the densely distributed metal nodes are helpful to improve electrocatalytic activity. Finally, the active sites of MOFs are generally metal units, which can be periodically arranged to make the active sites dispersed uniformly [15]. The pore size of most bulk MOFs is very small, which makes the mass transfer slow and affects the charge transfer process.

Inspired by 2D materials such as graphene and graphdiyne [16], 2D MOFs have been fabricated, which not only give full play to the advantages of MOFs in the field of electrocatalysis, but also help to overcome the shortcomings of massive MOFs to some extent. After exfoliation, 2D MOFs have higher electrocatalytic activity than massive MOFs because they have larger specific surface area and more active sites, which are conducive to improving the electrocatalytic performance [17,18]. Additionally, the ultra-thin structure of 2D MOFs favors exposing rich redox-active centers and shortening the diffusion distance, which is conducive to improving the ion and electron transfer rate in the electrocatalytic process. Moreover, the conductivity of traditional bulk MOFs is poor. In contrast, 2D MOFs have ultra-thin porous structure, which can increase the carrier concentration and improve the conductivity. Furthermore, the tortuous channels of bulk MOFs hinder the exposure of active sites, and reduce the contact between active centers and reactants, while rapid mass transfer of reactants and products can be achieved in 2D MOFs. In addition, the structure can be adjusted by modulating metal nodes and organic ligands [19–21]. Metal ions with ideal oxidation state are realized in 2D MOFs by regulating organic ligands. Cui et al. prepared 2D NiFe-DOBDC (H₄DOBDC = 2,5-dihydroxyterephthalic acid) (NiFe-MOF-74) ultrathin nanosheets array on NF [22]. This 2D fold sheet structure helps to expose more

* Corresponding authors.

E-mail addresses: wzl@jlu.edu.cn (Z. Wang), guanjq@jlu.edu.cn (J. Guan).

active sites, and provides rich defects. In 1 M KOH, the overpotential at a current density of 20 mA cm^{-2} (η_{20}) on NiFe-DOBDC-74 was 240 mV, which was smaller than that of Ni-DOBDC-74 (278 mV), Fe-DOBDC-74 (260 mV) and RuO_2 (315 mV). In addition, the charge transfer resistance (R_{ct}) of NiFe-DOBDC-74 was 42.32Ω , which was smaller than that of Ni-DOBDC-74 (211.7Ω) and Fe-DOBDC-74 (160.5Ω), indicating that NiFe-DOBDC-74 had higher conductivity and faster proton discharge kinetics.

Although 2D MOFs have great advantages over many other electrocatalysts, they also have some disadvantages, such as poor conductivity and poor stability, which will affect their electrocatalytic applications [17]. To overcome the shortcomings, researchers generally convert 2D MOFs materials into their derived transition metal sulfides, phosphating compounds, selenides, transition metal carbides, transition metal oxides and single metal atoms supported on carbon-based nanosheets [18]. The derived carbon-based nanosheets can enhance the conductivity, while the formed transition metal sulfides, phosphides and selenides can increase electrocatalytic activity and stability. Transition metal oxides have excellent electrocatalytic stability and high electrocatalytic tolerance. The single-atom electrocatalysts supported by carbon-based materials can reduce electron transfer resistance and enhance the electrocatalytic efficiency.

Compared with traditional bulk MOFs, 2D MOFs derived metal/carbon composites, metal oxides, metal sulfides and metal phosphates can not only retain the unique 2D structure, high specific surface area and high porosity of the precursors, but also increase the conductivity and the charge transfer. Since the channels of MOFs would collapse during high-temperature annealing process, the metal species will congregate [23]. Compared with 3D MOF-derived materials, the aggregation of metal species in 2D MOF-derived materials can be better inhibited due to spatial isolation effect [24,25]. Thus, 2D MOFs derivatives have higher specific surface area, more active sites, faster mass transfer rate and better conductivity. Li et al. chose 1D Co-BTC (BTC = 1,3,5-benzenetricarboxylic acid), 2D Co-BDC (BDC = 1,4-benzenedicarboxylic acid) and 3D Co-DHTP (DHTP = 2,5-dihydroxyterephthalate) to obtain 1D $\text{Co}_3\text{O}_4/\text{C}_{\text{BTC}}$, 2D $\text{Co}_3\text{O}_4/\text{C}_{\text{BDC}}$ and 3D $\text{Co}_3\text{O}_4/\text{C}_{\text{DHTP}}$ by pyrolysis method [26]. They found that 2D $\text{Co}_3\text{O}_4/\text{C}_{\text{BDC}}$ had smaller Co_3O_4 nanoparticles than 3D $\text{Co}_3\text{O}_4/\text{C}_{\text{DHTP}}$, which may be due to the 2D interlayer limiting the aggregation of nanoparticles, thus exposing more active sites. In addition, 2D $\text{Co}_3\text{O}_4/\text{C}_{\text{BDC}}$ inherited the 2D structure of the precursor, and its specific surface area was $181.9 \text{ m}^2/\text{g}$, which was higher than 1D $\text{Co}_3\text{O}_4/\text{C}_{\text{BTC}}$ ($75.6 \text{ m}^2 \cdot \text{g}^{-1}$) and 3D $\text{Co}_3\text{O}_4/\text{C}_{\text{DHTP}}$ ($98.7 \text{ m}^2 \cdot \text{g}^{-1}$). In 1.0 M KOH, 2D $\text{Co}_3\text{O}_4/\text{C}_{\text{BDC}}$ exhibited an OER overpotential of 208 mV (η_{10}), lower than 1D $\text{Co}_3\text{O}_4/\text{C}_{\text{BTC}}$ (295 mV) and 3D $\text{Co}_3\text{O}_4/\text{C}_{\text{DHTP}}$ (260 mV). 2D array structure can help the formation of $\cdot\text{OH}$ intermediate, thus promoting the first step of OER.

2D MOFs and their derived 2D materials have been rapidly developed and applied in the electrocatalytic hydrogen evolution reaction (HER) [27–29], oxygen evolution reaction (OER) [30–32], oxygen reduction reaction (ORR) [33,34], CO_2 reduction reaction (CO_2RR) [35–37] and nitrogen reduction reaction (NRR) [38,39]. Water electrolysis can be used for large-scale production of hydrogen [40]. Renewable energy such as solar energy and wind energy can be converted to clean hydrogen energy, which is a sustainable production model. Water electrolysis mainly includes two semi-reactions, namely OER and HER. For the HER, as early as 2011, Nohra et al. reported that polyoxometalate-based MOFs (POMOFs) showed HER activity, and later researchers made many explorations on MOF-based HER electrocatalysts [41]. The introduction of other metal elements into single-metal MOFs can adjust the original electronic structure and optimize the catalytic activity. In 2018, Lu et al. prepared a NiFe- $\text{H}_2\text{BDC-NH}_2$ ($\text{H}_2\text{BDC-NH}_2$ = 2-amino terephthalic acid) [42], which showed excellent HER catalytic

activity with an overpotential (η_{10}) of only 79 mV at $10 \text{ mA} \cdot \text{cm}^{-2}$. They also synthesized a bimetallic FeNi(BDC)(DMF, F)/NF (DMF = N, N-dimethylformamide, NF = nickel foam) with outstanding OER and HER activity [43].

2D MOFs have been used as templates to prepare 2D carbon-based materials to improve the electrocatalytic activity of HER. Wang et al. synthesized $\text{Co}_2(2\text{-Melm})$ (2-Melm = 2-methylimidazole) nanosheets and then sulfurized them to form N- CoS_2 @NC/Ti. After sulfurization, the N content in CoS_2 @NC increased, and there were many types of Co- N_x species, which could regulate the electronic structure of Co sites, thus showing high HER activity [44]. Zhang et al. prepared CoFeP TPAs/Ni (TPAs = triangular plate arrays) with excellent stability [45]. Xu et al. used 2D $\text{Ni}_2\text{-(bdc)}_2\text{ted}$ (bdc = 1,4-benzenedicarboxylic acid; ted = triethylenediamine) as the precursor to prepare nitrogen-doped graphene-shell Ni nanoparticles (Ni@NC) by high-temperature annealing in a nitrogen atmosphere. By adjusting the annealing temperature, the obtained Ni@NC-800 had high stability and tolerance to HER in an alkaline solution [46]. 2D MOFs and their derivatives are widely used in the field of water electrolysis, and through the regulation of their structures, the active surface area can be increased by the construction of hollow/porous structures and self-supporting structure. In addition, single-atom structure can be fabricated to enhance the density of active sites, thereby enhancing HER catalytic activity [47]. Zhou et al. studied the catalytic activity of several metal atoms immobilized on C_9N_4 for the HER by calculating the Gibbs free energy (ΔG_{H^+}) of hydrogen adsorbed on different metal sites [48]. The calculated ΔG_{H^+} is shown in Fig. 1a. The ΔG_{H^+} (N) values of Co-, Ni- and Pt-based catalysts are close to zero, indicating that the N atoms in these systems can adjust the electronic structure of metal sites for promoting HER. For OER, it belongs to a four-electron transfer process, and the required overpotential is large and the kinetics is slow, which is the key step in electrocatalytic water splitting. Whether in acidic or alkaline media, OER involves OH^* , O^* and OOH^* intermediates, and the OER activity depends largely on the surface binding energy of these intermediates. At present, the commercial OER catalysts are mainly IrO_2 and RuO_2 . IrO_2 has a strong binding force with oxygen intermediates [49,50], while RuO_2 has a weak binding force with oxygen intermediates [51,52]. Since Ir and Ru are precious metals, they cannot be used on a large scale due to their high cost and scarcity. From Fig. 1b, the OER activity of Co_3O_4 is comparable to that of noble metal oxides, which provides a possibility to substitute noble metals [53,54]. Adjusting the metal center and ligand components of 2D MOFs can optimize the electronic configuration of the catalyst, promote the adsorption of the intermediate in the rate-limiting step, and achieve fast electron transfer, thus improving the intrinsic activity, which mainly includes the regulation of metal centers and ligands. Pang et al. synthesized ultrathin single-metal 2D $\text{Co}_2(\text{OH})_2\text{BDC}$ nanosheets, showing a low overpotential (η_{10}) of 263 mV [55]. Zhu et al. prepared bimetal 2D Ni (Fe)-BDC nanosheets [56]. The strong coupling effect of Fe and Ni made them exhibit high OER activity. Organic ligands can effectively regulate the electronic structure of metal centers, and improve the conductivity of MOFs. Li et al. obtained 2D CoBDC-Fc by replacing BDC ligand with carboxyl ferrocene (Fc) by ligand-deficient method, which produced unsaturated Co sites and tuned the coordination environment of metal centers [57]. Du et al. prepared a new 2D $[\text{Ni}_3(\text{C}_{32}\text{H}_{16}\text{N}_{16})_n]$ (NiPc-MOF) based on nickel phthalocyanine [58], and found that the ligand in NiPc-MOF can improve the conductivity, which is helpful for electron transfer in the OER process. By controlling the composition of precursors and heat treatment, the composition and structure of MOF derivatives can be controlled, thus effectively improving the catalytic performance. Zhao et al. prepared N-, O-, and S- doped Co_9S_8 nanoparticles with enhanced conductivity and improved charge transfer ability [59].

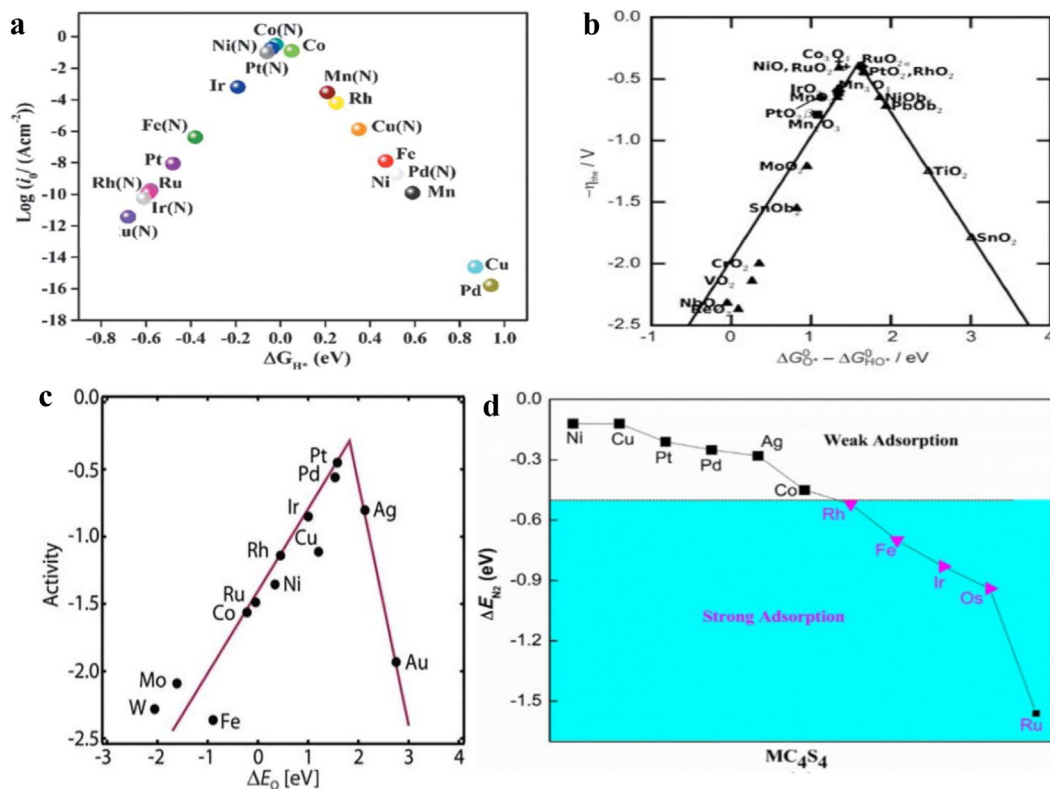


Fig. 1. (a) HER volcano curve. Reproduced with permission from ref. [48]. Copyright 2019, Royal Society of Chemistry. (b) Volcano plot of OER overpotential. Reproduced with permission from ref. [54]. Copyright 2019, Wiley-VCH. (c) Trends in oxygen reduction activity. Reproduced with permission from ref. [62]. Copyright 2020, Elsevier Ltd. (d) The adsorption energies of N₂ molecule. Reproduced with permission from ref. [74]. Copyright 2019, Elsevier Ltd.

More exploratory studies found that transition metal oxides exhibit high electrocatalytic activity for the OER. Hu et al. used Ni-C₈H₆O₄ (C₈H₆O₄ = terephthalic acid) as the precursor and calcined it at 250 °C to obtain ultra-small NiO nanoparticles (NPs). The oxygen vacancy in ultra-small NiO NPs can optimize the adsorption energy of OER intermediates [23]. Wu et al. prepared Co-Fe-P-Se nanoparticles on nitrogen-doped carbon (NC) [60]. The three-dimensional structure assembled by nanosheets is beneficial to the infiltration of electrolytes and provides a rich channel for the diffusion of reaction products. Since MOF crystals have the characteristics of highly ordered and uniform distribution of metal centers, they are considered ideal precursors for the preparation of single-atom catalysts (SACs) with high-density M-N_x-C_y active sites. Zang et al. prepared single-atom Co wrapped in nitrogen-doped carbon, which had high atomic utilization and thus showed low OER overpotential [61].

Oxygen reduction reaction (ORR) occurs mainly on the cathode of electrochemical devices such as fuel cells and metal-air batteries, and the ORR performance determines the energy conversion efficiency of such devices to a large extent. Density functional theory (DFT) calculations showed that Pt electrocatalysts have the highest catalytic activity for ORR (Fig. 1c) [62]. To reduce the over-reliance of noble metal-based ORR electrocatalysts, many researchers have turned to seeking cheap and readily available electrocatalysts with excellent performance, and 2D MOFs and their derivatives are one of the most concerned electrocatalysts [63,64]. 2D MOF nanosheets containing transition metals such as Fe, Co, Ni, and Cu showed unique advantages for catalytic ORR [65,66]. In 2016, Miner et al. designed conductive Ni₃(HITP)₂ (HITP = 2, 3, 6, 7, 10, 11-hexaiminotriphenylene) as the ORR catalyst, which had an initial potential of 0.82 V and high stability [64]. Peng et al. synthesized a series of bimetallic M₃HITP₂ (M = Ni, Co)

with HITP as the ligand by changing the ratio of Ni/Co and found that Co₃HITP₂ exhibited the best ORR activity [67]. However, MOFs usually have low conductivity, which is not conducive to electrocatalytic applications. The incorporation of conductive materials can overcome the poor conductivity of MOF nanosheets. Wang et al. prepared N-doped nanoporous carbon/graphene nanosheets with sandwich structure, which had a high onset potential of 0.92 V (vs RHE) for the ORR [68].

Electrocatalytic reduction of CO₂ is experimentally carried out in H-type electrolytic cells containing aqueous electrolytes. CO₂ can be converted into valuable chemicals (including C1, C2, and C3 products) by proton-coupled multi-electron transfer mechanisms [69]. The chemical structure of CO₂ molecule is very stable, and the reduction of CO₂ needs to overcome large kinetic and thermodynamic energy barriers. At the same time, the reduction of CO₂ involves multi-electron and multi-proton transfer, and there are many complex intermediates in the electrocatalytic process, which will affect the reaction pathway and the selectivity of products. Therefore, it is necessary to prepare ideal electrocatalysts to solve these issues. MOFs are crystal materials with distinct boundaries. The arrangement of organic ligands and metal nodes is highly periodic. In addition, their physical and chemical properties can be regulated by modulating the compositions, metal nodes, and organic ligands at the molecular level. At the same time, the high specific surface area and rich pore structure provide many active sites for CO₂ adsorption, which is conducive to the activation of CO₂ molecules. These advantages make them attractive in the field of electrocatalytic reduction of CO₂. Majidi et al. reported a 2D conductive MOF-tetrahydroquinoline copper (Cu-THQ) [70]. The average Faraday efficiency (FE) of CO production was 91 %, and the current density was up to 173 mA cm⁻². CO₂ electroreduction usually requires high negative potential, but the stability of

MOFs cannot be guaranteed under this condition. Hence, using MOFs as the precursor to prepare MOF-derived 2D materials is a perfect selection to improve stability. The decomposition of MOFs under controlled conditions usually leads to the aggregation of metal components into small nanoparticles. Cheng et al. prepared a series of CuNP-NC catalysts by annealing Cu-BTC at different temperatures and found that the presence of N-doped carbon supports formed at low temperatures significantly improved the selectivity of ethylene and ethanol in electrocatalytic CO₂RR [71].

As an environmentally friendly energy carrier, NH₃ is widely used in industrial and agricultural production, such as ammonia, dyes, plastics, explosives, agricultural fertilizers, etc. More than 200 million tons of ammonia are annually produced worldwide, 80% of which is used for synthetic fertilizers, making an important contribution to speedy economic development and rapid population growth. NH₃ is also considered an attractive hydrogen carrier (17.6 wt%) because of its high energy density (4.3 kWh·kg⁻¹), non-carbon characteristics, and easy transportation (-33 °C, liquid). NH₃ can be directly produced by using N₂ and water in nature through photocatalytic and electrocatalytic reduction methods [72,73]. Compared with the photocatalytic reduction method, electrochemical nitrogen reduction reaction (NRR) is more effective because it does not involve multiple wavelength changes and rapid carrier recombination. Compared with the traditional Haber Bosch process, the electrocatalytic reduction process can effectively reduce energy consumption and CO₂ emission, and simplify the complexity of the reactor. Therefore, it is urgent to design efficient NRR electrocatalysts to accelerate the reaction. Zhao et al. calculated the adsorption energy of N₂ on MC₄S₄ nanosheets [74]. As shown in Fig. 1d, the adsorption strength of N₂ molecules depends largely on the central metal atoms, and Fe, Os, Ir, and Ru can interact strongly with N₂ [74]. Noble metals are widely used in electrocatalytic nitrogen reduction due to their high coordination surface atomic density, excellent electrical conductivity, and appropriate reactant adsorption capacity. However, the cost of noble metal electrocatalysts is high and the selectivity is poor. Compared with noble metal materials, non-noble metal materials have higher crustal content and have a greater application prospect for the NRR. At present, researchers have developed a variety of NRR electrocatalysts made of Mo, Fe, V, and other metals for artificial electrochemical synthesis of NH₃ under environmental conditions. From an environmental and economic point of view, the use of non-metallic catalysts can reduce costs and avoid residual metal ions.

In this review, we systematically introduce the design and synthesis strategies of 2D MOFs, including top-down and bottom-up methods, and summarize the advantages and disadvantages. Then the factors affecting the electronic structure of active sites and the electrocatalytic performance are discussed. The applications of 2D MOFs and their derivatives in the field of electrocatalysis are classified and summarized. Finally, personal opinions on the electronic structure regulation strategies to improve electrocatalytic performances are proposed, and the future challenges and development prospects in the field of electrocatalysis prospect.

2. Synthesis methods of 2D MOFs and their derivatives

2.1. Synthesis methods of 2D MOFs

2D MOFs have a wide range of potential applications in the field of electrocatalysis, which have attracted more and more researchers' attention. However, there are many issues in the fabrication of 2D MOFs, such as high cost and low yield. How to obtain high-quality MOF nanosheets with low cost and high yield by simple methods is still a great challenge. The preparation methods of 2D

MOFs can be roughly divided into two categories, namely top-down method and bottom-up method [75]. The top-down method is to destroy the weak interaction force between MOF's layers by applying an external force, and 2D MOF nanosheets can be obtained by stripping [18]. The bottom-up method means the direct synthesis of 2D MOFs through the chemical reaction of metal ions and organic ligands. The thickness of 2D MOF nanosheets can be controlled by tuning the reactant concentration and reaction time [18]. The growth of MOFs in the vertical direction should be limited without affecting their growth in the other two directions. The synthesized MOF nanosheets can be identified by scanning electron microscopy (SEM), transmission electron microscopy (TEM), and atomic force microscopy (AFM), by which the morphology, structure, and thickness of 2D MOF nanosheets can be obtained.

2.1.1. Top-down synthesis

Top-down synthesis refers to the stripping of bulk MOFs into 2D nanosheets by physical and chemical means. This kind of synthesis method is suitable for stripping MOFs with a layered structure, and the interlayer forces are weak forces such as hydrogen bonding, van der Waals force, and π - π stacking. When specific chemical treatment or external energy is applied, it is possible to overcome the interlayer forces of MOFs. According to different extraction methods, top-down synthesis can be divided into physical stripping and chemical stripping. Thereinto, the physical stripping method is simple to operate and is a classical method for the preparation of 2D MOFs, including soft physical stripping method and ultrasonic stripping method [76,77]. Chemical exfoliation refers to the destruction of ligand structures by chemical reactions, such as electrochemical exfoliation and intercalation chemical exfoliation [76].

2.1.1.1. Physical stripping. For the physical stripping method, ultrasonic, grinding and other mechanical forces are used to break the weak interlayer interaction (van der Waals force and hydrogen bond), but do not destroy the covalent bond in each layer, so that the structure of each layer can be maintained, which can also be called mechanical stripping method. Ultrasonic stripping is one of the simplest and the most feasible methods to prepare 2D materials, by which the interlayer force can be destroyed because the hole effect will be formed in the process of ultrasonic stripping. Zhao et al. obtained Cu-TCPP nanoplates by simple ultrasonic stripping via the Tindall effect (Fig. 2a) [78]. The Cu-TCPP nanosheets with TCPP ligands are connected to a 'chessboard' structure by four Cu₂(COO)₄ 'paddle wheel' metal nodes. The thickness of the nanocomposites was only 3.4 nm and the nanolayer contained four layers (Fig. 2b-d). Ma et al. synthesized a novel MOF nanosheet based on porphyrin, namely [BMI]₂[Ca₃(H₂TCPP)₂(μ -2-OH)₂(H₂O)₂] (H₆TCPP = *meso*-tetra(carboxyphenyl) porphyrin, BMI = 1-butyl-3-methylimidazolium) [79]. They firstly synthesized the MOF by ionic liquid-assisted synthesis and then obtained nanosheets with a width of 50–100 nm and a length of 100–900 nm by ultrasonic stripping. Single crystal X-ray analysis shows that the MOF crystallizes in triclinic space group Pi. Huang et al. synthesized 2D bimetallic Ni/Fe-BDC by two-step ultrasonic exfoliation, in which Ni-BDC was well retained in bimetallic nanosheets and Fe-BDC was uniformly dispersed [80]. The nanosheets had a specific surface area of 75.3 m²·g⁻¹, a pore volume of 0.19 cm³·g⁻¹, and narrower mesoporous distribution. The exfoliation of lamellar crystals is one of the most direct ways to prepare the ultrathin nanosheets. Tan et al. exfoliated 3D layered porous MOF into monolayer and bilayer nanosheets by ultrasonic exfoliation [81]. The exfoliated 2D MOF crystallizes in the triclinic space group P1, which has similar crystal structure to the unexfoliated 3D MOF. Similarly, Liu et al. prepared single crystal ultrathin 2D MOF

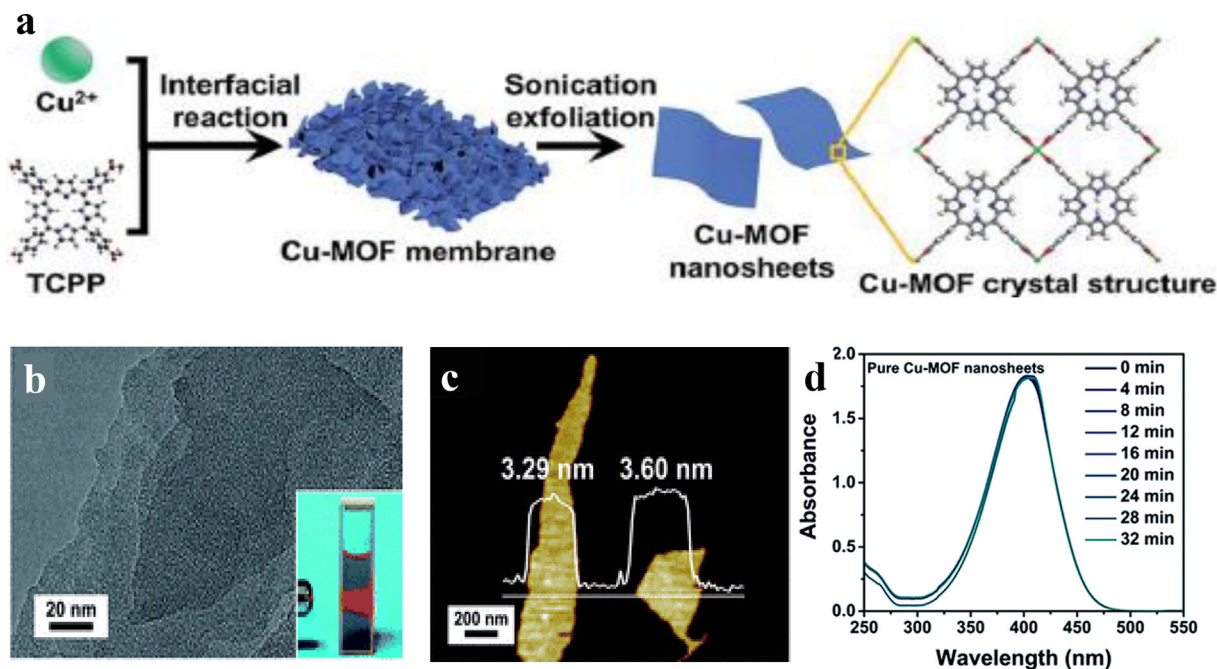


Fig. 2. (a) Synthesis process of Cu-TCPP nanosheets. (b) TEM image and Tyndall effect. (c) AFM image. (d) Time-dependent UV-vis absorption spectra. Reproduced with permission from ref. [78]. Copyright 2019, Royal Society of Chemistry.

nanosheets by ultrasonic exfoliation of layered metals, with a thickness of 6.0 nm (2 layers) and a transverse size of $1.5 \times 3.0 \mu\text{m}^2$ [82]. The advantage of ultrasonic stripping method is a simple operation, but there are many shortcomings. For example, the solvent used directly affects the structure, morphology and thickness of the obtained nanosheets, which is easy to refill between nanosheets. In addition, the yield of this method is low, and cannot be used on a large scale.

In the process of ultrasonic stripping, it is necessary to select appropriate solvents, such as water, methanol, acetone, and tetrahydrofuran, which can give priority to stripping and improve the stability of nanosheets. However, these solvents are easy to volatilize. Researchers have found a molten salt, an ionic liquid, which has little volatility and fine solubility. The ionic liquid can theoretically be used as a solvent to assist the stripping. Liu et al. dispersed $\text{Zn}_2(\text{BIM})_4$ (BIM = benzimidazole) precursor in mixed ionic liquids (pure water, pure [Omic]Cl, methanol, and *n*-propanol) [83]. $\text{Zn}_2(\text{BIM})_4$ nanosheets were obtained by centrifugation, and the suspension showed a Tyndall effect. The monolayer $\text{Zn}_2(\text{BIM})_4$ had a twisted tetrahedral geometry with a layer thickness of approximately 5 Å. The advantages of ionic liquid-assisted exfoliation are easy operation and amplification, but there are disadvantages of low yield and easy refilling.

The shear stripping is carried out by shear force, which is produced by a commercial mixer, and thus the yield is high and it can be used for industrial production. Ying et al. synthesized large blocks of ELM-12 ($\text{Cu}(\text{bpy})_2(\text{OTF})_2$, bpy = 4,4-bipyridine, OTF = trifluorosulfonic acid) and $\text{Zn}_2(\text{BIM})_4$ (Fig. 3a). ELM-12 (Fig. 3b, c) and $\text{Zn}_2(\text{BIM})_4$ (Fig. 3d, e) nanosheets with a thickness of 3–5 nm were obtained by centrifugation in a commercial agitator with four blades [84]. High shear ring microreactor has a high shear rate, which affects the particle size and yield of nanoparticles. Lapkin et al. synthesized original monodispersed CuBDC nanosheets using a high-shear annular microreactor [85]. Later, they studied the influence of different solvents on the structure of CuBDC nanosheets [86]. Due to solvent exchange, 2D CuBDC exhibited branch structure and disordered thin films. The use of high shear ring microreactor makes 2D MOFs easier to synthesize in the lab-

oratory, which is an economical and effective method in industrial-scale manufacturing.

Traditional physical exfoliation such as ultrasonic exfoliation and shear exfoliation can obviously destroy the interaction between layers and even destroy the structure of MOF nanosheets. The soft physical stripping method combining wet ball milling with ultrasonic stripping can reduce the damage to the structure and improve the stripping yield. Additionally, appropriate solvents should be selected, because they can not only promote the exfoliation of MOFs but also stabilize the exfoliated nanosheets. Hence, mixed solvents are generally used. Sun et al. developed a method of soft physical stripping [87]. $\text{Ni}_3(\text{HITP})_2$ nanoparticles were prepared by wet ball milling $\text{Ni}_3(\text{HITP})_2$ powder at a certain speed, then mixed with volatile solvent and peeled off with the aid of an ultrasonic wave. The obtained nanosheets had high crystallinity and leaf shape. Yang et al. synthesized $\text{Zn}_2(\text{BIM})_3$ nanosheets using an improved soft-physical stripping technique [88]. In an isovolumic mixture of methanol and *n*-propanol, small methanol molecules are inserted into the layers of $\text{Zn}_2(\text{BIM})_3$ precursor, destroying the interactions between the layers, while *n*-propanol prevented the nanoparticles from reassembling. Sun et al. synthesized $[\text{Cd}(4,4'\text{-bpy})_2(\text{H}_2\text{O})_2](\text{ClO}_4)_2 \cdot (2,4'\text{-bpy})_2 \cdot \text{H}_2\text{O}$ nanoplates with the thickness of 15–25 nm by a modified soft physical stripping method [89], which have great potential in the field of selective adsorption.

In addition to the above physical exfoliation methods, some other physical exfoliation methods are also suitable for the preparation of 2D MOFs. Coronado et al. used sellotape to peel off layered MOFs [90]. Maeda et al. exfoliated $\text{La}(\text{BTP})$ (BTP = 1,3,5-benzenetriphosphonic acid) by vibration. Zhao et al. reported freezing-thawing extirpation of $\text{Ni}_8(5\text{-BBDC})_6(\mu\text{-OH})_4$ (BBDC = 5-*tert*-butyl-1,3-benzenedicarboxylic acid) [91]. Wang et al. reported the stripping of $[\text{Hphen}]_2[(\text{UO}_2)_2(\text{Ox})_3]$ massive crystals (Phen = 1,10-phenanthroline, Ox = oxalate) by ultraviolet radiation [92].

Layered MOFs have strong coordination bonds in the layer, while van der Waals force or hydrogen bond between layers is weak. Ultrasonic exfoliation, shear exfoliation and soft physical exfoliation can overcome the weak interaction between layers, so

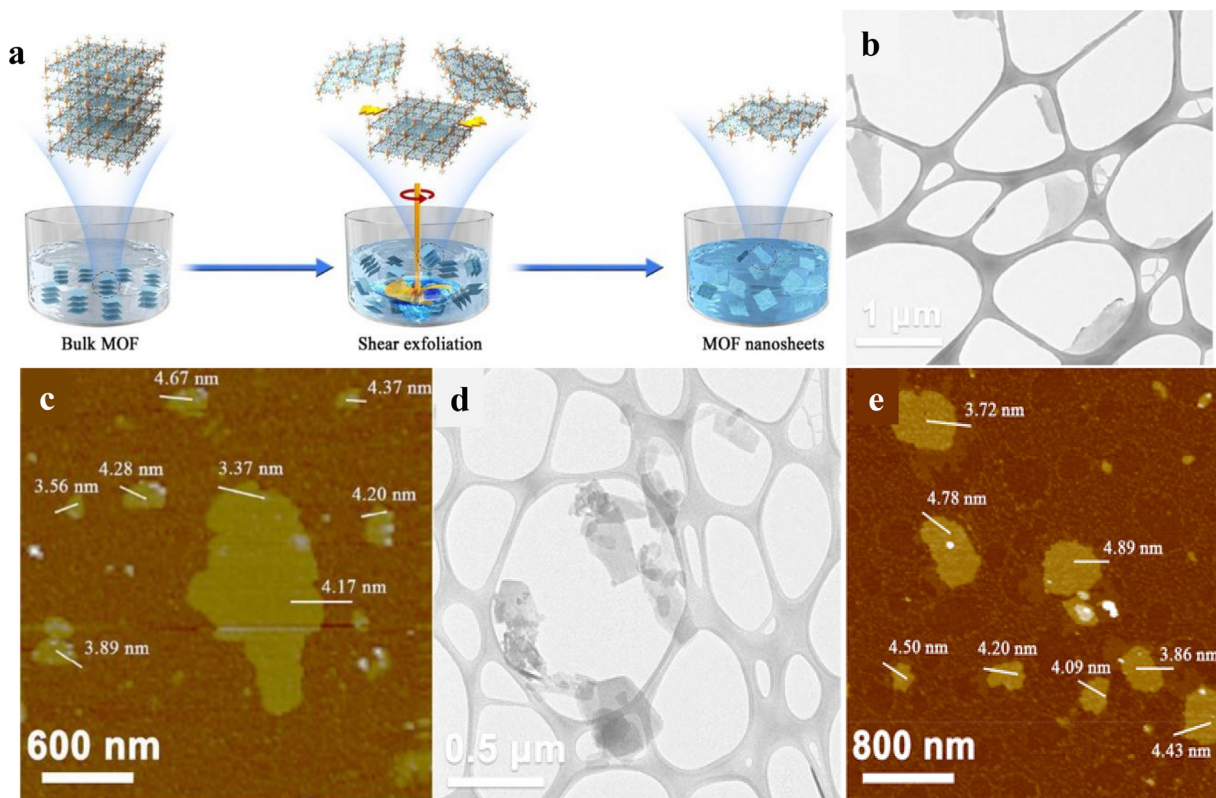


Fig. 3. (a) Schematic diagram of shear stripping process of MOF nanosheets. (b) TEM image and (c) AFM image of ELM-12 nm. (d) TEM image and (e) AFM image of $\text{Zn}_2(\text{BIM})_4$ nanosheets. Reproduced with permission from ref. [84]. Copyright 2020, American Chemical Society.

that layered MOFs are exfoliated. The development of these methods is largely affected by other 2D material synthesis technologies. The top-down method is a simple and practical method to prepare 2D MOFs nanosheets, but there are limitations. For instance, the delamination process will destroy the lamellar crystalline structure of the nanosheets. More importantly, the thickness distribution of the stripped product is uneven and the yield is low, which is difficult to synthesize in large quantities. The top-down synthesis of 2D MOFs still has great room for development, and the related synthesis mechanism and preparation technology still needs further exploration.

2.1.1.2. Chemical stripping. The chemical stripping method is suitable for stripping MOFs containing reactive ligands by destroying the ligand structure through a chemical reaction. Most massive laminated materials have strong intra-planar bonds, but weak interlaminar bonds, which mainly include van der Waals forces and electrostatic interactions [76]. Electrochemical stripping weakens this force, turning lumpy layered materials into single-layer 2D materials. Electrochemical exfoliation includes anode exfoliation and cathode exfoliation, both of which are carried out under mild conditions. The anode exfoliation is carried out in an aqueous solution, while the cathode exfoliation is usually carried out in an organic solution containing alkaline metal ions or quaternary ammonium cations [93].

Under different reaction conditions, pillared and layered MOFs can be peeled off to form 2D coordination layers by destroying interlayer coordination bonds, and some more stable columnar ligands can be selected. Zhang et al. synthesized $(\text{H}_3\text{O})_2[\text{Co}_6\text{O}(\text{DHBDC})_2(\text{H}_2\text{DHBDC})_2(\text{EtOH})_4]\cdot 2\text{EtOH}$ ($\text{H}_4\text{dhbdc} = 2,3$ -dihydroxy-1,4-benzenedicarboxylic acid) (MCF-13 or 3D-Co) with a unique three-dimensional (3D) columnar structure. They used the electrochemical stripping method to convert 3D Co into 2D Co nanosheets

(NS). During the experiment, 3D Co could only be converted into 2D Co NS in the electrolyte saturated with oxygen, but this conversion would be very slow without electrolysis [94]. The thickness of the transformed 2D-Co-Ns was about 2 nm, which were in C2 space group. Li et al. synthesized 2D Co-BDC/EG nanosheets with the thickness of 3.2–3.5 nm by electrochemical stripping [95]. Peng et al. synthesized the first semiconductor porphyrin phosphonic acid 2D $[\text{Co}(\text{Ni-H}_7\text{TPPP})_2]\cdot 8\text{H}_2\text{O}$ (TPPP = 5,10,15,20-tetrakis[*p*-phenylphosphonic acid]porphyrin) by electrochemical stripping method. Single crystal structure analysis showed that this compound crystallized in triclinic space group P1. After stripping, the conductivity reached $0.12 \text{ S}\cdot\text{cm}^{-1}$ [96]. The electrochemical stripping is generally carried out under relatively mild conditions, which is more convenient to control, and is a promising method for stripping bulk MOFs to 2D MOFs.

Although the electrochemical stripping method can be used to break interlayer interaction and strip 3D layered structure to 2D components, it is only suitable for stripping layered MOFs and the yield is low. Through the combination of intercalation and stripping, a more reliable stripping method is cultivated. Zhou et al. designed new intercalation and chemical stripping method [97]. They found that the intercalation distance between the layers increased when 4,4'-dipyridine disulfide (DPDS) was inserted into the layered polymetallic organic compound crystals (Fig. 4a). A new intercalated metal-organic compound was formed, and then 20 times excessive TMP (trimethylphosphine) was added to the crystal solution to cut off DPDS so that the interaction force between 2D MOF layers was weakened, and 2D MOF nanosheets were peeled out. The Tindell effect generated by laser irradiation on the nanosheets promoted the occurrence of the exfoliation process (Fig. 4b). The folded or fractured sheet could be observed after stripping, and its height was measured to be about 1.0 nm (Fig. 4c, d). Fig. 4e showed that the crystal plane spacing of the nanosheets

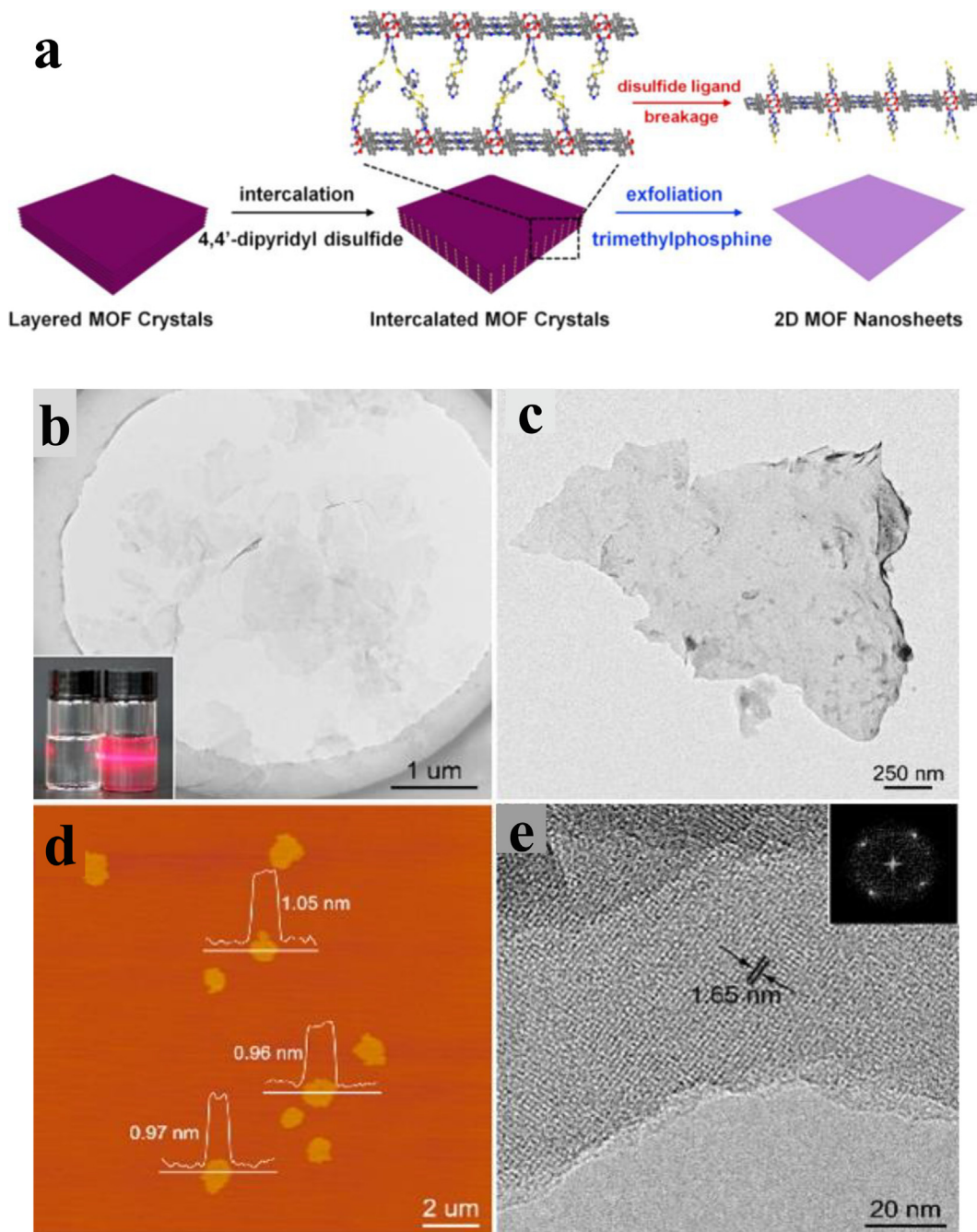


Fig. 4. (a) Composite diagram. (b) TEM image of the entire MOF nanosheet and (c) the single MOF nanosheet. (d) AFM image. (e) HRTEM images and FFT image. Reproduced with permission from ref. [97]. Copyright 2017, American Chemical Society.

was 1.65 nm, and the fast Fourier transform (FFT) image shows fourfold symmetry.

2.1.2. Bottom-up synthesis

The bottom-up method is used to prepare 2D MOFs by restricting the growth of coordination polymers in one direction or inhibiting the interaction between crystal layers in the synthesis process. The formation process is mainly due to the anisotropic growth of crystals. In this process, the growth rate of the transverse high energy surface of the material is higher than that of the longitudinal low energy surface, resulting in the preferential growth orientation of the 2D material in the horizontal direction [14]. The top-down approach relies primarily on diffusion media and

template synthesis, and small capping agents or modulators can be used to control crystal growth. Researchers usually control the thickness of nanosheets by tuning precursor concentration, reaction time, etc. Compared with the top-down method, the bottom-up method no longer needs MOFs crystals with a layered structure. More importantly, it no longer needs weak interaction in the crystals [77]. The bottom-up method has wider applicability, which includes interface synthesis, surfactant-assisted synthesis, and modulation synthesis.

The two-phase interface conforms to the basic characteristics of 2D nanomaterial structures. Hence, the interface synthesis method well combines the interface characteristics and material characteristics, and MOFs can be grown at the interface. There are three

interfaces for the synthesis of 2D MOFs: liquid–liquid interface, liquid–gas interface, and liquid–solid interface. Fonseca et al. synthesized several amorphous MOFs by liquid–liquid interface synthesis, including $[\text{Zn}(\text{FetpyCOOH})(\text{PF}_6)_2]_n$ (NEU-5), $[\text{Zn}(\text{Ru}(\text{terpy}^*_2)(\text{PF}_6)_2)]_n$ (NEU-6), $[\text{Fe}(\text{Ru}(\text{terpy}^*_2)(\text{PF}_6)_2)]_n$ (NEU-7), and $[\text{Ti}(\text{Ru}(\text{terpy}^*_2)(\text{PF}_6)_2)]_n$ (NEU-8), where pyridine plays two roles, one is to stimulate the electrophilic behavior of the metal source, and the other is to act as a sealant to prevent the growth of MOF in one direction [98]. 2-METHF (2-methyl-tetrahydrofuran) also plays two roles in the synthesis, one is to promote the deprotonation of $(\text{FeTp}^*\text{COOH})(\text{PF}_6)_2$ and $(\text{Ru}(\text{Terpy}^*_2)(\text{PF}_6)_2)$, and the other is to buffer medium alkalinity, creating a favorable interface for the synthesis. Since pyridine and 2-METHF are poorly miscible, metal ions and ligands diffuse into the transition segments at pH values of 7.49, 7.41, 6.63, and 7.16, rapidly forming nuclei and thus forming small domains.

The surface molecules in the liquid/gas interface may be affected by the uneven force from the liquid and gas phases, resulting in different physical and chemical properties of the gas–liquid interface. For example, at the water/air interface, a small amount of organic solvent is added to the water surface, and the water/air interface is formed after the evaporation of the organic solvent. The organic ligand forms a monodisperse layer on the water surface, which is beneficial to the synthesis of single-layer MOF nanosheets. Zeolite imidazole frameworks (ZIFs) are a subclass of MOFs with a large surface area and abundant pore structure [99,100]. Li et al. synthesized ZIF-8 thin film using the liquid/gas interface synthesis method [101]. The film had excellent porosity and an average thickness of 700 nm, and the film is homogeneous over a large area. The air side of the ZIF-8 film was smooth, while the liquid side was rough, suggesting that the two sides of the film may have different hydrophilicity. When the MeIM/Zn ratio was smaller, the film became thicker. This synthesis method can be applied to the self-crystallization of the porous membrane. In 2020, Li et al. reported a new air–water interface self-crystallization (AWISC) method to synthesize MOF using a polymer hollow fiber matrix [102]. They introduced solid polymer hollow fibers to support the MOF layer for obtaining the MOF membrane. This method can also be combined with the microfluidic process to prepare a long MOF-controlled fiber membrane. Makiura et al. grew 2D thin crystalline MOF nanosheets at the air/liquid interface [103]. The nanosheets are composed of porphyrin units and metal ion joints, which are completely oriented on the liquid surface of the Langmuir groove. The gas/liquid interface growth method has sufficient versatility and excellent crystallinity.

The layer-by-layer growth at the liquid/solid interface is to uniformly grow 2D layer along the *c* direction and control the thickness of the nanosheets by the number of cycles. Kitagawa et al. reported the layer-by-layer growth of nanosheets on the liquid/solid interface to synthesize $\text{Fe}(\text{py})_2[\text{Pt}(\text{CN})_4]$ (py = pyridine) nanosheets, where there was π - π interaction between adjacent pyridine molecules [104]. First, they prepared pyridine-capped self-assembled monolayers, and then the substrate was alternately immersed in an ethanol solution containing Fe^{2+} and $[\text{Pt}(\text{CN})_4]_2$ at room temperature. After 30 cycles, nanosheets were formed. Using the liquid/solid interface synthesis method, the thickness of the film and the crystal orientation can be controlled.

Interface synthesis is a simple and effective synthesis method, but it has certain limitations, mainly because the interface size affects the large-scale production of MOF nanosheets. The three-layer solvent synthesis method consists of three kinds of solvents with different densities. The intermediate layer is a buffer solution. Metal ions and organic ligands diffuse from the upper and lower liquid layers to the middle, respectively. The concentration of the intermediate buffer layer is very low, which is beneficial to produce ultrathin MOF nanosheets. Wang et al. synthesized 2D

$\text{Ni}_3(\text{HITP})_2$ films using liquid/liquid/gel interface synthesis [105]. The film was about 5 nm thick and had directional polycrystalline characteristics. Rodenas et al. synthesized CuBDC nanosheets by the three-layer solvent method [106]. The upper solution layer was 1 V(DMF): 2 V(CH_3CN), including $\text{Cu}(\text{NO}_3)_2$; the lower solution was 2 V(DMF): 1 V(CH_3CN), including BDC; and the intermediate solution was 1 V(DMF): 1 V(CH_3CN). Cu^{2+} in the upper layer and BDC in the lower solution were diffused to the middle layer to form CuBDC nanosheets. The transverse size of the nanosheets was 0.5–4 μm and the thickness was 5–25 nm.

Surfactant assisted method makes use of the feature that the surfactant can be selectively adsorbed on a specific surface of crystals so that MOFs can be grown in a directional plane. Li et al. reported the synthesis of two polycrystalline cobalt–molybdenum compounds (CTGU-5 and CTGU-6) by surfactant assisted synthesis. CTGU-5 synthesized with an anionic surfactant had a layered structure [107], while CTGU-6 synthesized with a neutral surfactant has a three-dimensional frame structure. Seoane et al. synthesized NH_2 -MIL-53 (Al) nanosheets via surfactant-assisted synthesis [108]. The separated nanolayers were identified by TEM and the dynamic behavior of the crystal structure changes with the flexibility. Sun et al. reported a method to synthesize large single crystals of Cu-BTC polycrystalline thin films with the assistance of surfactants [109]. They dissolved non-ionic surfactants and $\text{Cu}(\text{NO}_3)_2$ in deionized water to produce a Cu-surfactant solution and then added the surfactant solution into the H_3BTC (1,3,5-benzenetricarboxylic acid) ethanol solution. After 1–2 h, small pieces of crystalline precipitation could be seen, and after a week, large pieces of crystalline precipitation were formed. From SEM images, the crystal had an octahedral structure. With the assistance of surfactants, massive dense porous membranes could be synthesized.

Modulation synthesis has fine and effective control over the synthesis of MOFs, by which physicochemical properties such as crystallinity, particle size, and morphology can be controlled. Forgan et al. reported the effect of changing modulators on MOF synthesis [110]. They used dimethylformamide as the modulator and found that the nucleation rate was fast. Then, they added 37 % hydrochloric acid to the reaction solution and found that the addition of hydrochloric acid accelerated the crystallization process. Additionally, monocarboxylic acid modifiers such as benzoic acid and acetic acid could slow down the crystallization process and lead to the formation of larger particles. Cui et al. synthesized five kinds of Zr-((S)- H_4L) by using different acids as regulators [111]. They selected (S)- H_4L as the ligand and ZrOCl_2 as the metal source under solvothermal conditions using appropriate acids to obtain five kinds of Zr-((S)- H_4L). This experiment showed that the crystallinity and topological structure of MOFs can be modulated by the modulator. Moreover, the aperture and geometry of MOF crystals could be adjusted by modulation synthesis.

Using one synthesis method alone has some defects, for example, the yield is low or the structure of MOFs is difficult to tune. The combination of different synthesis methods will make the thickness of MOFs nanosheets adjustable and obtain high yield. Jia et al. synthesized ultrathin crystalline nanosheets using ultrasound-assisted and solvent-heating treatment (Fig. 5a) [112]. The (U + S)-CoFe-BDC ((U + S)-CoFe-MOF) had more pores than that synthesized without solvent heating. The thickness of (U + S)-CoFe-MOF was larger than that of MOF synthesized only by the solvothermal method (Fig. 5b–g). This method was simple and easy to operate and could be used to synthesize MOFs with large thicknesses. Yao et al. synthesized ultrathin MOF-74 nanosheets (M–MNS) using a sacrificial template method. A series of MOF-74 nanosheets, including Co-MNS, Fe-MNS, NiFe-MNS, and CoCu-MNS were synthesized by using ultra-thin metal oxide nanosheets (M–ONS) as the sacrificial template. FeCo-MNS with

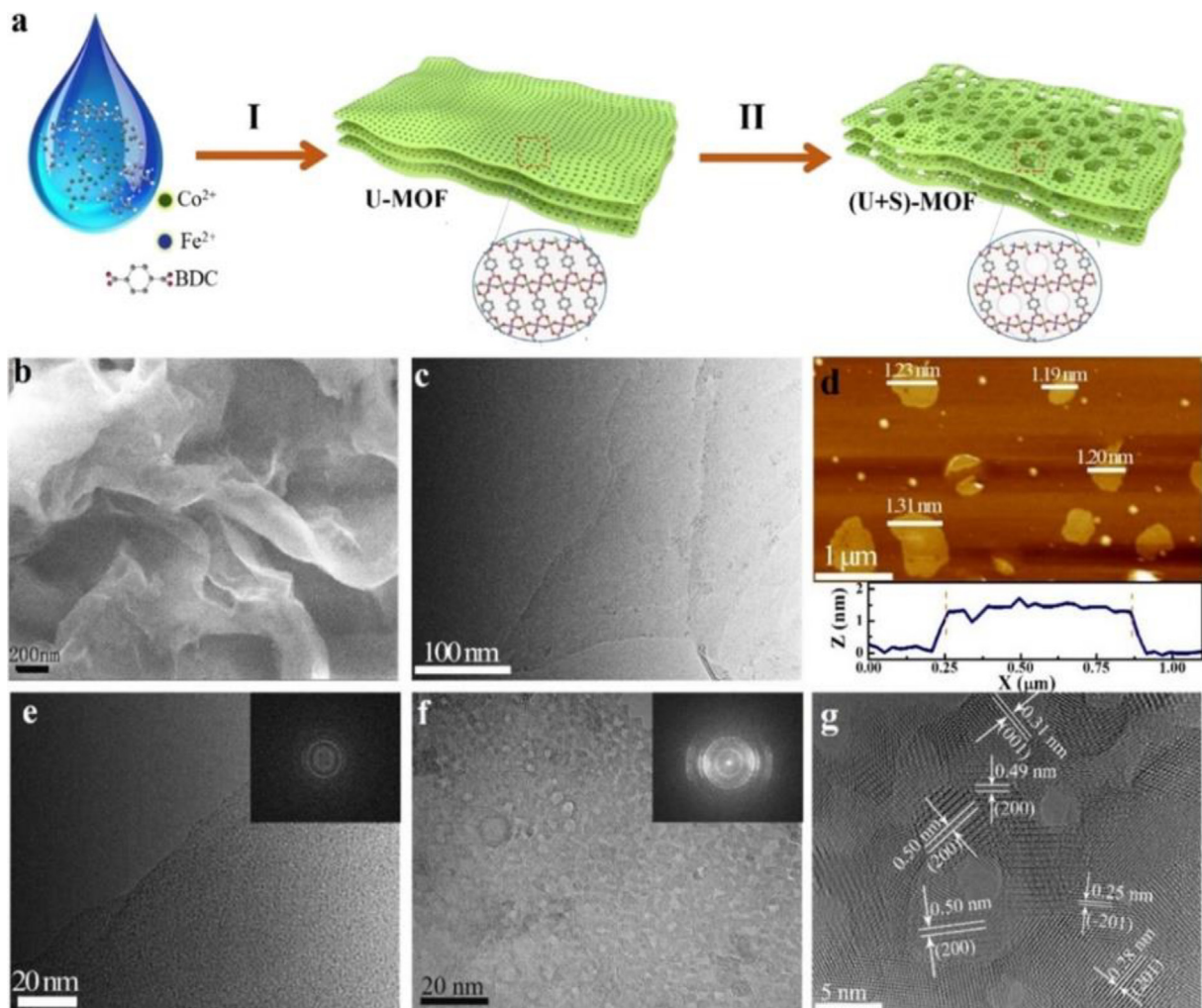


Fig. 5. (a) Preparation and structure diagram of (U + S)-CoFe-BDC. (b) SEM image and (c) TEM image of 2D CoFe-BDC. (d) AFM image and one typical height and size profile of the CoFe-BDC. TEM images of CoFe-BDC obtained by (e) only ultrasonic synthesis and (f) two-step synthesis. (g) HRTEM image of (U + S)-CoFe-BDC. Reproduced with permission from ref. [112]. Copyright 2019, American Chemical Society.

a thickness of 2.6 nm was synthesized with 2,5-dihydroxyterephthalic acid (H_4dobdc) as an organic ligand [113].

The top-down method is simple to operate but a low yield is usually obtained, while the bottom-up method is more complex in the synthesis process, but the morphology of MOFs can be controllable. Appropriate exfoliation methods combining both top-down and bottom-up characteristics can be used to fabricate 2D MOFs. For instance, Zhu et al. synthesized $[Zn(hsb-2)(2,6-ndc)]EtOH \cdot 4H_2O$ ($hsb-2 = 1,2$ -bis(4'-pyridylmethylamino)-ethane, $2,6-ndc = 2,6$ -naphthalenedicarboxylate) (HSB-W6) nanosheets using in-situ spalling method, which showed a double interspersing structure and could be applied as fluorescence sensors [114].

2.2. Synthesis methods of 2D MOF derivatives

2D MOFs have the characteristics of high specific surface area, high porosity and ultra-thin structure. However, 2D MOFs usually have poor conductivity and poor stability, which will affect electrocatalytic performance. To optimize the catalytic performance of 2D MOFs, researchers have explored many methods to prepare 2D nanosheets derived from MOFs. 2D MOFs are usually used as precursors to prepare derived materials by pyrolysis or other post-processing procedure. For example, 2D transition metal oxides, transition metal carbides, transition metal sulfides and transition

metal phosphides can be prepared by oxidation, carbonization, vulcanization and phosphating of 2D MOFs, respectively. Transition metal oxides have high stability, transition metal sulfides, transition metal phosphides have high electrocatalytic activity, and transition metal carbides contain carbon substrates with good conductivity. The extended materials prepared by post-treatment of 2D MOFs exhibit better stability, conductivity and electrocatalytic activity. However, there are many issues in the process of converting 2D MOFs into their derivatives, such as destroying the original pores, aggregation of 2D layer structure and reducing the intrinsic activity of active sites. Hence, it is a great challenge for researchers to prepare stable and ultra-thin 2D MOF-derived materials. Here, we summarize several methods for preparing 2D MOF-derived materials, including pyrolysis, oxidation and other synthetic methods.

2.2.1. Pyrolysis method

Carbon nanosheets have rich pores and high conductivity, which can be doped to improve electrocatalytic properties. Specific sacrificial templates are needed to limit the size and morphology of carbon nanosheets when preparing carbon nanosheets, and 2D MOFs are ideal sacrificial templates. Different carbon nanosheets with high catalytic performance can be prepared according to the types of MOFs and carbonization conditions, and different atoms

can be doped into carbon nanosheets. Carbon nanosheets with controllable size and thickness can be obtained by pyrolyzing suitable 2D MOFs under an inert atmosphere. The non-conductive organic part of the MOFs will be transformed into a highly conductive carbon matrix after pyrolysis, in which the metals are vaporized or reduced by carbon to generate more active sites and pores. Zhao et al. prepared B-N double-doped porous carbon (BNPC) by pyrolyzing $[Zn_2(im)(bdc)][B(im)_4] \cdot p\text{-murea}$ ($im = imidazole$), abbreviations: MC-BIF-1S, in an H_2/Ar mixed atmosphere (Fig. 6a) [115]. In the pyrolysis process, the zinc was reduced by carbothermic heat and then evaporated. The porous carbon was a bifunctional metal-free electrocatalyst, which showed good electrocatalytic activity and high stability in ORR and OER.

If the metal is not evaporated after pyrolysis, carbon nanosheets loaded with metal sites will be formed. Wang et al. used $Ni_2(2,6\text{-ndc})_2(\text{dabco})$ (DUT-8(Ni)) as the precursor to conducting pyrolysis in an atmosphere of argon and found that low annealing temperature led to incomplete pyrolysis of DUT-8(Ni) with low catalytic activity. When the pyrolysis temperature was $700\text{ }^\circ\text{C}$, the obtained carbon matrix composite showed the highest HER activity [116]. Ni@C-700 showed petal-like nanosheets after carbonization, but agglomerated after carbonization at high temperature, which led to the decrease of the distance between the nanosheets. Dong et al. converted $NaCl@ZIF-67$ into Co-N-C-NS by pyrolysis in the N_2 atmosphere (Fig. 6b). According to TEM image, Co-N-C NS was composed of uniform ultrathin carbon nanosheets without obvious aggregation of metal nanoparticles. HRTEM image showed that Co nanoparticles with the size of about 1–3 nm were uniformly dispersed on the carbon nanolayer. There were a large number of graphite carbon nanopores in the Co-N-C-NS and the electrocatalytic activity of ORR was significantly increased [117]. Liu et al. prepared Ni-Py MOFs by simple heat treatment of $NiSO_4$ and 4,4'-bipyridine, and then transformed them into porous N-doped Ni- $Ni_3S_2@C$ composites, which exhibited an η_{10} of 285 mV (Fig. 6c) [118]. After annealing, smooth nanosheets become rough slices embedded with small particles, but the rectangular shape of the nanosheets can be retained. TEM image showed that the carbon matrix was uniformly embedded in nanoparticles with a size of about 10 nm, which can be used as active sites to improve the catalytic activity of OER.

2.2.2. Oxidation method

Unlike pyrolysis in an inert atmosphere, the oxidation method is performed in air. MOFs can be converted into the corresponding oxides, while organic components undergo carbonization and oxidation. Zhang et al. synthesized Co-NDC (1,4- H_2 NDC = 1,4-naphthalenedicarboxylic acid) nanosheets by using 1,4- H_2 NDC as an organic linker and then calcined them in the air to synthesize a spinel Co_3O_4 hierarchical nanosheets (HNSs) (Fig. 7a) [119]. During the calcination, the heating rate was controlled at $2\text{ }^\circ\text{C min}^{-1}$ to avoid the collapse or agglomeration of the nanosheets. When the temperature reached $400\text{ }^\circ\text{C}$, Co-NDC can be completely decomposed. The prepared Co_3O_4 layered nanosheets have rich mesoporous structures and large surface areas.

Direct high-temperature calcination of MOFs to prepare derivatives usually leads to channel/pore collapse [120], which covers a large number of active sites and affects the electrocatalytic performance. To solve the problem, He et al. changed the complete decomposition of MOFs to the partial decomposition of MOFs (Fig. 7b) [23]. They partially decomposed the MOF precursor by controlled calcination, so that the porous structure of MOF could be preserved. They synthesized an ultra-thin 2D $Ni-C_8H_6O_4$ precursor and then calcined it in the air at $250\text{ }^\circ\text{C}$ to produce ultrafine NiO NPs. They found that the mesoporous structure of NiO NPs calcined at $400\text{ }^\circ\text{C}$ almost disappeared, indicating that the mesoporous structure of $Ni-C_8H_6O_4$ collapsed, while NiO NPs maintained a

uniform mesoporous distribution at $250\text{ }^\circ\text{C}$. Thus, controlled calcination has great flexibility to control the decomposition content of MOFs.

2.2.3. Other synthesis methods

Transition metal sulfides and phosphates have been demonstrated to have high electrocatalytic activity and stability [121,122]. Sulfurization and phosphating of 2D MOFs can improve the application in the field of electrocatalysis. Dou et al. [123] synthesized 2D Ni-BDC by in-situ growth, and then partially sulfurized it to obtain Ni-BDC@NiS, showing higher OER activity. The porous structure of Ni-BDC was preserved by partial vulcanization. The close binding and interaction between NiS and Ni-BDC are beneficial to the OER dynamics. Jayaramulu et al. prepared 2D $[Ni(C_4O_4)(H_2O)_2]_n$ under hydrothermal conditions [124]. The Ni_7S_6/GNS (GNS = graphene nanosheet) composite was obtained by sulfurization of the nanosheets with thiourea as a sulfur source, which showed better electrocatalytic performance than nickel sulfide/graphene-based composite. Polyvinylpyridinone (PVP) is used as the structural guide to preventing the aggregation of nanosheets. After curing, Ni_7S_6 also effectively prevents the re-accumulation of GNS. The material after curing has higher electrocatalytic activity and stability. The phosphating process enhances the electrical conductivity and enriches electrochemical active centers. Si et al. synthesized Zn-doped Ni-PTA (PTA = 1,4-benzenedicarboxylic acid) material on nickel foam, and then annealed it with NaH_2PO_2 at $350\text{ }^\circ\text{C}$ to obtain ZnNiP [125].

3. Electrocatalytic properties of 2D MOFs

2D MOFs show great potential in the field of electrocatalysis due to their high specific surface area, porosity and ultrathin structure, which can replace precious metal materials as electrocatalysts. Although the electrocatalytic performance of some 2D MOFs can be comparable to that of precious metals, most 2D MOFs have poor electrical conductivity, poor stability and other factors that affect the electrocatalytic performance [21]. Many researchers have adjusted the structure and function of 2D MOFs by modulating the metal centers and ligands and prepared their derived materials by carbonization, oxidation, vulcanization or doping other elements, which have more advantages than 2D MOFs. In this section, the factors affecting the electrocatalytic performance of 2D MOFs and the regulation strategies for improving the electrocatalytic performance are classified and summarized. The factors affecting the electrocatalytic performance of 2D MOFs mainly include the following points: (1) pore size and structure, (2) conductivity, (3) the intrinsic activity of the active site and (4) the number/density/distance of active sites.

3.1. Pore size and structure

There are many pores in 2D MOFs, which can provide mass transfer pathways for reactions. However, the pore size of most 2D MOFs is very small, which will seriously affect the electrocatalytic performance. Many studies have shown that the introduction of mesopores and macropores into MOFs helps to improve the mass transfer performance, thereby strengthening the catalytic performance. The pore structure and pore size affect the electrocatalytic activity, since they not only provide the electrocatalyst with more active sites but also increase the electron transfer rate. Mesoporous carbon materials have been a concern by researchers due to their adjustable mesoporous size and large specific surface area, which can be used in catalysis, sensor and energy storage. Wang et al. synthesized 2D Zr-tetrakis(4-carboxyphenyl)porphyrin porous membrane nanosheets (MOF-NS) with an ordered mesoporous

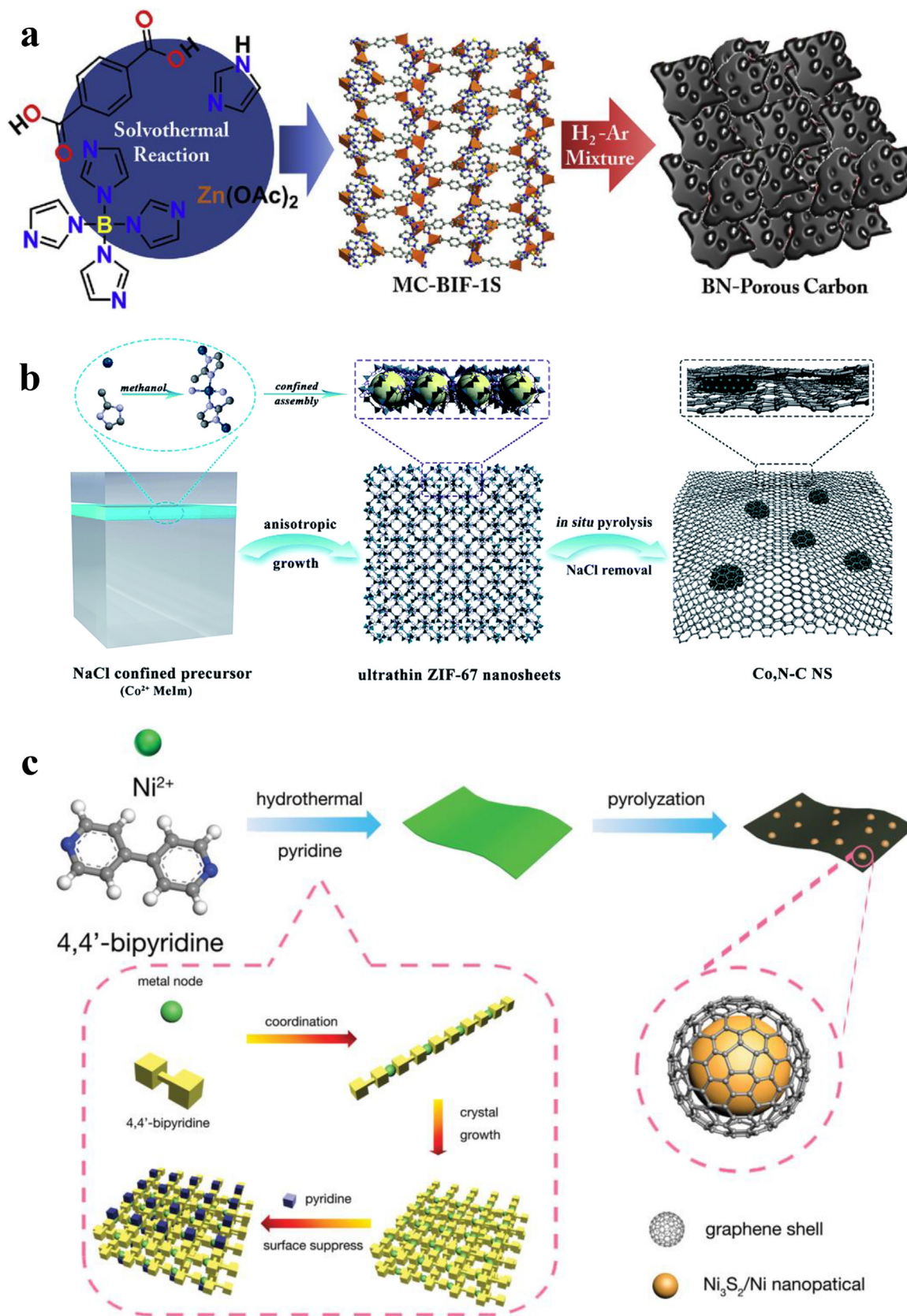


Fig. 6. (a) The synthetic scheme of BNPCs. Reproduced with permission [115]. Copyright 2017, Elsevier Ltd. (b) The synthesis of Co, N-C NS. Reproduced with permission [117]. Copyright 2017, Royal Society of Chemistry. (c) The preparation strategy of Ni- Ni_3S_2 /carbon nanoplates. Reproduced with permission [118]. Copyright 2019, Wiley-VCH.

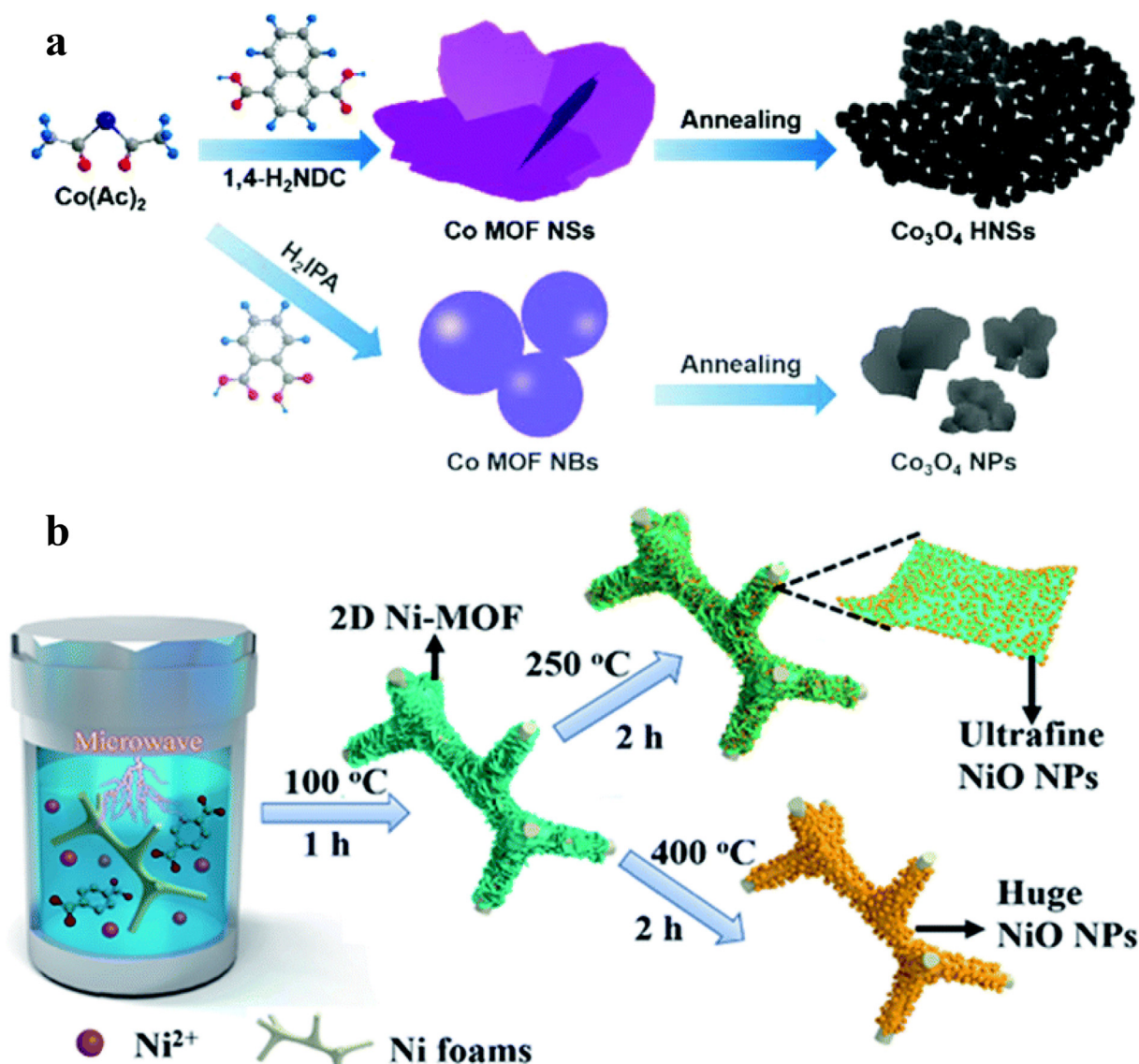


Fig. 7. (a) The synthesis process of Co_3O_4 HNSs and Co_3O_4 NPs. Reproduced with permission [119]. Copyright 2020, Royal Society of Chemistry. (b) The synthesis process of NiO NPs. Reproduced with permission [23]. Copyright 2020, Royal Society of Chemistry.

structure. They anchored Cu, Co and Fe to prepare MOF-NS-M, and found that MOF-NS-Co showed better CO_2RR activity than HER activity, suggesting that the catalytic center of CO_2RR was Co. The unique structure and visible light effect of the MOF-NS-M made them have better conductivity and more active sites [126]. Guo et al. synthesized porphyrin based 2D-CuTCPP/flake ordered mesoporous carbon (pOMC) composites [127]. The introduction of pOMC not only increased the adjustable mesoporous structure but also enhanced the conductivity of the composites and weakened the interlayer stacking, thus exposing more active centers.

Although mesoporous carbon has been widely studied in the field of electrocatalysis, it is a great challenge to prepare mesoporous carbon with a highly exposed surface area. Researchers are trying to solve this problem, such as reducing mesoporous carbon to the nanoscale, but the operation is very complex. Researchers fabricated a hollow structure, which not only has hole space, but also has an ultra-thin thin shell structure, showing high electrocatalytic performance. Yamauchi et al. prepared hollow-structured mesoporous carbon (HOMC) nanoplates by a simple and general method [128]. In the preparation process, resorcinol formaldehyde F127 micelles were segregated on the surface of

the nanosheets, so that the products had ordered mesoporous and hollow structures. After carbonization, HOMC nanosheets with good mesoporous and hollow structures were obtained, which can improve the electrocatalytic ORR performance and have excellent cycling stability. Xia et al. proposed a mechanism to enhance the electrocatalytic OER performance of AuNRs/NiCo-BDC- NO_2 ($\text{H}_2\text{BDC-NO}_2 = \text{nitroterephthalic acid}$) (AuNRs/NiCo-MOF) composites [129]. Firstly, they synthesized 2D ultrathin NiCo-BDC- NO_2 materials (Fig. 8a-c). Subsequently, they injected Au nanorods (AuNRs) into 2D NiCo-BDC- NO_2 under 808 nm light irradiation to obtain AuNRs/NiCo-MOF, and the structure is shown in Fig. 8d, e. AuNRs/NiCo-MOF showed an initial potential of 1.43 V and a low overpotential of 283 mV at 10 mA cm^{-2} in 1.0 M KOH, which were better than those of NiCo-BDC- NO_2 and AuNRs (Fig. 8f). The J - T curve showed that the photocurrent response of AuNRs/NiCo-MOF had high reversibility (Fig. 8g). The Tafel slope of AuNRs/NiCo-MOF decreased under light irradiation (Fig. 8h), but the irradiation had no effect on NiCo-BDC- NO_2 , which further indicates that AuNRs doping could improve the OER kinetics. Under the irradiation of 808 nm, an electron-hole pair was formed between AuNR and NiCo-BDC- NO_2 . Under appropriate bias voltage, the hot

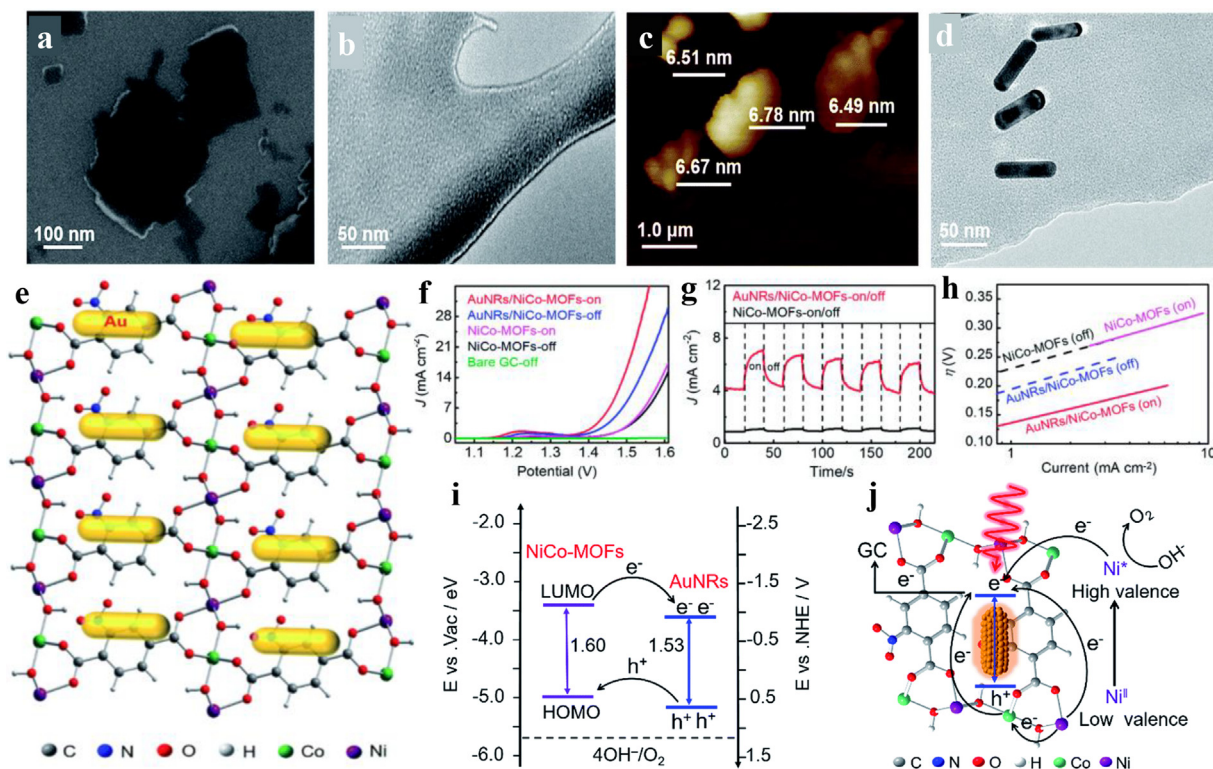


Fig. 8. (a) SEM image, (b) TEM image, and (c) AFM image of NiCo-BDC-NO₂. (d) TEM image of AuNRs/NiCo-MOF. (e) Schematic diagram. (f) LSV curves. (g) *J*-*t* curves. (h) Tafel plots. (i) The transfer processes of hot charge carriers between AuNRs and NiCo-BDC-NO₂. (j) Schematic electron transfer paths. Reproduced with permission from ref. [129]. Copyright 2019, Royal Society of Chemistry.

electrons were transferred to the external circuit, and the hot holes were injected into NiCo-BDC-NO₂, which decreased the energy level of NiCo-BDC-NO₂ (Fig. 8i). This charge transfer channel contributed to the formation of high-valence active center Ni* in NiCo-BDC-NO₂. The decrease of energy level and the increase of active center were helpful to improve the electrocatalytic activity of OER (Fig. 8m).

3.2. Conductivity of 2D MOFs and their derivatives

Electrocatalysis involves electron transfer and electrode surface reaction, which requires the electrocatalyst must have two functions at the same time: (1) It can conduct electricity and transfer electrons freely; and (2) it can effectively catalyze the targeted reaction. For high electrical conductivity, the electrocatalyst should provide electron channels for electron exchange, and the channel does not cause a serious voltage drop [130]. Different numbers of *d* electrons in transition metal ions affect the conductivity. Generally speaking, for a definite MOF, the higher the electrical conductivity is, the higher the electrocatalytic performance will be. Conductivity is an important factor in evaluating MOFs, which mainly depends on the density and mobility of charge [131]. Charge migration in MOFs is mainly divided into jump transport and band transport, in which band transport is conducive to a higher charge migration rate [132]. Therefore, the combination of metal ions containing high-energy electrons or holes with organic ligands with stable free radicals can promote charge transfer and enhance conductivity. In addition, highly conductive materials can be introduced into MOFs [133]. 2D MOFs materials have efficient interlayer charge transfer characteristics, and the ultra-thin structure accelerates the charge transfer rate. Wen's team selected different metal ions to modulate the metal centers of Co-BDC, Ni-BDC, and CoNi-BDC [134]. The Co-BDC had the smallest oxidation

peak potential and the lowest voltage difference. Since the thickness of Co-BDC was only 2.6 nm, a stable electrochemical reaction could take place on the surface. Liu et al. synthesized Fe-doped Ni-NH₂-BDC nanosheets on nickel foam (NF) (Fe-Ni-MOF-NSs/NF) using a template growth strategy for the OER [130]. The Fe-Ni-MOF-NSs/NF required a low overpotential (η_{50}) of 258 mV. The solid contact between Fe-Ni-MOF-NSs and NF led to the good conductivity of the nanosheets, and thus improved the electrocatalytic performance. Thermal annealing is effective to improve the conductivity of MOFs. Lai et al. annealed 2D-MOF in H₂ and Ar to synthesize Co-BDC/H₂ and Co-BDC/Ar [135]. Co-BDC/H₂ showed an η_{10} of only 312 mV, lower than Co-BDC/Ar due to the improved conductivity after H₂ treatment.

Single atom catalysts (SACs) are the minimum limit of metal particle catalysts, which can maximize the utilization of metal atoms on the atomic scale. The utilization rate of metal atoms is very high. In addition, the metal centers are in unsaturated coordination, which helps to improve the conductivity, stability and high activity. Jiang et al constructed monoatomic iron embedded nitrogen doped carbon using porphyrin MOF (PCN-222) [136]. The aggregated Fe atoms in PCN-222 (Fe) can be removed by HF (20 wt%) etching, and Fe₁-N-C SAC was prepared. The single atom Fe increases the atomic utilization and conductivity. Combined with the layered porous structure, Fe₁-N-C showed efficient ammonia synthesis and reduced the potential barrier of the rate-determining step (RDS).

In recent years, metal/carbon functional materials have attracted extensive attention, but they are also subject to many limitations, such as over sintering, poor conductivity and poor corrosion resistance during annealing in air. Heumann et al. combined a 2D cobalt-based MOF with graphite sheets to prepare metal/carbon electrocatalyst. The nanostructure can be controlled by adjusting macromolecular precursors, and the graphite matrix can

significantly improve the conductivity [137]. Wen et al. synthesized $\text{Co}_3\text{O}_4@\text{N}/\text{C}$ nanocomposites with a core-shell nanostructure composed of Co_3O_4 nanoparticles and N-doped carbon matrix, which showed good conductivity, ORR activity, and stability [138]. Li and colleagues found that 2D Co-BDC/EG as electrode material for non-enzymatic glucose sensors had high activity in glucose sensing [95]. The catalytic performance can be enhanced by improving the conductivity, which can be combined with carbon nanotubes, graphite and other materials with well electric conductivity.

3.3. Regulating electronic structure

The intrinsic activity of electrocatalysts depends on the adsorption strength between active sites and reaction intermediates and the energy of transition states, and the electronic structure of active sites directly determines their properties. In addition, the electronic structure plays a decisive role in the charge transport of MOFs, influencing the electrical conductivity and catalytic performance [21]. There are three common methods to regulate the electronic structure, including the regulation of metal centers, ligands and defects.

2D multi-metal MOFs show excellent electrocatalytic performance. The introduction of a second metal element into single-metal MOFs can regulate the original electronic structure of the materials, improve the electron transfer rate, and optimize the intrinsic catalytic activity. On the one hand, the introduction of a second metal may promote the transfer of electrons. On the other hand, there is interaction between the two metals, which may lead to the oxidation of a certain metal to a higher valence state and the enhanced intrinsic activity. Hou et al. doped Ce into Ni-BDC to generate Ce-NiBDC/OG (Fig. 9a, b) [139]. The structure remained good after Ce doping, and Ni and Ce metals were uniformly dispersed in

the skeleton. Ce-NiBDC/OG has superhydrophilic and superhydrophobic surfaces, which is conducive to the release of O_2 . From high-resolution XPS, compared with NiBDC/OG without Ce doping, Ni $2p_{1/2}$ and $2p_{3/2}$ in Ce-NiBDC/OG were negatively shifted by 0.2 eV (Fig. 9c), indicating that Ce doping promoted the electron transfer from Ce to Ni. Ce-NiBDC/OG showed an η_{10} of 265 mV in 1.0 M KOH, lower than Ni-BDC/OG (301 mV) and Ce-BDC/OG (466 mV) (Fig. 9d). To further understand the influence of Ce doping on the electronic structure of Ni atoms, the Bader charge number was calculated. The results showed that after Ce doping, the charge number of adjacent Ni atoms decreased from 1.154 e to 1.130 e (Fig. 9e), which was consistent with the results of XPS analysis. NiOOH was electrochemically formed, and after Ce was doped, it was transformed into Ce-NiOOH, which was the real active site. DFT calculations showed that the ΔG value of $^*\text{O}$ intermediate formed on Ce-NiOOH was significantly lower than that on NiOOH (Fig. 9f), indicating that Ce doping played a key role in promoting the OER kinetics. Yan et al. prepared 2D $\text{Co}_x\text{Fe-NH}_2\text{-BDC}$ ($\text{Co}_x\text{Fe-MOF}$) nanosheets with thickness of about 10 nm by controlling the proportion of metal salts in the precursor solution [140]. In 1.0 M KOH, $\text{Co}_3\text{Fe-MOF}$ exhibited η_{10} of 280 mV and Tafel slope of $38 \text{ mV}\cdot\text{dec}^{-1}$. According to XPS analysis, Co^{2+} and Co^{3+} existed in $\text{Co}_3\text{Fe-NH}_2\text{-BDC}$. The doping of Fe atoms caused the transformation of partial Co^{2+} to Co^{3+} . In addition, the combination of Fe and Co optimized the filling of e_g orbit, and changed the electron acceptance ability of Co^{2+} in the OER.

The organic ligands in 2D MOFs can effectively regulate the electronic structure of metal centers and optimize the intrinsic activity of MOF materials. Li et al. prepared missing interface MOF by introducing missing joints into layered column MOF $\text{Co}_2(\text{OH})_2(\text{C}_8\text{H}_4\text{O}_4)(\text{CoBDC})$ [57]. According to DFT calculations, terephthalic acid in CoBDC can be replaced by the missing carboxyl ferrocene joint (Fc), and a new stable MOF (CoBDC-Fc) can be

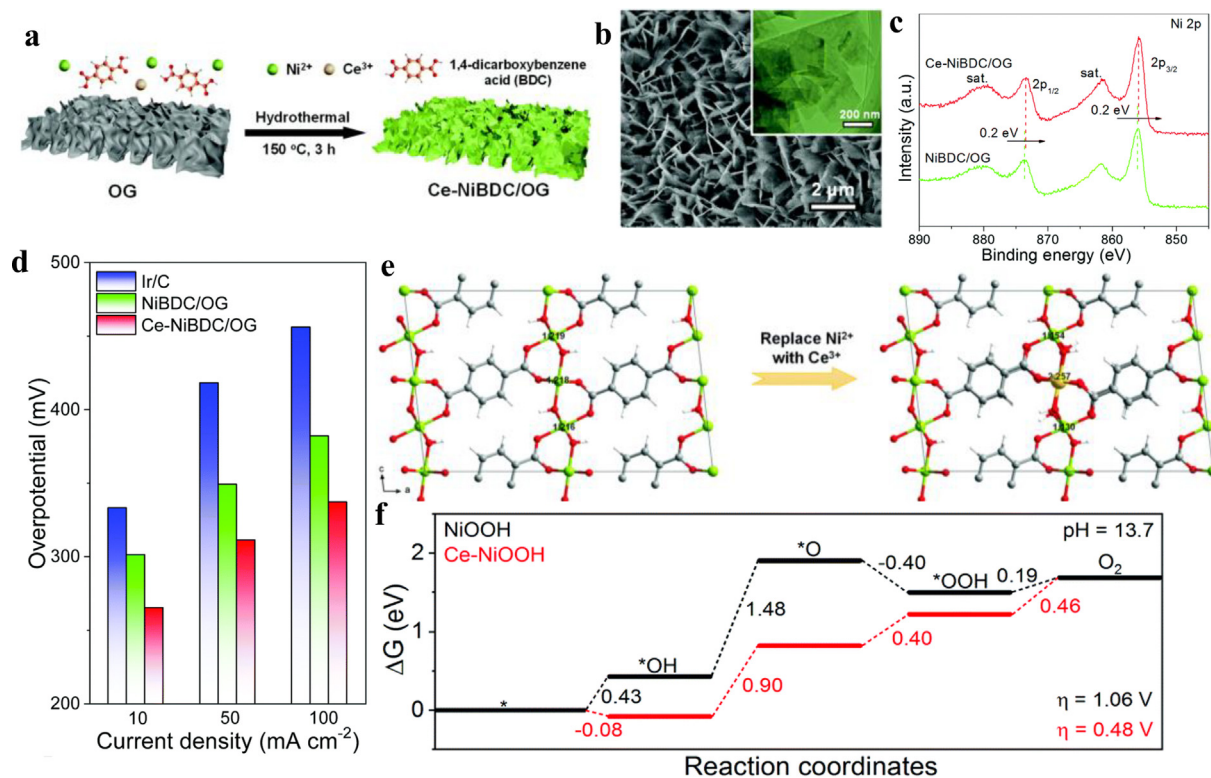


Fig. 9. (a) Composite graph of Ce-NiBDC/OG. (b) FESEM image and TEM image. (c) High resolution XPS. (d) Overpotential comparison. (e) The Bader charge numbers of NiBDC/OG and Ce-NiBDC/OG. (f) Calculated free-energy diagrams and theoretical overpotentials. Reproduced with permission from ref. [139]. Copyright 2021, Royal Society of Chemistry.

formed. PDOS showed that after the introduction of Fc, the new electronic states generated by CoBDC-Fc near the Fermi level are mainly due to the changes in the electronic structures of Co and O. DFT calculations showed that the introduction of Fc led to the formation of defect in site Co2 in CoBDC-Fc. When OH* was oxidized to O*, it had a low energy barrier of 1.85 eV, which meant that the electronic structure of the defect site favors the OER. XPS results showed that the introduction of Fc led to the change of the coordination environment of the active center, and the maximum energy of the valence band blue shift to the vacuum level of CoBDC-Fc is significantly lower than that of CoBDC, which also indicated that the electronic structure of MOF has changed. In 1.0 M KOH, the η_{10} on CoBDC-Fc in OER was 291 mV, which was lower than that of CoBDC (378 mV). Chen et al. anchored iron phthalocyanine (FePc) onto 2D MOF nanosheets (Ni-1,4-monobenzodiarboxylic acid pyrazide, Ni-MOF) for HER [141]. The FePc was evenly anchored on the surface of Ni-MOF ultra-thin nanosheets (Fig. 10a-e). The onset HER potential on the FePc@Ni-MOF was 140 mV and the η_{10} was 334 mV (Fig. 10f-g). Even at high current densities, FePc@Ni-MOF exhibited good electrocatalytic properties, which can be attributed to the interaction in the electrons that regulated the electronic environment of the central Fe and Ni sites. According to XPS results, in FePc@Ni-MOF, the Fe 2p binding energy shifted negatively, and the strong electron effect can adjust the electronic environment of the active site.

The existence of defects has a significant effect on the electronic structure of MOFs. The point defects in MOFs can cause periodic crystal defects in the local range, thus changing the electronic structure and electronic filling mode [142]. The materials synthesized by in-situ electrochemical method show abundant oxygen defects after redox process, which can regulate the electronic structure of active centers. Shen et al. adopted nickel foam to assemble CoM-ZIF-L nanosheet microarray, and obtained aCo(OH)₂-ZIF-L/NF-40 after optimization (Fig. 11a-c) [143], which showed an η_{100} of 290 mV for the OER (Fig. 11d-f). The oxygen defects can not only adjust the surface chemical and electronic structure, but also act as adsorption sites and active centers. Moreover, the concentration and electronic structure of oxygen defects can also be optimized by CV spark cycles. DFT calculations showed that the ΔG of the potential limiting step on oxygen defects was 0.49 eV (Fig. 11g), which was lower than that of the perfect surface, indicating that the defect surface was more active than the perfect surface.

3.4. The number/density/distance of active sites

In chemical reactions, the spatial distribution of catalytic active sites has an important effect on the overall activity of catalysts. The morphology, particle size, and specific surface area influence the catalytic activity. Zhang et al. synthesized Co-BDC nanosheets based on bulk MOF-71 [144]. Compared with bulk MOF-71, the double-layer capacitance of Co-BDC nanosheets increased by 12 times, indicating that Co-BDC nanosheets had a large point tiger hole surface area, which was conducive to exposing more active sites, thereby improving the electrocatalytic activity. These influencing factors are crucial, but they are also complex and challenging for the structural design of catalysts. Here, we summarized these factors as the number/density/distance of active sites. The electrocatalytic performance of MOF materials can be increased by increasing more exposed active sites or reducing the distance between active sites. There are two main methods: one is to inhibit molecular aggregation/accumulation, and the other is defect regulation.

To increase the density of active centers, we can prevent the movement of the metal centers by using the space confinement effect, and in this way, the formation of inorganic metal particles can be avoided. Wang et al. converted 2D Ni₂(2,6-ndc)₂(dabco) (DUT-8(Ni)) into nickel carbon matrix composites by adjusting the annealing temperature Ni@C-X (X represents annealing temperature) [116]. The higher the annealing temperature is, the more serious the aggregation of nickel nanoparticles will be. At low temperature, DUT-8(Ni) was not completely decomposed and its catalytic performance was poor. With the increase of temperature, the catalytic performance improved slowly. When the annealing temperature was raised to 800 °C, the electrochemical specific surface area decreased and the catalytic activity decreased slightly. Since nickel nanoparticles are the main active component of HER, when they are coated with graphite carbon layer, the aggregation of nickel nanoparticles is inhibited and the electrocatalytic activity is enhanced. Jayaramulu et al. prepared 2D [Ni(C₄O₄(H₂O)₂)_n (H₂-C₄O₄ = squaric acid) (Ni-MOF) with polyvinylpyrrolidone (PVP), which can be used as a structure directing agent to effectively prevent the agglomeration of Ni-MOF (Fig. 12a, b) [124].

2D MXenes (carbides, nitrides, and carbonitrides) have the advantages of adjustable structure, hydrophilicity and many redox active sites, but the defect is easy to aggregate, which reduces the stability of the catalysts [145,146]. The hole limiting effect of MOFs

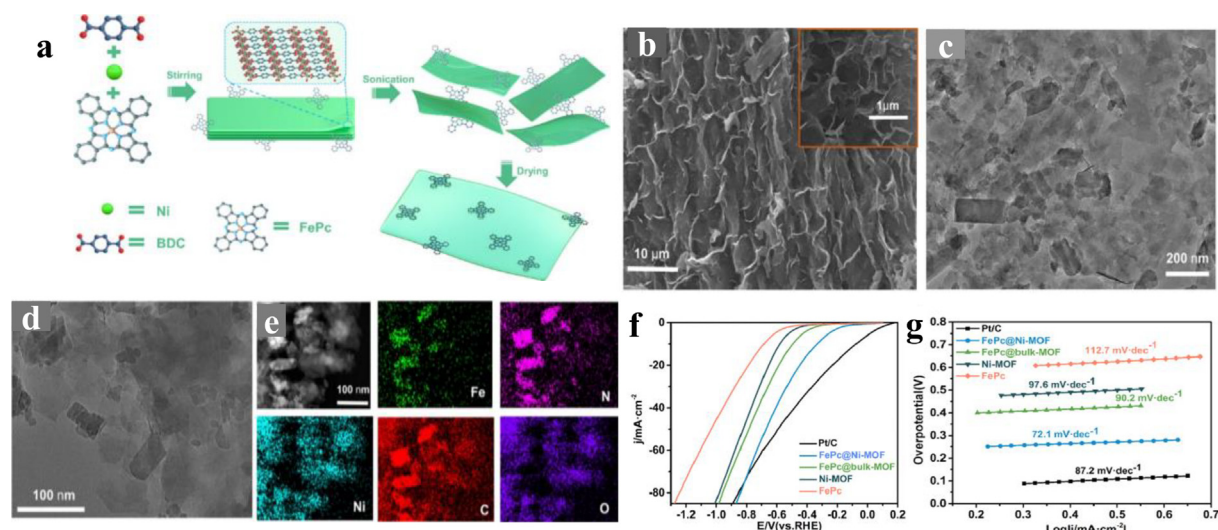


Fig. 10. (a). Synthesis diagram for FePc@Ni-MOF. (b). SEM image. (c). TEM image. (d). HAADF-STEM image. (e). Corresponding element mapping. (f) Polarization curves. (g) Tafel slopes. Reproduced with permission from ref. [141]. Copyright 2021, American Chemical Society.

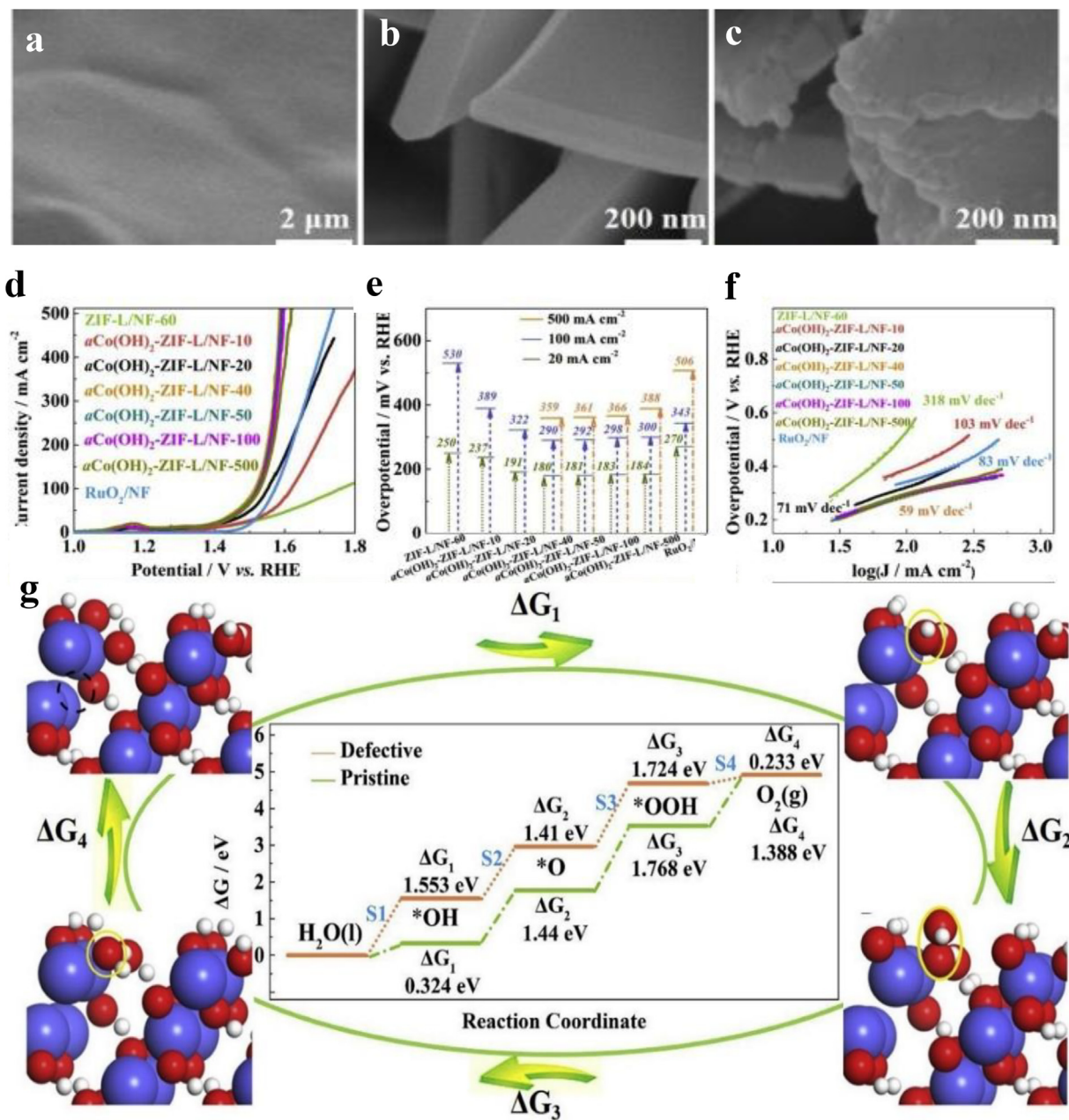


Fig. 11. SEM image of (a) NF, (b) ZIF-L/NF-60 and (c) $\alpha\text{Co}(\text{OH})_2$ -ZIF-L/NF-40. (d) LSV curve. (e) Overpotential at different current densities. (f) Tafel slope. (g) The optimized free energy diagram. Reproduced with permission from ref. [143]. Copyright 2021, Elsevier Ltd.

and the adjustable bit space can provide an excellent environment for MXenes and prevent their agglomeration. Liu et al. synthesized $\text{CoP-NC@Ti}_3\text{C}_2\text{T}_x$ as an efficient Li^+ electrode by phosphating ZIF-67@MXenes, which inhibited the accumulation of Ti_3C_2 MXenes [147]. The agglomeration can be inhibited using different synthetic methods and solvents. Han et al. assembled CNF@Ni-CAT (CNF = carbon nanofibers, CAT = catecholate) flexible self-supporting membrane [148]. The combination of electrospinning technology and hydrothermal method can not only improve the performance of the carbon nanofiber matrix, but also solve the problem of agglomeration. Guo et al. prepared 2D MOFs/polymer core-shell composites by a double solvent method [149]. The composites obtained by using two different polar solvents effectively avoided the phenomenon of agglomeration and uneven modification. Kaskel et al. studied the bottom-up synthesis method and

found that the ideal solvent can not only tear the layer, but also effectively prevent agglomeration in the suspension [150].

Defect regulation of MOFs mainly involves the regulation of point defects formed by metal nodes or organic ligand vacancies. The formation of such defects favors to expose more coordination unsaturated sites, thus improving the electrocatalytic activity to a certain extent [151–153]. Amino-functionalized MOF could effectively improve the catalytic activity, because amino is a hydrophilic group, which can increase electron transfer. Cao et al. prepared a layered $\text{AM-FeCo}(\text{OH})_x$ hybrid structure with rich defects [154]. After etching in $\text{NH}_3\cdot\text{H}_2\text{O}$, a large number of cobalt/iron hydroxide nanosheets coated on the surface form a core-shell structure. The structure has abundant active sites/defects, which not only increases the specific surface area, but also promotes proton-coupled electron transfer, reduces the reaction barrier

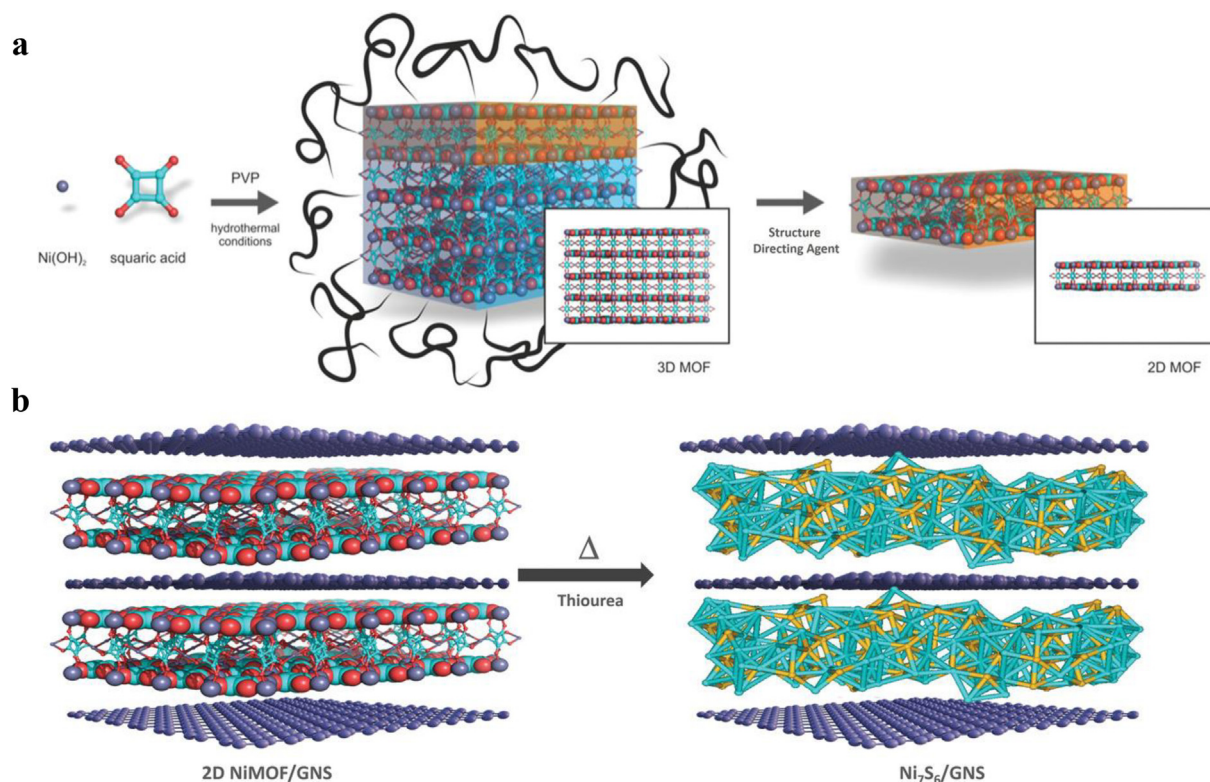


Fig. 12. (a) The formation of 2D $[\text{Ni}(\text{C}_4\text{O}_4)(\text{H}_2\text{O})_2]_n$ layers. (b) The preparation of heterobilayer hybrids of 2D graphene. Reproduced with permission [124]. Copyright 2019, Wiley-VCH.

and accelerates the reaction kinetics. Zhou et al. developed a method combining doping, annealing and vulcanization to synthesize a cobalt-based Ni-Co-S nanoarray (HPNA) [155]. Ni-Co-SHPNA is a defect-rich nanosheet with high specific surface area and porous structure. The diffusion path of ions is short and the active sites are abundant. For OER in 1 M KOH, Ni-Co-S-HPNA showed a low η_{10} of 270 mV. Furthermore, Ni-Co-S-HPNA exhibited a low η_{10} of 110 mV for HER. This preparation strategy plays an important role in the subsequent catalysis of overall water decomposition.

Through unremitting efforts, researchers have found many ways to improve the electrocatalytic performance of 2D MOFs. Despite the current research on improving electrocatalytic performance of 2D MOFs has made great progress, there are still much untapped potential. Most 2D MOFs still failed to perform practical applications, and hence, it is still an important content of electrocatalysis to find the right control strategy to improve the catalytic performance.

4. Electrocatalytic applications of 2D MOFs and their derivatives

4.1. Oxygen evolution reaction

The OER occurs at the anode of water electrolysis, involving the coupling of four electron protons, which is relatively complex. At present, researchers have not found a clear evolution path of OER reaction intermediates, but proposed some possible mechanisms, as shown in the Fig. 13 [156]. OER is a heterogeneous reaction involving multiple mixing steps. The formation of intermediates such as OH^* , O^* , OOH^* and the formation of M-O will affect the electrocatalytic performance. OER involves the transfer of four electrons, which requires high overpotential in the charging process of metal-air batteries and the anodic reaction of electrocatalytic water splitting, and is the highest energy consumption

process. At 25 °C, the thermodynamic voltage of OER is 1.23 V (vs RHE). It is necessary to find high performance electrocatalysts to improve the kinetics of OER. Ruthenium dioxide and iridium dioxide have been found to be highly active for OER [157]. However, both ruthenium and iridium are precious metals, which are costly and scarce elements. As more and more MOFs were found to be active for the OER [158], researchers began to turn their attention to 2D MOF materials.

4.1.1. 2D MOFs for OER

Transitional metals such as Fe, Co, Ni, Cu and Mn are the active centers of OER. 2D MOFs based on these transition metals can be fabricated using electron-rich ligands to stabilize the oxidation state of metal ions and enhance the charge transfer ability. MOFs with Co and Ni as metal centers exhibit excellent catalytic performance due to their excellent surface structure and physicochemical properties [159]. However, the original Ni-based and Co-based MOFs are easy to agglomerate in the OER process, and the catalytic ability is relatively weak. Introducing heterogeneous metal atoms or compounds into MOFs can adjust their electronic structure and enhance the intrinsic catalytic activity. Metal heteroatoms can be introduced into Ni- or Co-based MOFs, and the coupling effect between various metals is of great help to improve the catalytic activity. In addition, combining MOFs with heterogeneous elements (e.g. ferrocene carboxylate or $\text{Ti}_3\text{C}_2\text{T}_x$ nanosheets) can not only effectively prevent the aggregation of nanosheets, but also optimize the electronic structure. In addition to Ni- and Co-based MOFs, Cu-based MOFs also have great catalytic potential, which is conducive to commercialization.

4.1.1.1. Ni-based MOFs. In recent years, 2D Ni-based MOFs have been proven to have high OER electrocatalytic activity [160]. Biradha et al. synthesized six different 2D MOF compounds using

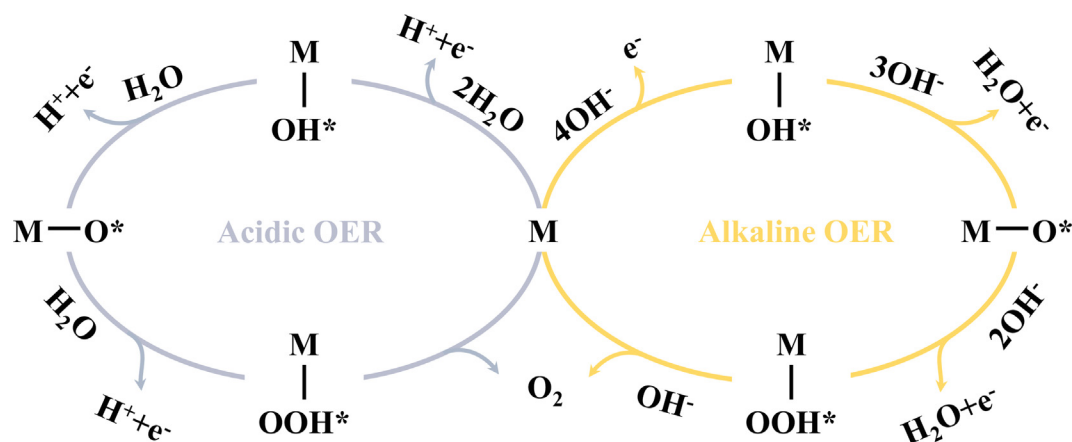


Fig. 13. Schematic illustration of the OER.

Ni, Cu and Co as well as different ligands [161]. $[(\text{Ni}(\text{L1})(\text{TA}) (\text{H}_2\text{O})_2) \cdot 2\text{H}_2\text{O}]_n$ (TA = 1,4-benzendicarboxylate (1,4-bdc)) (Ni-MOF) crystallizes in the $P\bar{1}$ network group and has an open 2D rectangular network. The Ni-MOF with 2D rectangular grid network exhibited the lowest η_{10} of 370 mV, and the highest ECSA value of 5.67 cm^2 . During the electron transfer process, Ni(II) was oxidized to Ni(III), followed by oxidation to Ni(IV), and then the high-valence Ni was reduced to Ni(II) by releasing O_2 . Usually, π -conjugated 2D MOFs have high intrinsic conductivity. Du et al reported high conductivity π -conjugated $[\text{Ni}_3(\text{C}_{32}\text{H}_{16}\text{N}_{16})]_n$ (NiPc MOF) [162], in which NiPc can not only serve as the connection unit, but also can serve as the active site of electrocatalysis. The electrocatalytic activity of NiPc-MOF increased with the increase of pH. In 1.0 M KOH, NiPc-MOF showed a low initial potential (1.48 V).

Nickel foam (NF) is a conductive substrate, which can enhance the electron transfer ability and reduce the electron transfer resistance. Liu et al. synthesized Ni-Fe-HPLC (HPLC = 2-amino terephthalic acid) on NF [130], which exhibited an η_{50} of 258 mV for the OER. According to AFM, the thickness of nanosheets is about 10 nm. These vertical nanostructures and NF skeletons can expose more active sites and increase the transmission of electrons and mass. Viswanathan et al. synthesized NiCo-BDC/NF, which showed a low η_{50} of 270 mV for the OER [163]. Co ion insertion changed the triclinic structure of Ni-BDC to face-centered cubic structure. The synergistic effect of the two metals enriched the active centers and NF made MOFs with faster electron transport and enhanced electrical conductivity. At the same time, the array of 2D nanosheets also helps to expose the active sites and has excellent mass transfer performance. The conductivity can be improved by metal doping, but the mechanism is unclear. 2D MOFs and ultrathin nanosheets can accurately determine the surface atomic structure and bonding arrangement, and obtain accurate structure–property relationship. Zhang et al. synthesized 2D Ni-Ln heterometallic MOF using electrochemical stripping design (Fig. 14a) [15]. 2D-Ni₄Ce is a light purple block crystal, which crystallizes in the $P\bar{1}$ space group of triclinic system. When 2D-Ni₄Ce was immersed in 0.5 M KHCO_3 , a powder sample (2D-Ni₄Ce-TD) was obtained after centrifugation (Fig. 14b-d). It took only 900 s to increase the current density from 7.3 to 27.5 $\text{mA}\cdot\text{cm}^{-2}$ (Fig. 14e, f). During the catalytic process on 2D-Ni₄Ce, the lamination of nanosheets was gradually stripped off to form sub-nanosheets, which increased the mass transfer rate. Through DFT calculations, the order of the free energy barrier of RDS was as follows: 2D Ni₄Pr > 2D Ni₄La > 2D Ni₄Ce (Fig. 14g-i). PDO calculations showed that the oxidation state and local electronic structure of Ni (II) would lead to different catalytic activities of metal–organic

nanosheets (MONs), and the d-band center of 2D-Ni₄Ce was higher, which indicated that the binding between the adsorbent and the catalyst was earlier, and thereby the OER activity was higher.

In short, 2D Ni-based MOFs have high OER activity and have attracted extensive attention. However, 2D Ni-based MOFs are prone to agglomerate in the OER process. Therefore, the original 2D Ni-based MOFs have weak OER catalytic ability and poor stability. The introduction of heterogeneous metal atoms or compounds into Ni-based MOFs can adjust the electronic structure and enhance intrinsic activity.

4.1.1.2. Co-based MOFs. 2D Co-based MOFs showed high OER activity. Singh et al. prepared a 2D $[\text{Co}_6(\text{btc})_2(\text{DMF})_6(\text{HCOO})_6]$ (Co-MOF), which had a unique six-core core. [164] Co-MOF crystallizes in the triangular crystal system of $P\bar{3}$ space group. The η_{10} on Co-MOF was as low as 175 mV, which was attributed to the existence of $\text{Co}(\text{OH})_2$ and CoOOH as real active sites. The unique 2D hexanuclear cluster structure in Co-MOF may provide more active sites.

Compared with pure 2D Co-based MOFs, 2D hybrid Co-based MOFs with metal heteroatoms (Fe, Ni) have controllable morphology, controllable electronic structure and higher OER activity. Hou et al. synthesized CoFe-L, Co-L and CoNi-L ($\text{H}_2\text{L} = 5-((\text{pyridin-4-ylthio})\text{methyl})\text{isophthalic acid}$ ligands) by replacing cobalt ions with iron or nickel ions [165]. CoFe-L, Co-L and CoNi-L are isostructural, and Co-L crystallizes in monoclinic space group C_2/c . The η_{10} on CoFe-L, Co-L and CoNi-L was 355, 397, and 501 mV, respectively. The morphology and structure remained unchanged after continuous operation for 15 h. Fe doping increased the electron density of Co center and promoted the formation of OOH, the key intermediate of OER. Yan et al. synthesized 2D bimetallic $\text{Co}_x\text{Fe-NH}_2\text{-BDC}$ nanosheets, which crystallizes in $C2/m$ space group [166]. After optimization, $\text{Co}_x\text{Fe-NH}_2\text{-BDC}$ showed a low η_{10} of 280 mV. Part of the charge was transferred from Fe center to Co center, resulting in high electron density of Co center. The combination of Co and Fe can optimize the filling of e_g orbital, and the addition of Fe can also change the valence of Co^{2+} and the ability to accept electrons in the OER. Yao et al. synthesized 2D Co-based bimetallic Co-Ni/Fe@HPA-MOF (HPA = hypoxanthine) nanosheets by in situ hydrothermal methods [167]. The η_{10} on Co-Ni@HPA-MOF was 320 mV, mainly because the coupling effect between Co and Ni provided massive active sites. Most importantly, cobalt-based bimetallic MOFs can be directly used to catalyze OER without annealing treatment.

4.1.1.3. Cu-based MOFs. In addition to Ni and Co-based MOFs, Cu-based MOFs also have the potential as OER electrocatalysts.

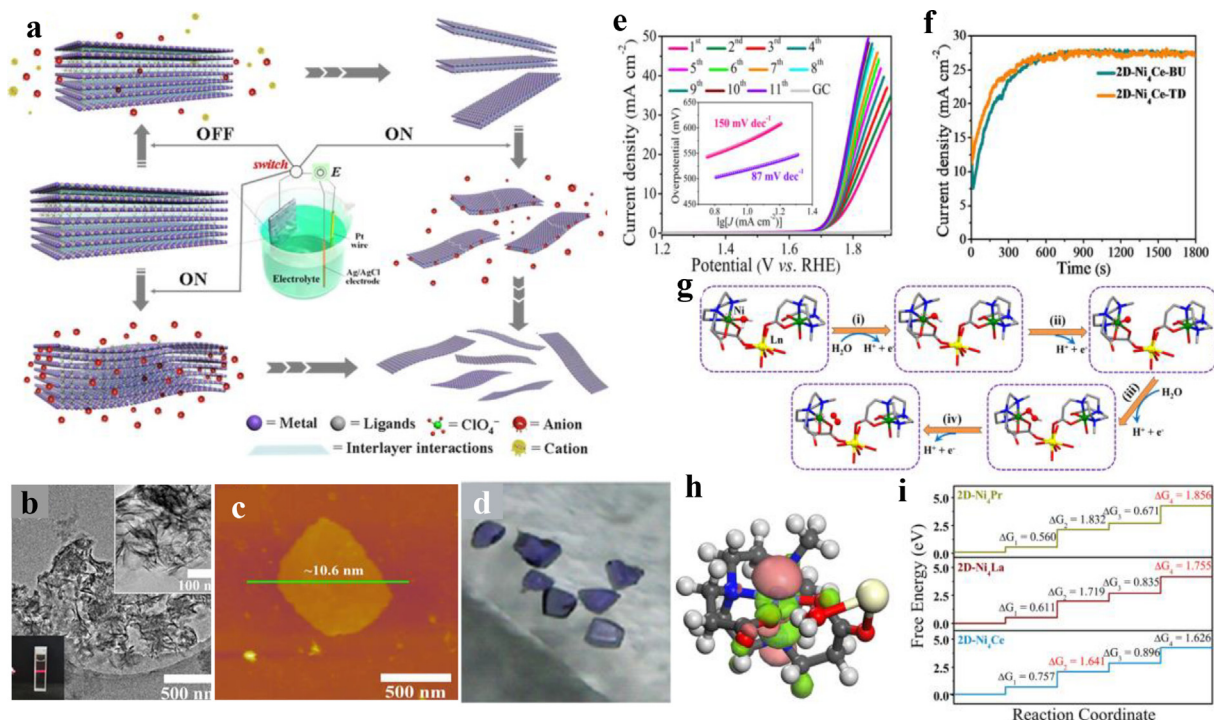


Fig. 14. (a) Diagram of the synthesis of ultra-thin MOFs. (b) TEM image of 2D-Ni₄Ce-NS. (c) AFM image of 2D-Ni₄Ce-TD. (d) Optical pictures of bulk 2D-Ni₄Ce. (e) LSV curve and Tafel slopes. (f) Chronoamperometry of 2D-Ni₄Ce-BU and 2D-Ni₄Ce-TD. (g) Four elementary OER steps. (h) Highest occupied molecular orbital (HOMO). (i) Standard free energy diagrams. Reproduced with permission from ref. [15]. Copyright 2020, American Chemical Society.

Yang et al. prepared Cu₃HITP₂/CF by growing 2D MOF on copper foam (CF) [168]. The structure of Cu₃HITP₂/CF is 2D needle-like and can run stably in alkaline solution. Cu₃HITP₂/CF can be used as OER and ORR bifunctional electrocatalysts. For OER, the η_{10} was 0.3 V, and the current density did not decrease significantly after 24 h. Using the synergistic effect between metals and 2D structure, Peng et al. introduced Cu into 2D Co-BDC to prepare CuCo-BDC, which had a unique book structure [169]. In the Cu-based bimetallic MOF catalyst, a variety of metals shared coordination, thus introducing more active structural defects. Moreover, the doping of Cu can increase the conductivity and water adsorption energy of the electrode, showing low interfacial resistance and fast charge transfer rate. The η_{10} on 2D CuCo-BDC was 340 mV, which was attributed to the synergistic effect between the two kinds of metals. Kim et al. synthesized Cu-Fe-NH₂ based MOF films without binder, which had 2D sheet structure [170]. Cu-Fe-NH₂ MOF showed a low η_{500} of 330 mV, and its chronopotentiometry decay loss was only 1.26 % at η_{500} for 24 h. Due to the synergistic effect of metal ions, multi-metal materials have received extensive attention. MOFs with high crystalline structures can be prepared by direct synthesis. Polymetallic electrocatalysts can also be prepared by introducing a second or third metal into MOFs. 2D MOF nanosheets have nanoscale thickness, which can accelerate ion exchange. In addition, they have soft crystal characteristics, and are flexible dynamic porous frameworks with convertibility. Fu et al. used Cu(BDC) as sacrificial template to introduce Co/Ni ions to synthesize CuCoNi trimetallic hybrids by impregnation method [171]. Ordered crystal structure of Cu(BDC) nanosheets transformed into amorphous structure and transformed from regular nanosheets to layered structure. The introduction of Co and Ni reduced the energy of Cu and made Cu atoms obtain more electrons, which will lead to the increase of local electric dipoles and reduce the dynamic barrier. The η_{10} on CoNi-Cu(BDC) was 327 mV (Table 1), which could be attributed to the synergistic effect of different metal ions and 2D layered structure.

4.1.2. 2D MOF-derived electrocatalysts for OER

Specific structural transformation can inhibit the aggregation of 2D MOFs, increase the active surface area, expose more active sites, and improve the accessibility of each active site, thereby enhancing the activity and stability. Non-noble metal nanocomposites usually refer to transition metal oxides, hydroxides, sulfides, phosphates and carbides. There are many kinds of 2D MOF derivatives for different electrocatalytic reactions.

4.1.2.1. Metal/alloys. 2D MOFs can be converted into metal/alloy

nanoparticles on carbon support by high temperature treatment under inert gas atmosphere. The carbonaceous component in the ligand provides high conductivity and supports high density of active sites for OER. Rodenas et al. chose 2D Co-based MOF as the precursor to introduce highly dispersed metal species, and combined it with exfoliated graphene with excellent electron transport properties to form CoTFBDC/EG (CoTFBDC = cobalt tetrafluoro-benzenedicarboxylate, EG = exfoliated graphene) composites [137]. After annealing at 250 °C, the EG-supported Co-based MOFs were decomposed into a hybrid with 1–5 nm thin sheets composed of metallic nanocrystals. According to XPS analysis, the fluorine introduced in 2D Co-based MOF can overflow during annealing, which is helpful for the release of O₂ on the surface of the electrocatalyst. In 1 M KOH, the Tafel slope of CoTFBDC/EG was as low as 39.8 mV dec⁻¹. Li et al. prepared nanoflower-like MOF derivatives (FeNi@CNF and CoNi@CNF) (Fig. 15a) [172]. They used 2D bimetallic MOF-FeNi and MOF-CoNi with nanoflower morphology as precursors (Fig. 15b, e). After high temperature pyrolysis, the original morphology was retained (Fig. 15c, f), and the surface of carbon nanostructures became uneven, exposing more active sites. The diameter of the hollow carbon nanotubes was about 20 nm (Fig. 15d and g). According to XPS analysis, some Fe atoms were inserted into Ni crystal to form FeNi alloy. FeNi metal nanoparticles coated at the end of carbon nanotubes can form the host-guest effect and improve the catalytic performance of the car-

Table 1
OER performance comparison of 2D MOF electrocatalysts.

Electrocatalyst	Substrate	Mass loading (mg cm ⁻²)	Electrolyte	η_{10} (mV)	Stability (h)	Ref.
Ni-MOF	GCE ^a	/	0.1 M KOH	370	5.5	[161]
NiPc-MOF	FTO ^b	0.0076	1.0 M KOH	270	50	[162]
NiFe-MOF-74	NF ^c	/	1.0 M KOH	208	15	[22]
NiCo-MOF/NF	NF	/	1.0 M KOH	270	8.3	[163]
5 % Ni/Co-MOF	CFP ^d	0.2	1.0 M KOH	310	12	[30]
[Co ₆ (btc) ₂ (DMF) ₆ (HCOO) ₆]	GCE	/	1.0 M KOH	175	10	[164]
Co-MOF	GCE	0.1	1.0 M KOH	350	2.2	[144]
Co-MOF	GCE	0.225	0.1 M KOH	397	15	[165]
CoFe-MOF	GCE	0.225	0.1 M KOH	355	15	[165]
Co ₃ Fe-MOF	GCE	0.4	0.1 M KOH	280	10	[166]
Co-Fe@HPA-MOF	GCE	/	1.0 M KOH	370	/	[167]
MOF-Fe/Co (1:2)	GCE	/	1.0 M KOH	238	13.8	[178]
Co-Ni@HPA-MOF	GCE	/	1.0 M KOH	320	/	[167]
FeCoNi-MOFs	GCE	0.25	1.0 M KOH	254	100	[179]
CoNi-MOF	GCE	0.225	0.1 M KOH	501	15	[165]
CuCo-MOF	NF	0.43	1.0 M KOH	340	24	[170]
CuNi-Cu(BDC)	GCE	0.38	1.0 M KOH	327	8	[171]

^a GCE: glassy carbon electrode, ^b FTO fluorine-doped tin oxide; ^c NF: nickel foam, ^d CFP: Carbon fiber paper.

bon layer. BET measurement showed that there were micropores/mesopores, and the specific surface area was about 290.1 m²/g, which was beneficial to the exposure of active sites. In 1 M KOH, the η_{10} on FeNi@CNF was 356 mV, which was lower than that of CoNi@CNF (388 mV) (Fig. 15h). After 24 h of continuous operation, the voltage increased slightly (Fig. 15i).

4.1.2.2. Metal oxides. In general, metal oxides can be derived from 2D MOFs when the annealing temperature is 200–600 °C. Cobalt-based oxides have the advantages of high theoretical capacity, low cost, abundant natural resources and simple preparation, which can be used in energy storage and conversion fields. Zhang et al. annealed 2D Co₂(3,5-di(pyridin-4-yl)-4H-1,2,4-triazol-4-amine) (Co-MOF) in air to prepare layered NL-Co₃O₄ with thickness of about 70 nm (Fig. 16a) [158]. When the annealing temperature was 400 °C, the obtained NL-Co₃O₄ retained the layered structure of Co-MOF, and possessed a loose and porous structure (Fig. 16b-e). This unique structure can effectively alleviate volume expansion and expose more active sites. According to the nitrogen adsorption and desorption tests, NL-Co₃O₄ is a typical mesoporous material with a pore size of about 2.6 nm. In 1 M KOH, the η_{10} on NL-Co₃O₄ was 420 mV, and its Tafel slope was 69.2 mV dec⁻¹, which was better than that of RuO₂ (428 mV, 86.6 mV dec⁻¹) (Fig. 16f, g). After 15 h of continuous operation, the current density did not change significantly, and the layered structure was also maintained. Combining 2D MOFs with carbon to prepare metal oxide/C nanosheets can not only increase the conductivity, but also increase the number of active sites, which is of great help to improve the catalytic activity. Li et al. prepared Co₃O₄/C_{BDC}, NiO/C_{BDC} and Cu₂O/S-C_{TDC} (TDC = 2,5-thiophenedicarboxylate) by combining 2D structure with porous carbon [26]. To compare the effects of metal oxides/carbon (MO_x/C, M = Co, Ni, Cu) prepared in different dimensions on OER activity, they also chose 1D/3D MOF as the precursor. Taking 2D Co₃O₄/CBDC as an example, the η_{10} of 1D Co₃O₄/C_{BTC}, 3D Co₃O₄/C_{DHTP} and 2D Co₃O₄/CBDC was 295, 260 and 208 mV, respectively. The combination of 2D array structure and C helps to form *OH intermediates and promote the first step reflection of OER. Compared with single metal oxides, bimetal or trimetal oxides derived from 2D MOFs have more unique heterostructures. Hu et al. doped Fe into Co₂(C₄H₆N₂) (C₄H₆N₂ = 2-methylimidazole) with abundant oxygen vacancies (V_O), and then carbonized it to obtain “cheese-like” Fe/Co-carbon nanosheets [173]. After carbonization, the triangular structure did not change, but the original smooth surface became rough,

forming more hollow and porous structures. The doping of Fe can fill the oxygen vacancy and a unique heterostructure can be achieved. After optimization, the η_{10} on Fe₁Co₃V₀-800 was 260 mV. Metal oxides derived from 2D MOFs are easy to maintain stable crystal structure and can be produced on a large scale.

4.1.2.3. Metal chalcogenides. Transition metal sulfides derived from 2D MOFs have tunable metal-sulfur coordination environment. Dou et al. synthesized 2D MOF ([Ni₃(OH)₂(1,4-BDC)₂(H₂O)₄)]₂H₂O, or Ni-BDC) by in-situ growth method, and then modified it with NiS to obtain Ni-BDC@NiS composite (Fig. 17a-c) [123]. The morphology and structure of MOF were retained by partial vulcanization, and the produced NiS improved the electronic conductivity. However, the array structure was unstable at high temperature vulcanization. Ni-BDC@NiS with the highest degree of vulcanization could be obtained at 90 °C, which showed a low η_{20} of 330 mV (Fig. 17d). NiS generated by layered MOF is conducive to the rapid transfer of charge and the high adsorption of water. This composite structure will form the interaction of interfaces and provide strong structural integrity. Ma et al. synthesized nitrogen-doped Ni-Ni₃S₂@carbon nanoplates by pyrolysis of 2D MOFs [118]. They used anti-anion SO₄²⁻ for self-sulfidation without additional sulfur source and pyridine as a 2D inhibitor. After pyrolysis treatment, the nanosheets composed of carbon matrix were retained, and the Ni-Ni₃S₂ nanoparticles were embedded. The synergistic effect of the alloy core and the 2D morphology promoted the charge transfer, and changed the electronic properties. Heterogeneous interfaces can be formed not only in polymetallic compounds, but also in monometallic compounds. Pan et al. synthesized silver-ear MOFs (TLMs), and obtained heterogeneous CoS₂/CoS nanosheets by vulcanization [174]. Due to the mismatch between CoS₂ and CoS, a clear interface leads to rich defects and disordered structures. The η_{10} on CoS₂/CoS nanosheets was 269 mV, which was lower than that of CoS₂ (296 mV) and CoS (399 mV). CoS₂/CoS nanosheets inherited the unique structure of the precursor, which changed the electron interaction during the vulcanization process, thus promoting the electron transfer.

4.1.2.4. Metal hydroxides. The large surface area, abundant surface atoms and convenient charge transport of transition metal (oxygen-containing) hydroxide nanosheets make them efficient electrocatalysts for the OER. Layered double hydroxides (LDHs) have high specific surface area and unique layered structure, which were widely used as OER electrocatalysts [175]. However, the

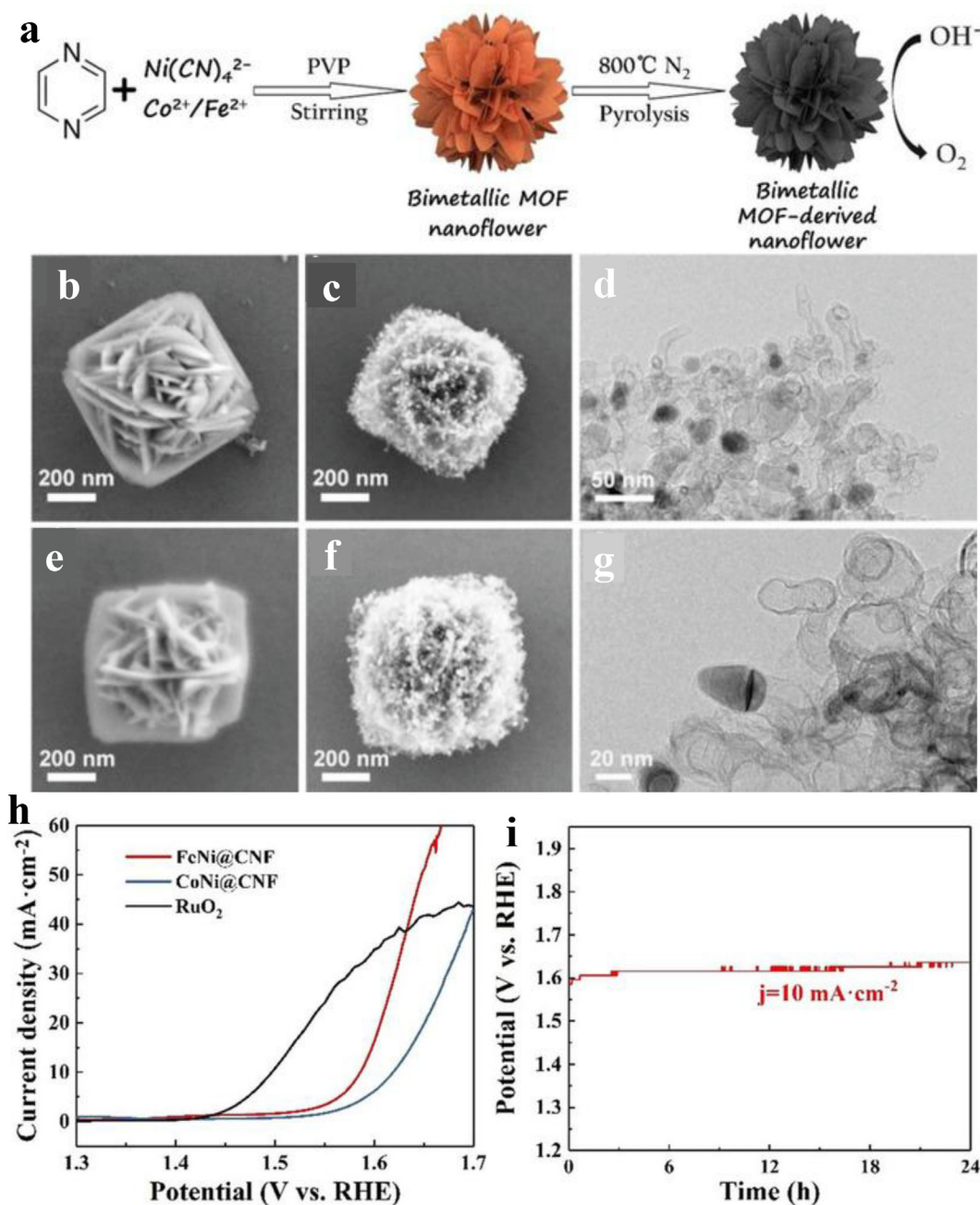


Fig. 15. (a) Schematic illustration. SEM image of (b) MOF-FeNi and (c) FeNi@CNF. (d) TEM of FeNi@CNF. SEM of (e) MOF-CoNi and (f) CoNi@CNF. (g) TEM of CoNi@CNF. (h) LSV. (i) V-t curve. Reproduced with permission [172]. Copyright 2019, Wiley-VCH.

synthesis of LDH is difficult and its structure is easy to collapse. Using MOFs with 2D structure as precursors, ultra-thin LDH electrocatalysts can be prepared by using controllable interlayer conversion strategy. Li et al. used Hofmann-MOF with unique structure to synthesize ultra-thin FeNi-LDH under the condition of hydrogen bubble assistance (Fig. 18a-c) [176]. The FeNi-py LDH synthesized by adding pyridine (py) ligand has a sheet shape, and its thickness is about 6 nm. The atomic ratio in the MOF precursor and LDH did not change. Due to the synergistic effect of bimetal and the unique layered structure, the η_{10} on FeNi-py LDH was 238 mV (Table 2). The electrocatalytic performance can be improved by forming a polymetallic structure. Co and Ni in CoNi-based hydroxide have synergistic effect. When the third metal Fe is added, more active sites will be generated. Yu et al.

synthesized 2D layered trihydroxide (LTH) nanosheets and CoNiFe-LTH nanosheets by MOF mediated method (Fig. 18d) [177]. CoNiFe-LTH presents petaloid morphology assembled from ultrathin nanosheets. After optimization, the η_{10} on CoNiFe-LTH was as low as 262 mV (Fig. 18e, f). In addition to Fe, transition metals such as Cd, Ce, Cu and Mn can also be added.

Most of 2D MOF derivatives can retain 2D structure of the precursors by appropriate treatment, while the surface morphology might change. For instance, FeNi@CNF and CoNi@CNF obtained after high temperature annealing and acid leaching still retained the nanoflower morphology, but the surface became uneven [172]. For NL-Co₃O₄ [158], Co₃O₄/CBDC [26] and Fe₁Co₃/V₀-800 [173], the 2D morphology of the precursors was retained after high temperature carbonization, while the smooth surface became

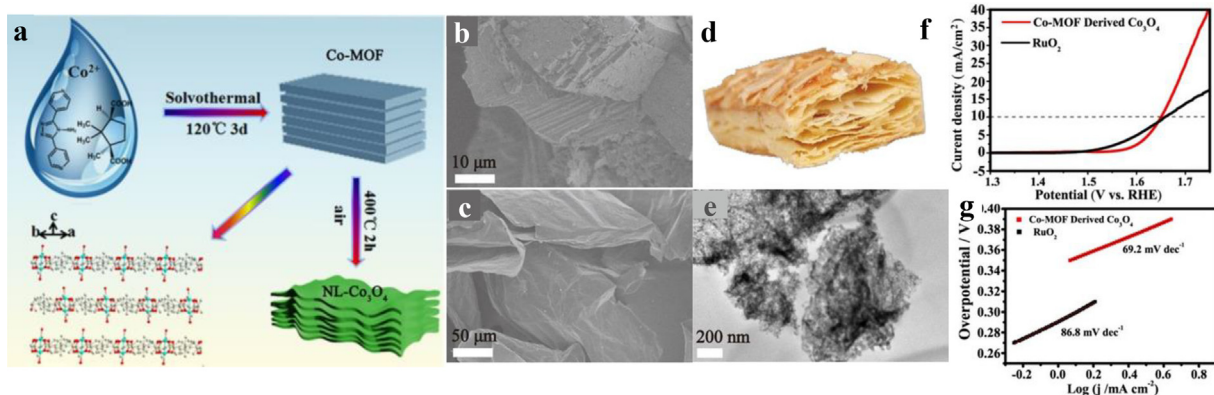


Fig. 16. (a) Illustration of the synthesis of NL- Co_3O_4 . SEM of (b) Co-MOF and (c) NL- Co_3O_4 . (d) The food of Napoleons. (e) TEM of NL- Co_3O_4 . (f) LSV plots. (g) Tafel plots. Reproduced with permission [158]. Copyright 2020, Wiley-VCH.

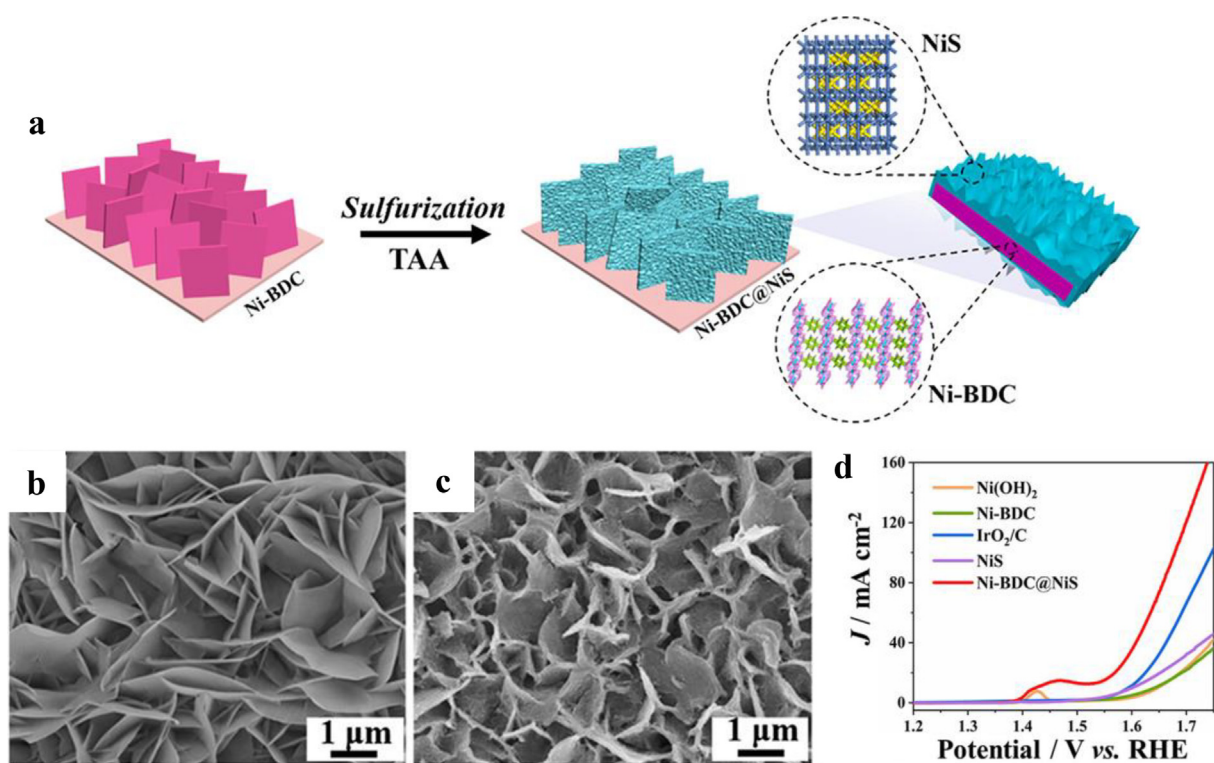


Fig. 17. (a) The fabrication of the Ni-BDC@NiS. SEM images of (b) Ni-BDC and (c) Ni-BDC@NiS. (d) LSV curves. Reproduced with permission [123]. Copyright 2019, American Chemical Society.

rough and more porous structures were formed. For metallic sulfur compounds, the well-aligned Ni-BDC was transformed into Ni-BDC@NiS with hierarchical structure after vulcanization, while the original array structure was still retained [123]. For metal hydroxides, MOF-derived FeNi-py LDH [176] exhibited 2D layered structure, and CoNiFe-LTH [177] exhibited petal-like morphology assembled by nanosheet.

4.2. Hydrogen evolution reaction

Hydrogen production from water electrolysis has developed rapidly in recent years, and the technology has been relatively mature. The raw material is water, the reaction process is environmentally clean, and there is no CO_2 in the product. The whole reaction is very consistent with the concept of sustainable

development. Therefore, it is a feasible mainstream method to develop water electrolysis to prepare hydrogen. HER is a two-electron transfer process at the cathode of water splitting (Fig. 19). The reaction mechanisms in both acidic and alkaline solutions are basically the same, and only the source of protons is different, namely protons in acidic solution from H_3O^+ , while protons in alkaline solution from H_2O . Electron transfer and hydrogen desorption are two essential and decisive steps. The dynamics of HER is experimentally determined by the Tafel slope. Theoretically, the electrochemical HER kinetics can be reflected by the hydrogen adsorption free energy (ΔG_{H^+}). The greater the absolute value of ΔG_{H^+} is, the worse the hydrogen evolution performance of the catalyst is. Only when the absolute value of ΔG_{H^+} is close to zero, the adsorption force and desorption force reach the balance suitable for the reaction, and the hydrogen evolution performance of the

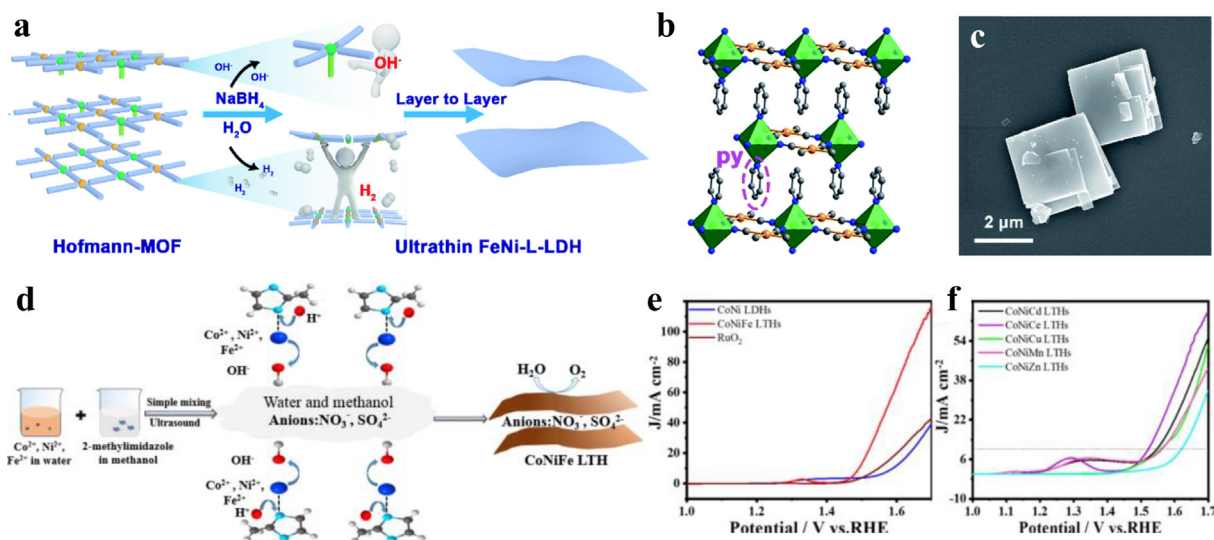


Fig. 18. (a) Schematic illustration of FeNi-LDH. The crystal structure (b) and morphology (c) of FeNi-py-MOF. Reproduced with permission [176]. Copyright 2021, Royal Society of Chemistry. (d) Schematic illustration of CoNiFe-LTH. (e, f) LSV. Reproduced with permission [177]. Copyright 2021, Elsevier Ltd.

Table 2

OER performance comparison of 2D MOF derived electrocatalysts.

Electrocatalyst	Substrate	Mass loading (mg cm ⁻²)	Electrolyte	η_{10} (mV)	Stability (h)	Ref.
Ni@NC-800	GCE	0.31	1.0 M KOH	280	10	[46]
Ni-BDC/Ni(OH) ₂	GCE	/	1.0 M KOH	320	20	[180]
NiO/C _{BDC}	GCE	/	1.0 M KOH	285	36	[26]
Ni-Ni ₃ S ₂ @C	GCE	0.2	1.0 M KOH	284.7	8	[118]
FeNi@CNF	NF	/	1.0 M KOH	356	12	[172]
(Fe ₂ O ₃) _{0.36} @Ni-MOF	CFP	1.0	1.0 M KOH	230	20	[181]
NiFe(20Ni)-MOF/NFF	NF	0.2	1.0 M KOH	226	20	[182]
Ru-NiFe/NF	NF	1.0	1.0 M KOH	179	20	[183]
Ni-MOF@Fe-MOF	GCE	0.2	1.0 M KOH	265	/	[5]
FeNi ₃ -Fe ₃ O ₄ NPs/MOT-CNT	GCE	0.28	1.0 M KOH	234	20	[184]
FeNi@OCNC	NF	/	1.0 M KOH	300.4	12	[172]
CoNi ₄₀ -MOFNs	GCE	0.2	1.0 M KOH	346	20	[185]
AuNRs/NiCo-MOFs	GCE	0.05	1.0 M KOH	345	/	[186]
CoNi ₂₀ -MOF Ns@MX	GCE	0.2	1.0 M KOH	379	20	[185]
α -Co(OH) ₂ nanosheets	GCE	0.25	0.1 M KOH	340	12	[187]
Co-BPDC/Co-BDC-3	GCE	0.28	1.0 M KOH	335	80	[188]
NL-Co ₃ O ₄	GCE	/	1.0 M KOH	430	15	[158]
Co ₃ O ₄ /C _{BDC}	GCE	/	1.0 M KOH	208	36	[26]
Co ₃ S ₈ @TDC-900	GCE	/	1.0 M KOH	330	7	[59]
CoS ₂ /CoS	GCE	/	1.0 M KOH	269	22	[174]
Co-CuTCPP/rGO	GCE	0.12	1.0 M KOH	396	10	[189]
Cu ₂ O/S-C _{TDC}	GCE	/	1.0 M KOH	313	24	[26]
Fe ₁ Co ₃ /V _O -800	CC ^e	/	1.0 M KOH	260	15	[173]
FeNi-py-LDH	GCE	/	1.0 M KOH	238	15	[176]
CoNiFe-LTH	GCE	/	1.0 M KOH	262	50	[177]

^e CC: carbon cloth.

catalyst is excellent. At present, the ΔG_{H^+} of precious metals such as Pt, Pd, Ru, Ir and Rh is close to 0, and the hydrogen evolution ability is excellent, but their cost is high and they cannot be used in large scale [190]. 2D MOF nanosheets and their derivatives have become new catalytic materials for HER due to their unique physical and chemical properties.

4.2.1. 2D MOFs for HER

4.2.1.1. Single-metal MOFs. 2D nanosheets have larger surface area, more active sites and shorter migration length than bulks. Ruiz-Molina et al. synthesized a complex [Cu(2,5pydc)(H₂O)]_n·2H₂O (pydc = 2,5-pyridine dicarboxylic acid), and then obtained thin nanosheets (NSs) by ultrasonic stripping method (Fig. 20a) [192]. The [Cu(2,5pydc)(H₂O)]_n·2H₂O crystallizes in triclinic space group

Pi. They modified the traditional synthesis method to produce larger layered blue crystals (Fig. 20b). Fig. 20c showed that the nanosheets have a wider thickness distribution in the range of 50–200 nm. Compared with the samples before stripping, NSs had a lower η_{10} of 340 mV for the HER (Fig. 20e, f). Cu (II) ions were coordinated with carboxyl and pyridyl groups in two modes, forming a linear high-density accumulation of metal center along the 2D layer, while water molecules stabilized the structure through hydrogen-bond interaction.

The introduction of non-metal elements into MOFs can enhance the affinity between reactants and intermediates. The electron absorption effect of halogen atoms and the lone pair electrons will show the resonance effect. Li et al. synthesized three 2D [Co(X₄-pta)(bpy)(H₂O)₂]_n (X = F, Cl and Br), which crystallize in

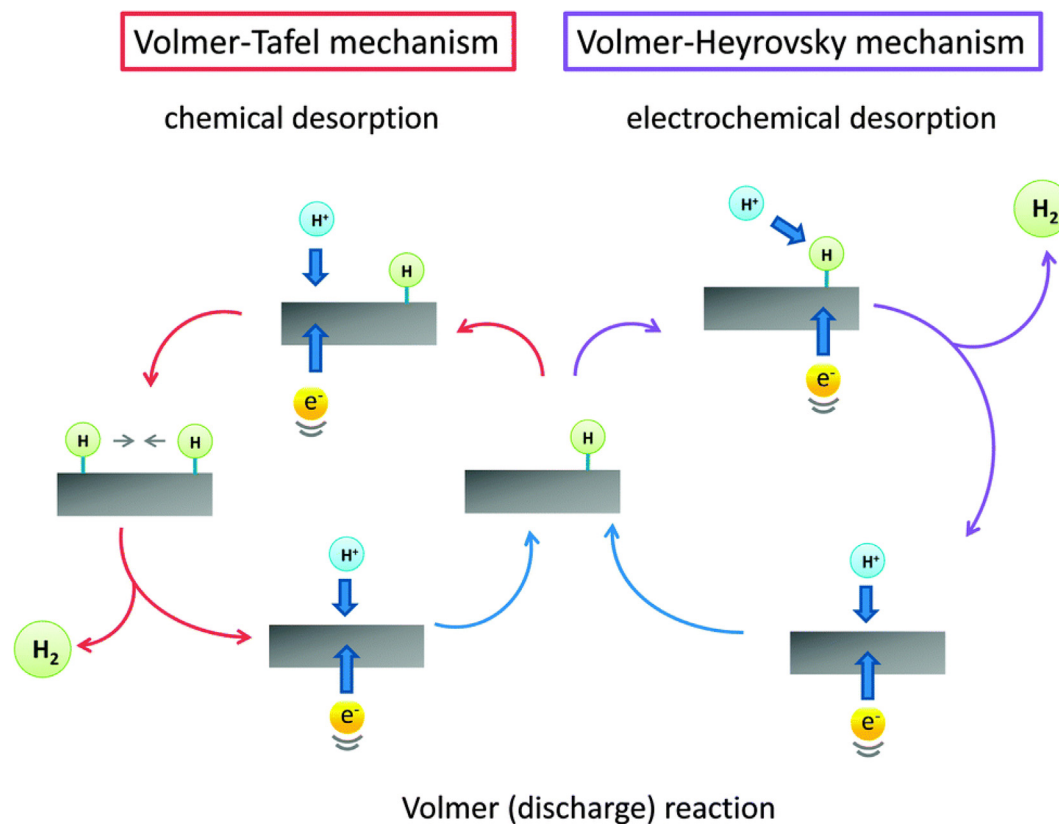


Fig. 19. HER mechanism in acidic media. Reproduced with permission [191]. Copyright 2014, Royal Society of Chemistry.

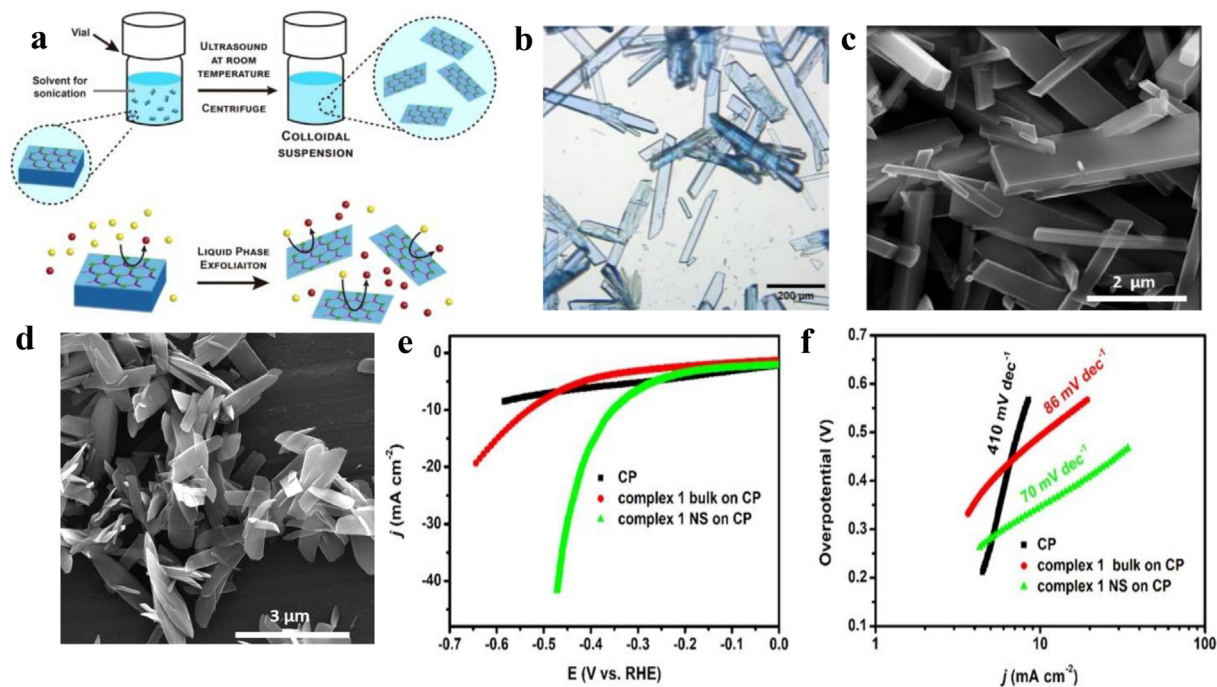


Fig. 20. (a) Schematic diagram. (b) Crystal optical images. (c) High magnification SEM image. (d) SEM images of NSs in aqueous colloidal suspension. (e) HER polarization plots. (f) Tafel plot. Reproduced with permission from ref. [192]. Copyright 2021, Elsevier Ltd.

orthorhombic *Pccn* space group [193]. In 0.5 M H_2SO_4 , the catalytic activity of pure $\text{Co-Cl}_4\text{-MOF}$ was better than that of pure $\text{Co-Br}_4\text{-MOF}$. XPS measurement showed that after HER test, the binding

energies of $\text{Co } 2p_{3/2}$ and $\text{Co } 2p_{1/2}$ showed a positive shift of 0.4 eV, while $\text{Cl } 2p_{3/2}$ and $\text{Cl } 2p_{1/2}$ showed a negative shift of 0.05 eV, indicating that halogen atoms were helpful to desorb H

from the Co site. Adding acetylene black (AB) to $[\text{Co}(\text{X}_4\text{-pta})(\text{bpy})(\text{H}_2\text{O})_2]_n$ can enhance the conductivity. AB&Co-Cl₄-MOF (3:4) showed an η_{10} of 283 mV.

4.2.1.2. Bimetallic/polymetallic MOFs. Adding Ru to MOFs can not only retain the original morphology and structure, but also increase electrochemical active sites. Selecting a suitable substrate is conducive to increasing conductivity. Wang et al prepared Ru-doped $\text{Ni}_2(\text{BDC})_2\text{TED}$ (TED = triethylenediamine) MOF, and then synthesized NiRu-MOF/NF (Fig. 21a) [194]. NiRu-MOF/NF was vertically grown on nickel foam with a thickness of only 10 nm (Fig. 21b). Compared with $\text{Ni}_2(\text{BDC})_2\text{TED}$, the peaks of $\text{Ni}^{2+} 2p_{3/2}$ and $\text{Ni}^{2+} 2p_{1/2}$ in the NiRu-MOF moved to a slightly lower binding energy, indicating that Ru doping changed the electronic structure of Ni cations. In 1.0 M KOH, NiRu-MOF/NF had a low η_{100} of 156 mV. Moreover, the conversion frequency (TOF) of NiRu-MOF was 1.06 s^{-1} (Fig. 21c-f). In the subsequent research, more attention should be paid to the control/optimization of crystal size, morphology and composition, the improvement of stability, and the enhancement of the conductivity within MOF crystals and between MOF crystals and substances. Lin et al. synthesized NiFe(dobpdc) MOF with yarn spherical structure, which showed a 2D tightly coupled spherical structure [195]. The dobpdc^{4-} (4,4'-dioxidobiphenyl-3,3'-dicarboxylate) can contribute more π electrons to metals, and the bimetal interact to jointly promote the overall water splitting. In HER, NiFe(dobpdc) achieved low η_{10} of 113 mV and η_{100} of 170 mV. Cui et al. prepared bimetallic NiFe-DOBDC ($\text{H}_4\text{DOBDC} = 2,5$ -dihydroxyterephthalic acid) (NiFe-MOF-74) nanosheets on nickel foam, which had interconnected honeycomb networks

[22]. In HER, the η_{10} on NiFe-DOBDC-74 was 208 mV and the η_{100} was 240 mV. According to the XPS results, the binding energy of Ni $2p_{3/2}$ in NiFe-DOBDC-74 was negatively shifted by 0.2 eV, while that of Fe $2p_{3/2}$ was positively shifted by 0.8 eV, indicating that electrons were transferred from Fe to Ni, which led to a decrease in the number of d-electron orbits near Fe. The synergistic effect between Ni and Fe modulated the morphology and electronic structure of NiFe-MOF-74, leading to enhanced electrocatalytic activity. Chen et al. synthesized a conductive lamellar MOF with double active sites (Ni and Fe) and a thickness of about 1.35 nm (Fig. 21g, h) [196]. The conductivity of NiFe(2,5-thiophene dicarboxylic acid) (NiFe-MOF) array was about $35 \pm 8 \text{ S m}^{-1}$. In HER, the η_{10} on NiFe-MOF was only 68 mV, and the η_{500} was 356 mV. DFT calculations revealed that H^* desorption was the step determining the potential, and Ni sites promoted the desorption of H^* , and the coexistence of Ni and Fe can bring synergistic effect and promote the HER (Fig. 21i).

4.2.2. 2D MOFs derived electrocatalysts for HER

The d-orbitals of transition metal oxides (TMOs) can be adjusted, and multi-interface heterostructures can be constructed by deriving from 2D MOFs. Song et al. prepared Ru-doped cobalt-nickel oxide heterostructure nanosheets ($\text{Ru-Co}_3\text{O}_4\text{-NiO-NF}$) derived from MOF (Fig. 22a) [197]. The obtained $\text{Ru-Co}_3\text{O}_4\text{-NiO-NF}$ effectively inherited the favorable morphology of Co-2-Melm precursor, while maintaining the mechanical strength of NF skeleton. Ru doping existed in the form of low content hetero-doping, which reduced the crystallinity of Co_3O_4 . The η_{10} on the $\text{Ru-Co}_3\text{O}_4\text{-NiO-NF}$ was 44 mV (Fig. 22b), and the

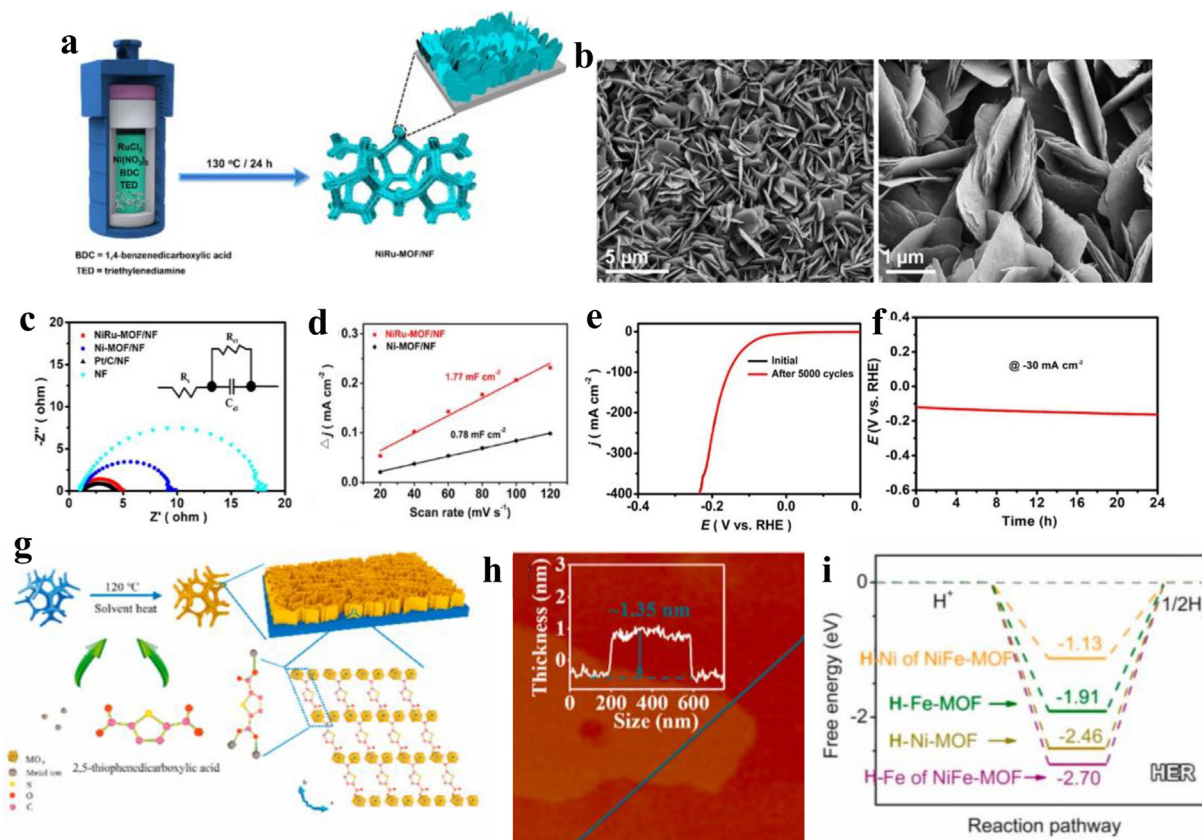


Fig. 21. (a) Schematic diagram of synthesis of NiRu MOF nanosheets on nickel foam. (b) SEM images of the NiRu-MOF/NF. (c) Nyquist plots. (d) Plots of current density difference (Δj) against scan rate. (e) LSV curve before and after 5000 cycles. (f) v-t curve at -30 mA cm^{-2} current density. Reproduced with permission from ref. [194]. Copyright 2020, American Chemical Society. (g) Synthesis procedure of NiFe-MOF. (g) AFM and height profile. (i) HER free energy diagrams. Reproduced with permission [196]. Copyright 2021, Elsevier Ltd.

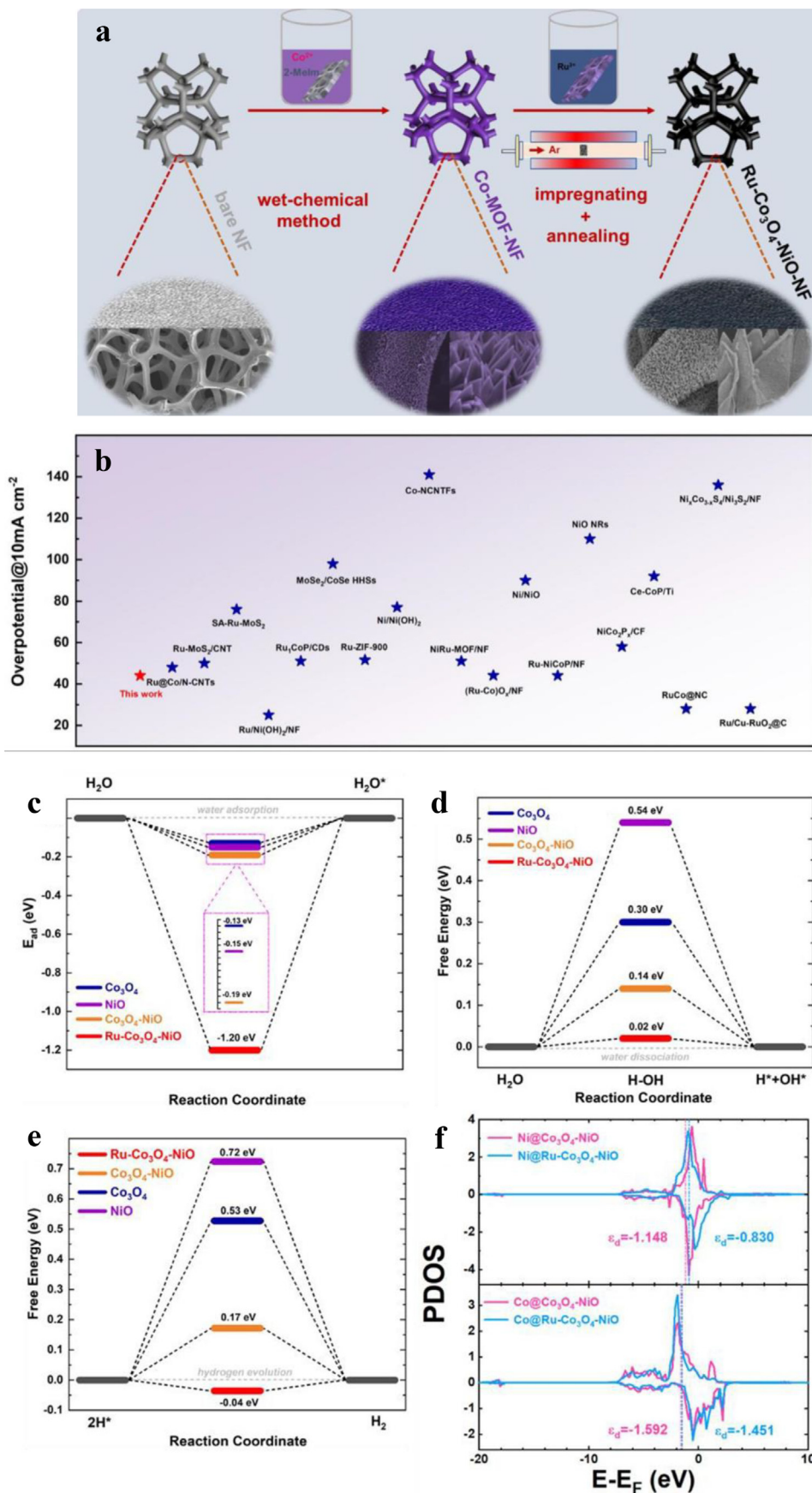


Fig. 22. (a) Schematic illustration. (b) The comparison of overpotential. (c) Water adsorption energy diagram. (d) Water dissociation energy diagram. (e) Hydrogen adsorption free energy diagram. (f) PDOS. Reproduced with permission [197]. Copyright 2021, Elsevier Ltd.

η_{100} was as low as 115 mV. According to XPS, both the heterogeneous interfaces of Ru and Co_3O_4 -NiO could introduce strong electron interaction and enhance the dynamics of charge transfer. The doping of Ru reduced ΔG_{H^+} to -0.02 eV, and the ΔG_{H^+} of Co_3O_4 -NiO was also reduced to 0.17 eV (Fig. 22c-f), which was beneficial to enhance the catalytic activity of HER. MOF-derived porous carbon composites (MOFC) exhibit high catalytic activity due to the uniform doping of active heteroatoms. However, most MOFC are formed by high temperature carbonization, and the aggregation of metal particles is prone to occur during pyrolysis. Wang et al. induced 2D MOF nanosheets with CoO nanowalls as template to prepare Ni@CoO@Co-MOF (Co-MOF: $[\text{Co}(\text{bimpy})(\text{p-bdc})(\text{H}_2\text{O})]_n$), and then pyrolyzed it to form Ni@CoO@Co-MOFC [198]. The Ni@CoO@Co-MOFC retained the 2D morphology of the precursor, but the surface became curved. Metal particles are prone to aggregate in bulk MOFs during pyrolysis, but the aggregation of nanoparticles can be avoided or reduced in 2D MOF nanosheets during pyrolysis due to well-arranged nanoarray structure. The η_{10} on Ni@CoO@Co-MOFC was 138 mV. The presence of Co can promote the adsorption of H atoms, while CoO can promote the adsorption of hydrolyzed $-\text{OH}$. The synergistic effect can enhance the catalytic activity of HER.

In terms of practical application, alkaline HER is more practical than acidic HER, because acid fog is easily generated in acidic environment and hydrogen is polluted. However, the reaction rate of HER in alkaline environment is lower. Theoretically, molybdenum disulphide exhibits the closest hydrogen adsorption free energy to Pt and high corrosion resistance, and thereby it could replace noble metal electrocatalysts to catalyze HER [199]. There are four polycrystalline types of molybdenum disulfide, among which, the triangular phase of molybdenum disulfide can provide more active sites for HER. Qiao et al. synthesized 2D-Co-BDC/MoS₂ hybrid nanosheets (BDC: 4-phthalate, $\text{C}_8\text{H}_4\text{O}_4$) [200]. They first converted bulk MoS₂ into MoS₂ nanosheets, and then deposited Co-BDC on MoS₂. The obtained Co-BDC/MoS₂ still retained the characteristics of 2D nanosheets. However, under the influence of Co-BDC, molybdenum disulfide was transformed from hexagonal phase (2H) to triangular phase because Co-BDC provided electrons to promote the phase transformation. Co-BDC promoted the dissociation of water, while MoS₂ promoted the generation of hydrogen. In addition to the high catalytic activity of MoS₂, Ni₃S₂ is also widely concerned because of its high conductivity and inherent metal properties. The S sites at the edge of Ni₃S₂ are easy to form S-H bond, which is conducive to the adsorption of hydrogen intermediates. Cheng et al. prepared Ni₃S₂@Co-(2-mlm)/CP by electrodeposition of honeycomb Ni₃S₂ nanosheets on the surface of 2D Co-(2-mlm) (2-mlm = 2-Methylimidazole) as a template [29]. The 2D Co-(2-mlm) nanosheets showed smooth nanosheets on the CP (carbon paper) surface with a thickness of about 150 nm. After Ni₃S₂ was loaded by in-situ electrodeposition, the leaf shape remained, but the smooth surface became rough and a honeycomb structure was grown. MOF array as the template can avoid the aggregation of Ni₃S₂ particles, thus providing more HER active sites. The η_{10} on Ni₃S₂@Co-MOF/CP was 140 mV (Table 3), and the η_{130} was only 395 mV, indicating that it has great potential for industrial application.

Transition metal phosphides have a catalytic mechanism similarly to hydrogenase for HER. When transition metal phosphides are combined with nano-substrates, the nano-substrates can improve the overall electrical conductivity. Cobalt phosphate (CoP) has attracted much attention in HER electrocatalysis due to its high activity and durability [201]. Zheng et al. embedded CoP on the surface of carbon nanoparticles to form CoP@C [202]. They prepared four kinds of CoP@C-Y with different proportions of Co^{2+} and 2-dimethylimidazole (2-MeIM). When Co^{2+} :2-MeIM was 2:1 (CoP@C-1) or 1:1 (CoP@C-2), the product was light yellow. When

Co^{2+} :2-MeIM was 1:2 (CoP@C-3) or 1:4 (CoP@C-4), the product was dark purple, as shown in Fig. 23a, b. Fig. 23c shows that CoP@C-2 has a rough surface due to the coverage of CoP nanoparticles. In Fig. 23d, the lattice spacings of 0.279 and 0.186 nm correspond to the (001) and (211) crystal planes of CoP, respectively. The η_{10} on CoP@C nanosheets was 236 mV (Fig. 23e, f). According to DFT calculations, the P-top sites on (011) and (211) planes of CoP were the main active sites (Fig. 23g, h), and the water dissociation on CoP (211) plane was more favorable than that on (011) plane. In other words, CoP (211) was more active for HER (Fig. 23i). Under acidic conditions, the ΔG_{H^+} values on (011) and (211) surfaces were -0.17 eV and -0.05 eV, respectively (Fig. 23j).

4.3. Oxygen reduction reaction

Fuel cell is considered as one of the most effective green energy conversion technologies due to its advantages of low pollution and high efficiency. Oxygen reduction reaction (ORR) occurs at the cathode of fuel cells, and its reaction mechanism is complex, which can be divided into four-electron pathway and two-electron pathway [219]. Compared with the two-electron pathway, the four-electron pathway has higher output voltage and energy conversion efficiency, but the energy barrier of the reaction is also relatively high. Pt noble metal catalysts have the optimal ORR performance, which is mainly manifested in the four-electron reaction pathway [220]. ORR catalysts need to meet the conditions of good conductivity, electrochemical stability and high catalytic activity. 2D MOFs can meet these requirements after appropriate modification. Hence, researchers have studied various MOFs, and found that Al, Mg, Mn, Fe, Co, Ni, and Cu-based MOFs show good ORR catalytic activity.

4.3.1. 2D MOFs for ORR

ORR has slow kinetics and it is a huge challenge to prepare high-performance catalytic materials for this reaction. Platinum-based catalysts are the most active and widely used materials for the ORR, but the scarcity of the precious metal Pt and the high cost limit their widespread use, and thereby it is important to develop new ORR electrocatalysts to replace the precious metal Pt. Zhao et al. prepared 2D conjugated MOF $\text{Co}_3(\text{HADQ})_2$ using 2,3,6,7,10,11-hexaamine disyoquinoline (HADQ) as the building block (Fig. 24a-c), which was a black powder with 2D stacking structure [221]. $\text{Co}_3(\text{HADQ})_2$ had a high conductivity of 8385.744 S/m. In addition, the Co-N₄ structure is present in $\text{Co}_3(\text{HADQ})_2$, which can be used as the active site of ORR. In 0.5 M H₂SO₄, the onset potential on the $\text{Co}_3(\text{HADQ})_2$ was 0.85 V (vs RHE), the half-wave potential was 0.835 V (vs RHE), and the current density dropped by only 5.4 % after 20,000 cycles (Fig. 24d). According to DFT studies, $\text{Co}_3(\text{HADQ})_2$ has a planar and porous structure, which favors the dispersion of ions and protons. Each Co-N₄ sequence in $\text{Co}_3(\text{HADQ})_2$ is covalently bound to two pyrazine rings, and the high electron delocalization between the benzene units gives $\text{Co}_3(\text{HADQ})_2$ high conductivity. The η_{ORR} on the Co- site was smaller than that on the pyridine N-site, indicating that ORR occurred preferentially at the Co-site (Fig. 24e, f).

The coupling effect of the interaction between multi-metal sites increases the catalytic activity of ORR. Zhang et al. assembled spherical microstructures by preparing 2D MOF nanosheets consisting of ultra-thin Ni/Co-2-methylimidazole (Ni/Co-MOF) nanosheets, which have a maximized surface area and the coupling effect of bimetallic ions, giving them high ORR catalytic activity [222]. Ni/Co-MOF nanosheets exhibit unique hollow nanocages assembled from overlapping nanosheets. In 0.1 M KOH, the onset potential on Ni/Co-MOFs nanosheets was 0.76 V (vs RHE). According to the K-L equation, in the potential range of 0.05–0.3 V, the

Table 3
Comparison of HER performance.

Electrocatalyst	Substrate	Mass loading (mg cm ⁻²)	Electrolyte	η_{10} (mV)	Stability (h)	Ref.
NiFe-MOF	NF	/	1.0 M KOH	68	20	[196]
NiFe(dobpdc)	NF	/	1.0 M KOH	113	30	[203]
NiFe-MOF-74	NF	/	1.0 M KOH	195	15	[22]
NiRu-MOF/NF	NF	2.1	1.0 M KOH	51	24	[194]
Ni ₃ S ₂ @2D Co-MOF/CP	CP ^f	/	1.0 M KOH	140	12	[29]
Ni-MOF@Pt	GCE	0.2	1.0 M KOH	102	/	[204]
NiCoP/NF	NF	/	1.0 M KOH	78	24	[205]
NiCoSe nanosheet	NF	3	1.0 M KOH	175	40	[206]
Ni-Co-S HPNA	CC	/	1.0 M KOH	110	12	[155]
Ni@CoO@Co-MOFC	NF	/	1.0 M KOH	138	/	[198]
Ru-Co ₃ O ₄ -NiO-NF	NF	/	1.0 M KOH	44	60	[197]
CoP/Co-MOF	CP	/	1.0 M KOH	26	20	[201]
FeS ₂ -MoS ₂ @CoS ₂ -MOF	NF	/	1.0 M KOH	92	30	[207]
CoS ₂ NS/CC	CC	3.5	1.0 M KOH	90	/	[208]
Co-BDC/MoS ₂	GCE	0.16	1.0 M KOH	248	15	[209]
Mn-CoP	GCE	0.5	1.0 M KOH	195	20	[210]
CoP/Co-MOF	CP	/	1.0 M PBS	106	20	[201]
CoP/Co-MOF	CP	/	0.5 M H ₂ SO ₄	52	20	[201]
Co-MOF-800	GCE	0.7	0.5 M H ₂ SO ₄	193	20	[211]
Co-Cl ₄ -MOF	GCE	0.28	0.5 M H ₂ SO ₄	424	/	[193]
AB&Co-Cl ₄ -MOF(3:4)	GCE	0.28	0.5 M H ₂ SO ₄	283	24	[193]
Co-Br ₄ -MOF	GCE	0.28	0.5 M H ₂ SO ₄	699	/	[193]
AB&Co-Br ₄ -MOF(2:4)	GCE	0.28	0.5 M H ₂ SO ₄	344	/	[193]
MoS ₂ /Co-MOF	GCE	/	0.5 M H ₂ SO ₄	262	6.9	[212]
(GO 8 wt%)Cu MOF	GCE	0.226	0.5 M H ₂ SO ₄	159	/	[65]
THTA-Co 2D MOF	GCE	/	0.5 M H ₂ SO ₄	283	4	[213]
MoS ₂ /Co-MOF-74	GCE	0.09	0.5 M H ₂ SO ₄	68	12	[214]
Mn-CoP	GCE	0.5	0.5 M H ₂ SO ₄	148	20	[210]
Co-PTC	CF ^g	2	0.5 M H ₂ SO ₄	227	40	[215]
MoS-CoS-Zn	GCE	/	0.5 M H ₂ SO ₄	72.6	60	[216]
CoP-NS/C	GCE	0.14	0.5 M H ₂ SO ₄	140	24	[217]
POM-based MOF	GCE	0.13	0.5 M H ₂ SO ₄	237	/	[218]
Ni-MOF@Pt	GCE	0.2	0.5 M H ₂ SO ₄	43	/	[204]

^f CP: carbon paper, ^g CF: Carbon film.

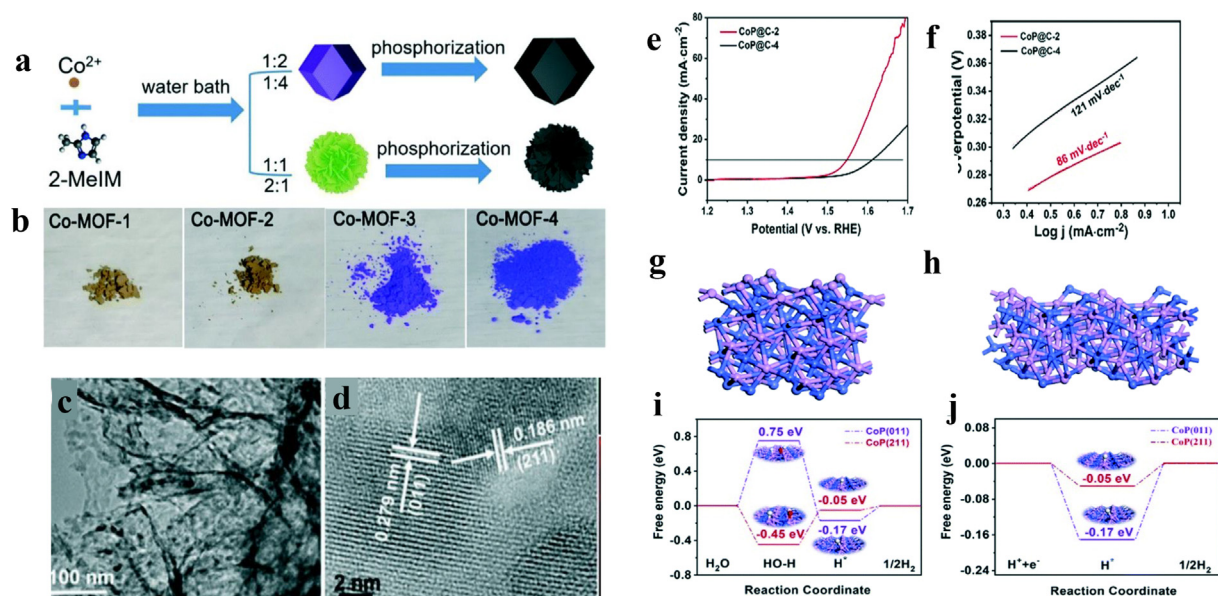


Fig. 23. (a) Composite diagram of CoP@C-Y. (b) Digital images in various scales. (c) TEM image and (d) HRTEM image of CoP@C-2. (e) LSV curve. (f) Tafel slope. (g) (011) aspects. (h) (211) aspects. (i) (011) and (211) HER free energy graphs under alkaline conditions. (j) HER free energy diagrams of (011) and (211) under acidic conditions. Reproduced with permission from ref. [202]. Copyright 2021, Royal Society of Chemistry.

number of transferred electrons in the O₂ reduction process was about 3.7, indicating that the main route of ORR on Ni/Co-MOFs nanosheets was the four-electron process. Choi et al. prepared bimetallic conductive 2D hexagonal MOF layer Co_xNi_y-HHTP

(HHTP = 2,3,6,7,10,11-hexahydroxytriphenylene) (Co_xNi_y-CATs) [223], and after optimization, bimetallic Co_{0.27}Ni_{0.73}-CAT not only exhibited a high diffusion-limited current density comparable to Co-CAT ($j = -5.68$ mA/cm²), but also had a high onset potential.

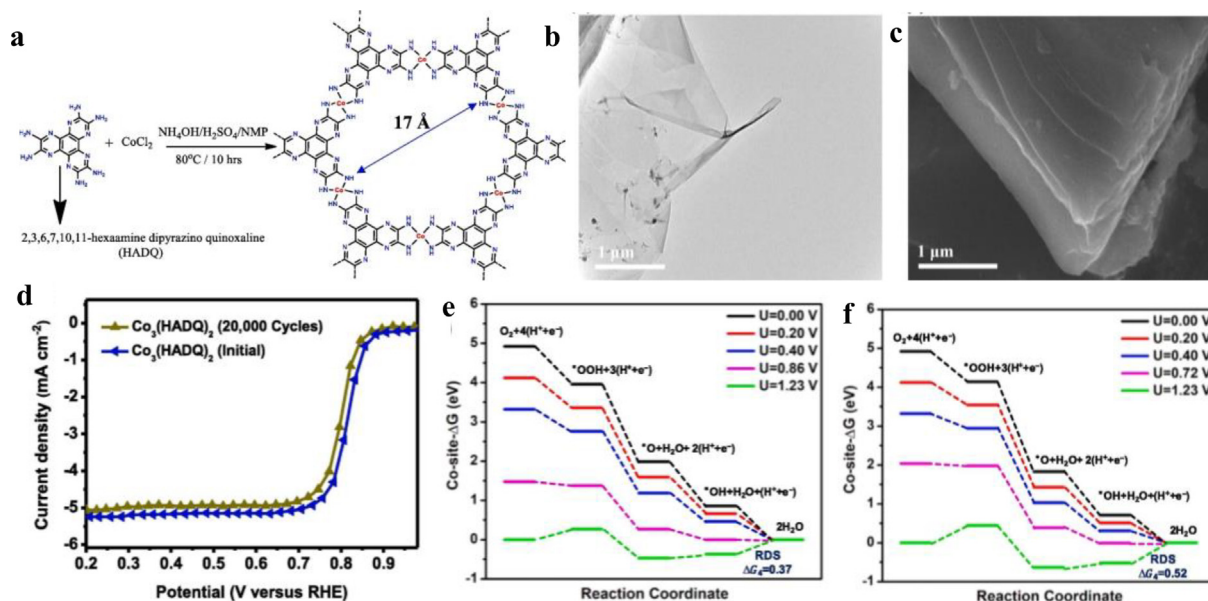


Fig. 24. (a) Synthesis route. (b) TEM. (c) SEM. (d) LSV before and after 20,000 CV cycles. The Free energy diagrams on (e) Co-site and (f) pyridinic N-sites. Reproduced with permission [221]. Copyright 2022, Elsevier Ltd.

Most 2D MOFs cannot be directly used for the ORR, because their conductivity is relatively poor, while they can catalyze the ORR by converting them into the corresponding derivatives.

4.3.2. 2D MOFs derived electrocatalysts for ORR

4.3.2.1. 2D MOFs-derived nanocomposites for ORR. Conditions such as annealing temperature need to be precisely controlled during pyrolysis to optimize morphology, structure and composition. Lei et al. prepared annealing (A-NCM) and regenerated (R-NCM) NiCo-based MOFs with 2D NiCo(2,6-naphthalenedicarboxylate tetrahydrate) (NCMs) as the precursors [224]. A-NCM showed thicker nanosheet stacks, while R-NCM exhibited denser nanosheets. R-NCM exhibited better ORR catalytic activity than NCM and A-NCM. Huang et al. synthesized binary NiFe-PTA (PTA = p-phthalic acid) nanosheets (MOF-NSs) by hydrothermal method, and then obtained their derivatives by pyrolysis strategy [225]. After NiFe-PTA NSs was annealed at 250°C for 1 h, NiO nanoparticles were uniformly dispersed on the surface of the MOF, and the basic MOF morphology was retained. When the pyrolysis temperature reached 300°C , massive highly crystallized nanoparticles appeared, and the MOF structure was partially decomposed. In 0.1 M KOH, NiFe-PTA NSs-300 had an onset potential of 0.75 V (vs RHE), and after 10,000 cycles, the selectivity of H_2O_2 was only 2 % lost. The generation of NiO nanoparticles and the partial decomposition of MOF structure generated more active sites and increased the selectivity of H_2O_2 . Studies have shown that single/paired non-noble metal atoms doped into carbon are one of the most promising ORR catalysts. Lu et al. prepared Zn/Fe-MOF@gC₃N₄ by doping massive single/paired Fe atoms and N with 2D bimetallic Zn/Fe-(1,4,5,8-naphthalenetetracarboxylic anhydride) as precursor, and then obtained Fe/N-PCNs by pyrolysis [226]. The derived Fe/N-PCNs maintained 2D morphology well, but the outer surface of the catalyst became more rough. During the pyrolysis process, gC₃N₄ decomposed to form Por-N₄, and the single Fe atoms were stabilized by Por-N₄ to form Fe-N₄ configuration, which can be used as active sites to catalyze ORR activity. According to the characterization, the doped Fe atoms were highly dispersed in the catalyst in the form of single atom or 2–4 clusters. The half-wave potential on the Fe/N-PCNs was 0.86 V (vs RHE) in 0.1 M KOH and 0.79 V (vs RHE) in 0.1 M KClO₄. The high

single/paired Fe atoms loading and high N content in the catalyst increased the density of active sites.

In transition metal- and N-codoped carbon materials, N, C and transition metals can interact in surface charge delocalization and charge redistribution. Wan et al. prepared Co/NCNTs/NSs by pyrolysis of the mixture of 2D Co/Zn-(2-methylimidazole) and N-doped carbon nanotubes (CNT) [227]. After heat treatment in H₂/Ar atmosphere, Co/NCNTs/NSs retained the 2D structural characteristics. According to the characterization, C=N bond can change the electronic structure of metal/C, providing more active sites for the ORR, and the charge redistribution caused by N doping is conducive to the adsorption of oxygen. In 0.1 M KOH, the onset potential on Co/NCNTs/NSs was 0.96 V (vs RHE), and its half-wave potential was 0.87 V (vs RHE). The encapsulation of 2D MOFs nanoparticles in carbon nanotubes can effectively prevent the oxidation and aggregation of transition metal nanoparticles. ZIF has large specific surface area and abundant pores, which can be transformed into amorphous or graphite carbon skeleton after pyrolysis [228]. Wang et al. encapsulated 2D Co/Zn-ZIF on nitrogen-doped carbon nanotubes by pyrolysis (Fig. 25a, b) [229]. Co–N–C is completely exposed on the surface of CNT (Fig. 25c, d), which can be used as active sites to improve the electrocatalytic performance. According to XPS spectra, nitrogen existed in the form of Co–N_x (399.0 eV) and graphitic N (401.3 eV) (Fig. 25e). In 0.1 M KOH, the onset potential on Co–N–CNTs was 0.97 V (vs RHE), and the E_{1/2} was 0.90 V, higher than Pt/C.

4.3.2.2. 2D MOFs derived single-atom materials for ORR. At present, single atom catalysts (SACs) have attracted much attention due to their maximum atomic utilization and unique properties. The order of intrinsic ORR activity of different active metals is Fe > Co > Cu > Mn > Ni. Cobalt-based SAC has excellent ORR activity. As an important branch of SACs, M–N–C electrocatalysts as a substitute for noble metal electrocatalysts have attracted wide attention, because M–N_x as active centers can effectively improve the electrocatalytic activity. Increasing the content of M–N_x can improve the electrochemical activity. Zhan et al. selected g-C₃N₄ as nitrogen source to prepare Co₃O₄@N/C composites with core-shell structure [138]. According to XPS, Co₃O₄@N/C had 3.43 % N content. The electronegativity of high N can change the electronic

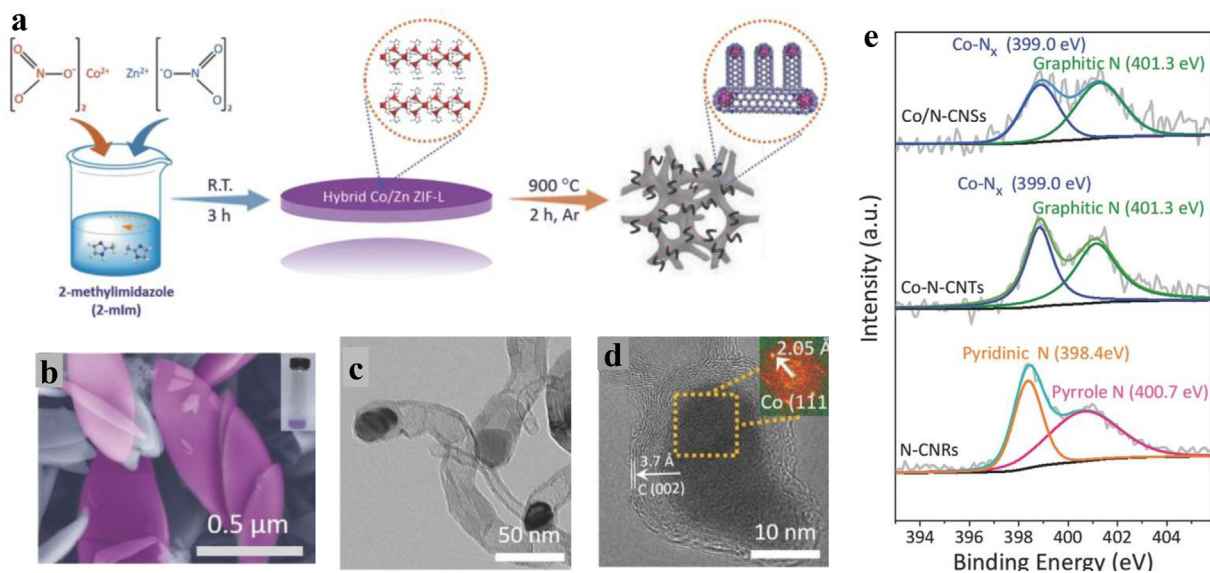


Fig. 25. (a) Illustration for the synthesis of Co/Zn-ZIF. (b) SEM image of Co/Zn-ZIF. (c) TEM and (d) HR-TEM of Co-N-CNTs. (e) N 1s XPS spectra. Reproduced with permission [229]. Copyright 2018, Wiley-VCH.

state of C and promote the adsorption of O. In addition, it can coordinate with metal to form active sites. The Co/N co-doping effect, the uniform dispersion of Co_3O_4 nanoparticles and the synergistic chemical coupling effect between N-doped carbon coatings with high graphitization and high N content are helpful to improve the catalytic activity of ORR. In 0.1 M KOH, the initial potential of $\text{Co}_3\text{O}_4\text{/N/C}$ was 0.90 V, and the half-wave potential was 0.80 V, which showed 13 % activity loss after 30000 s. In addition, the methanol poisoning test showed that $\text{Co}_3\text{O}_4\text{/N/C}$ was tolerant to methanol. Dong et al. synthesized high-quality ZIF-67 nanosheets with the help of salt template, which had uniform morphology and ultra-thin structure [117]. The directly carbonized porous carbon nanosheets had many accessible active centers and small diffusion barriers. Lu et al. prepared Cu-SAs/NSs (Cu SAs) by pyrolysis of 2D Cu/Zn-(BDC-NH₂)(C₃H₆N₆), which have many accessible Cu-N₄ active sites [230]. Under high temperature pyrolysis, the bimetallic Cu/Zn-(BDC-NH₂)(C₃H₆N₆) was transformed into N-doped porous carbon nanosheets, maintaining the original 2D morphology. The Zn species in the bimetallic Cu/Zn-(BDC-NH₂)(C₃H₆N₆) would evaporate during pyrolysis, and the Cu atoms would be fixed by the Cu-N bond. In 0.1 M KOH, its onset potential was 1.05 V (vs RHE) and the half-wave potential was 0.9 V (vs RHE) (Table 4). According to the K-L equation, the main pathway for ORR on Cu SAs was the four-electron process. In 0.1 M HClO₄, Cu SAs had an onset potential of 0.86 V (vs RHE) and a half-wave potential of 0.74 V (vs RHE), indicating excellent ORR performance under acidic conditions.

4.4. CO₂ reduction reaction

With the rapid development of industry and economy, the emission of carbon dioxide (CO₂) in the atmosphere gradually increases. The average concentration of carbon dioxide in the atmosphere in 2021 was ca. 415 ppm, far higher than the safe upper limit of 350 ppm. Hence, reducing the atmospheric CO₂ concentration is an urgent problem to be solved in scientific research [248]. In the process of reducing CO₂ concentration, on the one hand, low-carbon or non-carbon energy is used to replace fossil fuels to reduce CO₂ emissions. On the other hand, the main measures to capture, store and convert CO₂ in the air include thermochemistry, photochemistry [249], biochemistry and

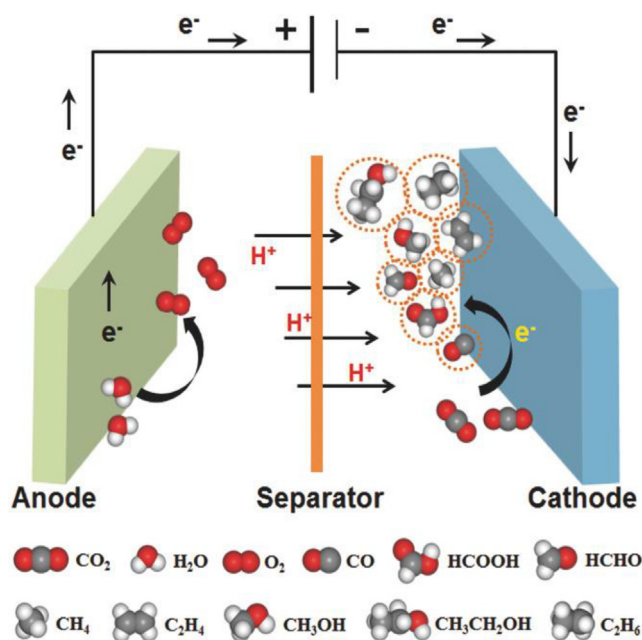
electrochemical catalytic conversion. The total electrocatalytic CO₂ reduction reaction can be divided into two semi-reactions, namely anodic OER and cathodic CO₂ reduction reaction (Fig. 26). Among them, CO₂ undergoes multi-electron and proton transfer at the cathode to generate different reaction intermediates or adsorbed products. At present, 16 products have been found, and it is difficult to obtain a single product. CO can be formed on Au-, Ag-, Pd- and Zn-based catalysts, while formic acid and other products can be generated on Sn, Bi and In-based catalysts. Cu is the only metal material reported at present that can effectively reduce CO₂ to multi-carbon products. Traditional electrocatalysts still have shortcomings such as slow reaction rate, poor selectivity and use in low-concentration CO₂ environment. The pores in MOF materials will produce spatial and electronic limits, which can improve the selectivity of products. In addition, MOFs have high affinity for CO₂, which are expected to achieve effective conversion at low CO₂ concentration. 2D MOFs have large surface area, which are beneficial to the adsorption and catalytic performance of CO₂RR.

4.4.1. CO as the reduction product

For CO₂ electroreduction to CO, the C in CO₂ is first combined with the active site of the catalyst, and *COOH intermediate is formed by proton and electron transfer. Then, *COOH intermediate is further transferred to form *CO intermediate. Finally, the obtained *CO intermediate is desorbed and CO is released from the active site of the catalyst. The *CO₂ intermediate generated in the CO₂RR process can be stably combined on the metal surfaces such as Au, Ag, Zn and Ni [37], and then coupled with *CO₂ through a proton to form a *COOH intermediate with strong binding ability to the metal surface. In addition, the *COOH intermediate is further transferred through single electron and single proton to form a *CO intermediate with weak binding to the catalyst surface, which makes CO easy to escape. Feng et al. synthesized bimetallic centered PcCu-O₈-Zn ((2D c-MOF)-O₈-Zn) with copper phthalocyanine as ligand and zinc bis (dihydroxy) complex [251]. PcCu-O₈-Zn MOF is composed of 2, 3, 9, 10, 16, 17, 23, 24-octahydroxyphthalocyanine copper monomer connected by square plane ZnO₄. The CO Faraday efficiency (FE_{CO}) of the electrocatalyst was as high as 88 %. The zinc bis (dihydroxy) complex in the catalyst was conducive to the conversion of CO₂ to CO, while CuN₄

Table 4
Comparison of ORR performance.

Electrocatalyst	Substrate	Mass loading (mg cm ⁻²)	Electrolyte	E _{onset} (V vs RHE)	E _{1/2} (V vs RHE)	Stability (h)	Ref.
Fe/N-PCNs	GCE	0.5	0.1 M KOH	0.96	0.85	5.5	[226]
Fe/Fe ₃ C@C	GCE	1.6	0.1 M KOH	0.93	0.83	/	[231]
Fe-ISAs/CN	GCE	/	0.1 M KOH	1.00	0.90	/	[232]
Fe ₃ C@N-CNT	GCE	/	0.1 M KOH	0.95	0.85	4.1	[233]
COP-TPP(Fe)@MOF-900	GCE	0.2	0.1 M KOH	0.99	0.846	/	[234]
FeNC-20-1000	GCE	0.76	0.1 M KOH	1.04	0.88	5.5	[235]
C ₃ N ₄ @NH ₂ -MIL-101	GCE	0.336	0.1 M KOH	0.99	0.84	4.4	[236]
Co/NCNTs/NSs	GCE	0.6	0.1 M KOH	0.96	0.87	/	[227]
Co ₃ O ₄ @N/C	GCE	1.28	0.1 M KOH	0.90	0.80	8.3	[138]
Co,N-C NP-800	GCE	/	0.1 M KOH	0.915	/	/	[237]
Co,N-C NS-800	GCE	/	0.1 M KOH	0.938	0.869	10	[237]
Co-N-C NS	GCE	0.646	0.1 M KOH	0.93	0.85	2.7	[238]
Co/NPC	GCE	0.49	0.1 M KOH	0.91	0.74	9.4	[239]
NiCo-NC	GCE	/	0.1 M KOH	/	0.81	8	[240]
BCN/ZrO ₂	GCE	0.141	0.1 M KOH	0.98	0.85	24	[241]
Co-NCS@CNT	GCE	0.17	0.1 M KOH	0.93	0.86	30	[242]
Co@N-C700	GCE	1	0.1 M KOH	/	0.78	28	[243]
Co@FLG	GCE	/	0.1 M KOH	/	0.841	24	[244]
Co _{0.6} -N/C-800	GCE	0.254	0.1 M KOH	0.916	0.825	/	[245]
Ni@N-HCGHF	GCE	/	0.1 M KOH	/	0.875	20	[246]
Cu ₃ HITP ₂ /CF	GCE	/	0.1 M KOH	/	0.75	24	[168]
PcCu-O ₈ -Co/CNTs	GCE	/	0.1 M KOH	/	0.83	/	[247]
Cu-SAs/NSs	GCE	0.25	0.1 M KOH	1.05	0.9	16.7	[230]
20 wt% Pt/C	GCE	0.125	0.1 M KOH	0.926	0.811	/	[245]

**Fig. 26.** Illustration of CO₂RR and the possible products. Reproduced with permission [250]. Copyright 2018, Wiley-VCH.

complex could promote the protonation process, and the bimetallic synergistic effect promoted CO₂RR. Metalloporphyrins have stable and adjustable structures and play a role in electron transfer and O₂ activation. In addition, they have catalytic activities in HER, OER, ORR and CO₂RR [219,252,253]. When metal porphyrins are combined with MOFs, metal porphyrins can be used as active sites [254,255], which not only inherits the advantages of MOFs, but also increases the number of active sites. Gu et al. anchored metalloporphyrin on 2D MOF nanosheets to prepare TCPP(Co)/Zr-BTB [256]. After adding TCPP (Co), the morphology of TCPP/Zr-BTB nanosheets is consistent with that of Zr-BTB. The TCPP/Zr-BTB nanosheets have smooth surface and ultra-thin thickness, resulting

in the curling of the edge of the nanosheets and the thickness of about one molecular layer (1.9 nm), which is conducive to reducing the mass transfer resistance and increasing the electron mobility. The FE_{CO} was 77.2 %. They also used the modified reagent to optimize it, and found that TCPP (Co)/Zr-BTB-PSABA (PSABA = p-sulfamido benzoic acid) had the best performance with FE_{CO} of 85.1 %. Metalloporphyrin and metalloporphyrin can generate electron transfer channels and enhance electron transfer ability. Because the path of CO generation is relatively simple, the FE_{CO} can reach 100 % at this stage, but the stability of catalysts is relatively poor.

4.4.2. CH₄ as the reduction product

The formation of CH₄ in the reaction also goes through two paths:



CO₂ is easily transformed into CH₄ in theory, because CH₄ has high theoretical reduction potential in thermodynamics. However, in fact, the selectivity of CH₄ is relatively low, which is mainly because the formation of CH₄ is a slow eight-electron transfer process. To improve the selectivity to CH₄, Cao et al. used a single type of copper-based MOF electrocatalyst, followed by the introduction of hydrogen bonds to stabilize specific intermediates to avoid the production of other products such as CO [257]. Cu-HHTP had a porous structure with micropore size of 1.23 nm and BET surface area of 184 cm³·g⁻¹. The Cu₂O@Cu-HHTP electrocatalyst showed FE (CH₄) of 73 %, and the current density of CH₄ as high as 10.8 mA·cm⁻² at -1.4 V. From FTIR spectra, the blue shift of *CO signal was related to the formation of hydrogen bonds. The key intermediates of CO₂ reduction to CH₄ such as *CHO, *CH₂O and *OCH₃ showed strong signal. According to DFT calculations, Cu₂O was the active center for the formation of CH₄. More importantly, the formation of hydrogen bonds made the adsorption of *CHO closer at the active site and reduced the energy barrier, and thereby hydrogen bonds could regulate the stability of the intermediates. Recent studies have identified a new class of 2D M₃(HITP)₂ MOF as electrocatalysts for CO₂RR (Fig. 27a, b). Chen et al. drew the energy distribution map of volcanic CO₂RR [258]. Taking Co₃(-HITP)₂ and Ni₃(HITP)₂ as examples, they combined transition metals with nitrogen atoms to form ligands and hybrid organic and inorganic compounds have excellent electrocatalytic properties for CO₂RR. DFT calculations showed that the final product selectivity of CO₂RR was determined by the coupling strength of O bond or C bond. Cr₃(HITP)₂ had lower overpotential (0.62 V) for CH₄ formation (Fig. 27c-f). In addition, Cr or Mn had high CO₂ reduction activity to CO and CH₃OH. When the metal was Cr, Mn, Fe and Os, the transformation of CO₂ to HCHO was more active.

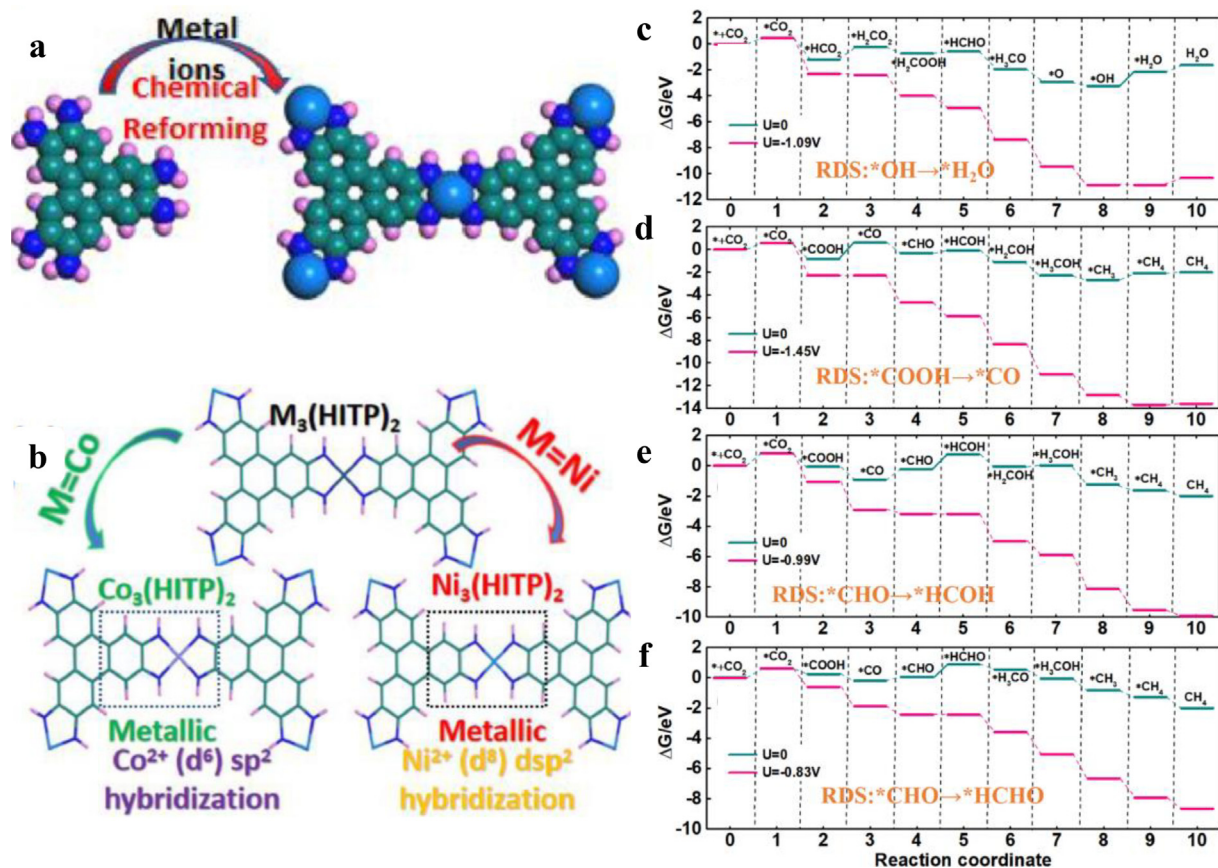


Fig. 27. (a) Composition diagram. (b) Illustration of 2D M₃(HITP)₂ geometry. (c) Gibbs free energy diagram for the reduction of CO₂ to CH₄ on Cr₃(HITP)₂, (d) Mn₃(HITP)₂, (e) Fe₃(HITP)₂ and (f) Co₃(HITP)₂. Reproduced with permission from ref. [258]. Copyright 2021, Elsevier Ltd.

The preparation of monoatomic catalysts by dispersing monoatomic metal ions onto appropriate carriers can not only improve the utilization of metal atoms, but also improve the selectivity. MS₄-based catalysts have high surface area and tunable pore structure. Yan et al. used DFT to study the M₃C₁₂S₁₂ (M = Fe, Co, Ni, Ru, Rh and Pd) monolayer [259]. M₃C₁₂S₁₂ possesses a planar structure, where M atom combines with four S atoms to form MS₄ unit (Fig. 28a). The limiting potential of CO₂ reduction to CH₄ was -0.74 V. The ΔG of COOH*/HCOO* formation on Ru₃C₁₂S₁₂ and Rh₃C₁₂S₁₂ was lower than 0.74 V. From Fig. 28b, the formation of COOH* was more stable than the formation of HCOO*. Through CO desorption and hydrogenation, the CO* hydrogenation energy (ΔG = 0.43 eV) on Rh₃C₁₂S₁₂ was lower than that of CO desorption (ΔG = 0.99 eV) (Fig. 28c, d). The CO₂ reduction pathway on Rh₃C₁₂S₁₂ was CO₂ (g) → COOH* → CO* → CHO* → CHOH* → CH₂OH* → CH₂* → CH₃* → CH₄ (g).

4.4.3. Methanol as the reduction product

From the perspective of the ORR process, the protonation of the key intermediate CH₃O* leads to the final formation of methanol. Recently, Ni₃(HITP)₂ was synthesized, which has high methanol resistance and redox properties. Yan et al. systematically explored a series of M₃(HITP)₂ (M = Fe, Co, Ni, Ru, Rh and Pd) for the CO₂RR [260]. Ru₃(HITP)₂ catalyzed the reduction of CO₂ to CH₄ and CH₃OH, while Fe₃(HITP)₂, Co₃(HITP)₂ and Rh₃(HITP)₂ catalyzed the reduction of CO₂ to CH₃OH (Fig. 29a), and their free energies were -0.50, -0.70 and -0.40 eV, respectively. The overpotentials on Co₃(HITP)₂ and Rh₃(HITP)₂ were 0.67 V and 0.46 V, respectively, which are more favorable for CO₂RR. The pathway of CH₃OH formation was CO₂ → COOH* → CO* → CHO* → OCH₂* → CH₂OH* → CH₃OH. However, the kinetic results showed that

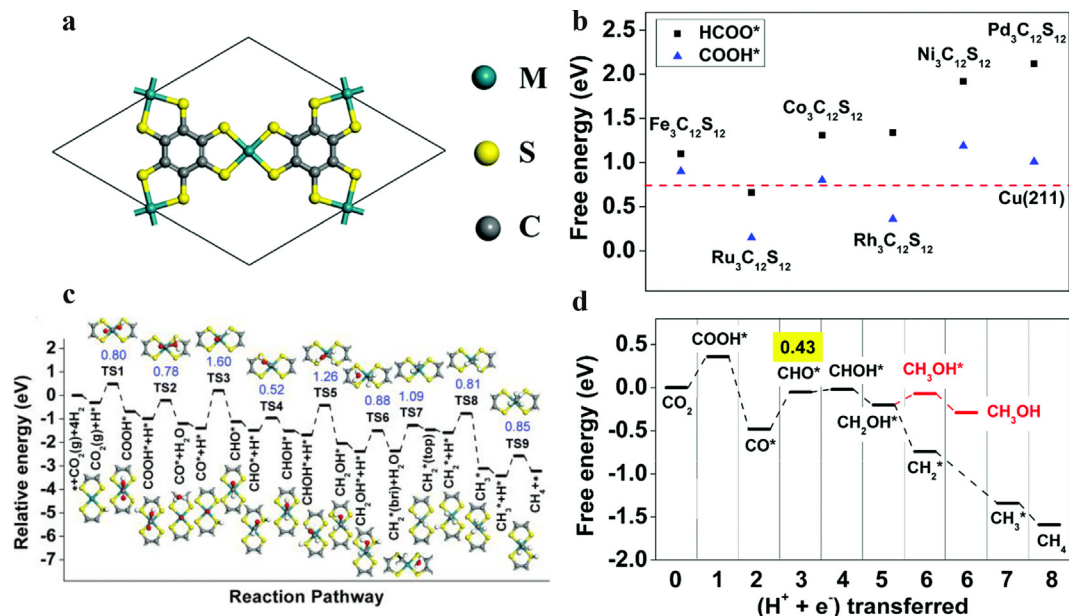


Fig. 28. (a) The configuration of $M_3C_{12}S_{12}$. (b) The free energies of $COOH^*$ and $HCOO^*$ formation. (c) Potential energy distribution of CO_2 reduction to CH_4 on $Rh_3C_{12}S_{12}$. (d) Free energy profiles for the CO_2RR on $Rh_3C_{12}S_{12}$. Reproduced with permission from ref. [259]. Copyright 2019, Royal Society of Chemistry.

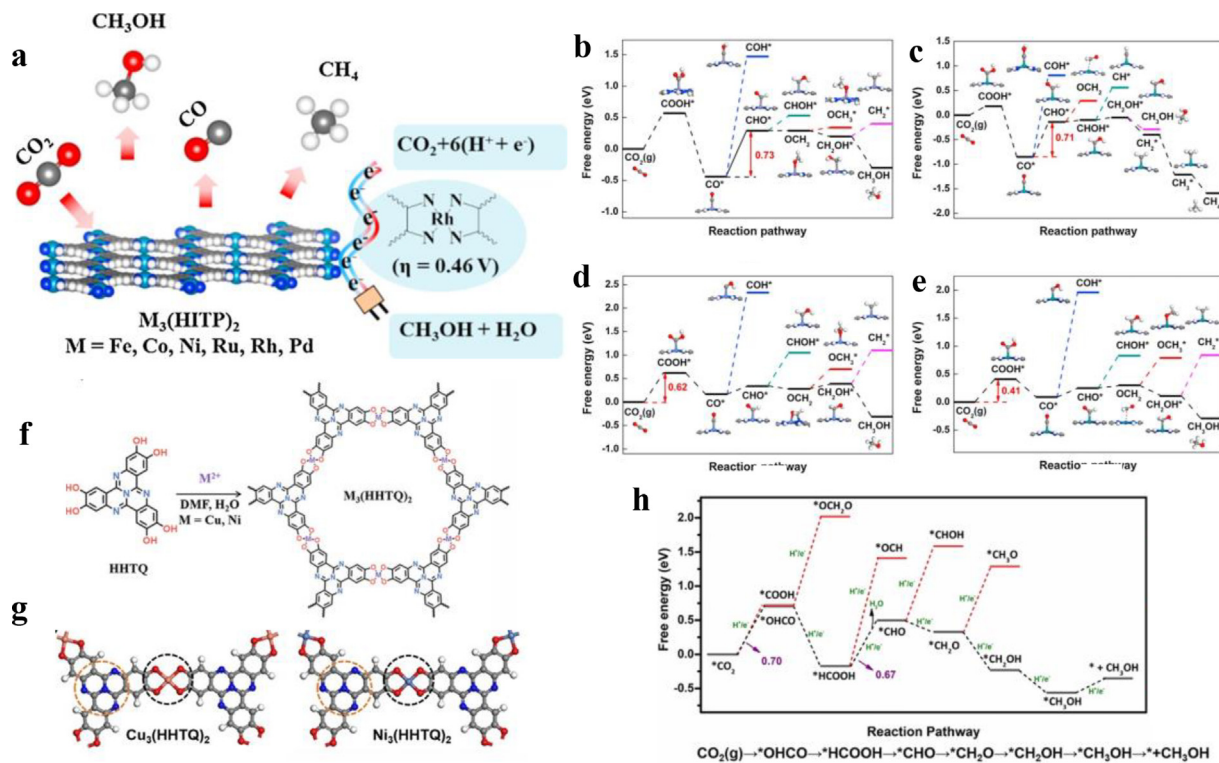


Fig. 29. (a) CO_2RR on $M_3(HITP)_2$. Free energy distribution of (b) $Fe_3(HITP)_2$, (c) $Ru_3(HITP)_2$, (d) $Co_3(HITP)_2$ and (e) $Rh_3(HITP)_2$ at zero potential. Reproduced with permission [260]. Copyright 2019, Elsevier Ltd. (f) Synthesis of $M_3(HHTQ)_2$. (g) Atomistic structure. (h) Free energy profiles on $Cu_3(HHTQ)_2$. Reproduced with permission [261]. Copyright 2021, Wiley-VCH.

$CO_2 \rightarrow COOH^* \rightarrow CO^* \rightarrow CHO^* \rightarrow CHOH^* \rightarrow CH_2OH^* \rightarrow CH_3OH$ was the more favorable for the formation of CH_3OH on $Co_3(HITP)_2$ (Fig. 29b-e). Chen et al. integrated nitrogen-rich and electron-deficient tricyclic quinazoline (TQ) into 2D MOFs to prepare $M_3(HHTQ)_2$ ($M = Cu$ or Ni) (HHTQ = 2,3,7,8,12,13-Hexahydroxytricycloquinazoline) (Fig. 29f, g) [261]. The content of metal ions was

up to 20 % in $M_3(HHTQ)_2$, and they were uniformly anchored in hexagonal lattice. Over $Cu_3(HHTQ)_2$, CH_3OH was the only product with FE of 53.6 %. DFT calculations showed that the $\Delta G(CO_2)$ on $Cu_3(HHTQ)_2$ was -0.24 V, and the adsorption capacity for CO_2 was stronger than $Ni_3(HHTQ)_2$ ($\Delta G = -0.19$ V). The calculation showed that the favorable reaction pathway of CO_2RR on

$\text{Cu}_3(\text{HHTQ})_2$ was $\text{CO}_2(\text{g}) \rightarrow * \text{OCHO} \rightarrow * \text{HCOOH} \rightarrow * \text{CHO} \rightarrow * \text{CH}_2\text{O} \rightarrow * \text{CH}_2\text{OH} \rightarrow * \text{CH}_3\text{OH} \rightarrow \text{CH}_3\text{OH}$ (Fig. 29h).

4.4.4. Formic acid as the reduction product

Among various reduction products of CO_2RR , formic acid is particularly attractive as an important raw material for chemical manufacturing and fuel cell applications. There are many reports on the use of various metal-based electrocatalysts such as Hg, Pd, Sn, Bi, Cu and Tl for the CO_2RR . However, Pb, Cd, Hg, and Tl have high toxicity, which hinders their large-scale application. Bi and Sn materials are often used to produce formate in CO_2RR . Sun et al. prepared 2D Bi-BTC (CAU-17) composed of ternary joints (H_3BTC) (Fig. 30a) [262]. Bi-BTC had a specific surface area of $316.8 \text{ m}^2/\text{g}$, single point total pore volume of $0.144 \text{ cm}^3/\text{g}$ and CO_2 adsorption capacity of $33.0 \text{ mg}/\text{g}_{\text{cat}}$. Bi-BTC was composed of randomly stacked nanosheets (Fig. 30b, c) with good crystallinity. In 0.1 M KHCO_3 , the conversion of CO_2 to HCOOH on the Bi-BTC electrode began at -0.6 V . When the potential reached -0.9 V , the FE of HCOOH reached a maximum value of about 92.2 % (Fig. 30d). The Tafel slope of Bi-BTC was $175.5 \text{ mV}/\text{dec}^{-1}$, which was lower than that of Bi_2O_3 ($250.4 \text{ mV}/\text{dec}^{-1}$) and Bi sheet ($186.3 \text{ mV}/\text{dec}^{-1}$) (Fig. 30e), indicating that the kinetics of CO_2RR on Bi-BTC was faster. After continuous working at -0.9 V for 10 h, the yield of HCOOH increased monotonically with the reaction time. According to DFT calculation, the formation energy of $* \text{HCOO}$ was 1.88 eV , and the formation energy of $* \text{H}$ was 2.27 eV (Fig. 30f, g). Therefore, HER is inhibited on the Bi-BTC. The main reasons for the high CO_2RR catalytic activity of Bi-BTC are as follows: (1) 2D structure with layered porosity and high exposed active sites favored the mass transfer rate; (2) The diameter of hexagonal, rectangular and triangular channels in Bi-BTC crystal structure is larger than that of CO_2 molecule; (3) Uniformly distributed Bi^{3+} can act as the active site of CO_2RR .

4.4.5. C_2+ as the reduction product

The reaction path of C_2+ production in CO_2RR is complex, and many intermediates cross each other. CO_2 is transferred through proton and electron transfer to form $* \text{CO}$ intermediate, and the generated $* \text{CO}$ is added H on O to form $* \text{COH}$. The obtained $* \text{COH}$ is coupled with $* \text{CO}$ to form $* \text{COCO}$, and further hydrogenated to form $* \text{COHCH}_2$. $* \text{COHCH}_2$ is an important intermediate, which will generate a variety of C_2 products. (1) C_2H_4 is generated from the cleavage of the carbon-oxygen bond [263]. (2) $\text{C}_2\text{H}_5\text{OH}$ is generated after further proton and electron transfer [264]. (3) C_2H_6 is generated after further proton and electron transfer and dehydrogenation [265,266]. (4) If the product obtained by further coupling with $* \text{CO}$ through proton and electron transfer, $\text{C}_3\text{H}_7\text{OH}$ can be generated [267]. There is one path to generate C_2H_6 , namely the intermediate of $* \text{CH}_3$ will generate C_2H_6 ($* \text{CH}_3 + * \text{CH}_3 \rightarrow \text{C}_2\text{H}_6$) through C-C coupling.

Copper is the only known metal that selectively converts CO_2 into hydrocarbons and alcohols. The local field around copper plays an important role in CO_2RR . Alcohols can be formed on binuclear Cu-Cu. Wei et al. synthesized a series of MOF-derived Cu NPS NC catalysts at different temperatures and studied the effect of N doping on CO_2RR . [71] The experimental results showed that Cu-NC400 was beneficial to the formation of C_2+ , on which FE(ethanol) was 18.4 % and FE(formate) was 7.2 %. The products on the undoped Cu-C samples were mainly CO , CH_4 and C_2H_4 , and the total FE value was only 15 %. Sargent et al. adjusted the surface structure of copper clusters by changing the position of copper in MOF [268]. They changed the impeller structure of copper dimer in $\text{Cu}_3(\text{btc})_2 \cdot x\text{H}_2\text{O}$ ($\text{C}_{18}\text{H}_6\text{Cu}_3\text{O}_{12}$, HKUST-1) MOF, separated the carboxylic acid part and calcined them. Before calcination, the FE(C_2H_4) in the CO_2RR on HKUST-1 MOF was 10 %, and the liquid product contains ethanol. However, after calcination at $250 \text{ }^\circ\text{C}$ for 3 h, the FE(C_2H_4) increased to 45 % (Table 5) and the FE(CH_4) was suppressed below

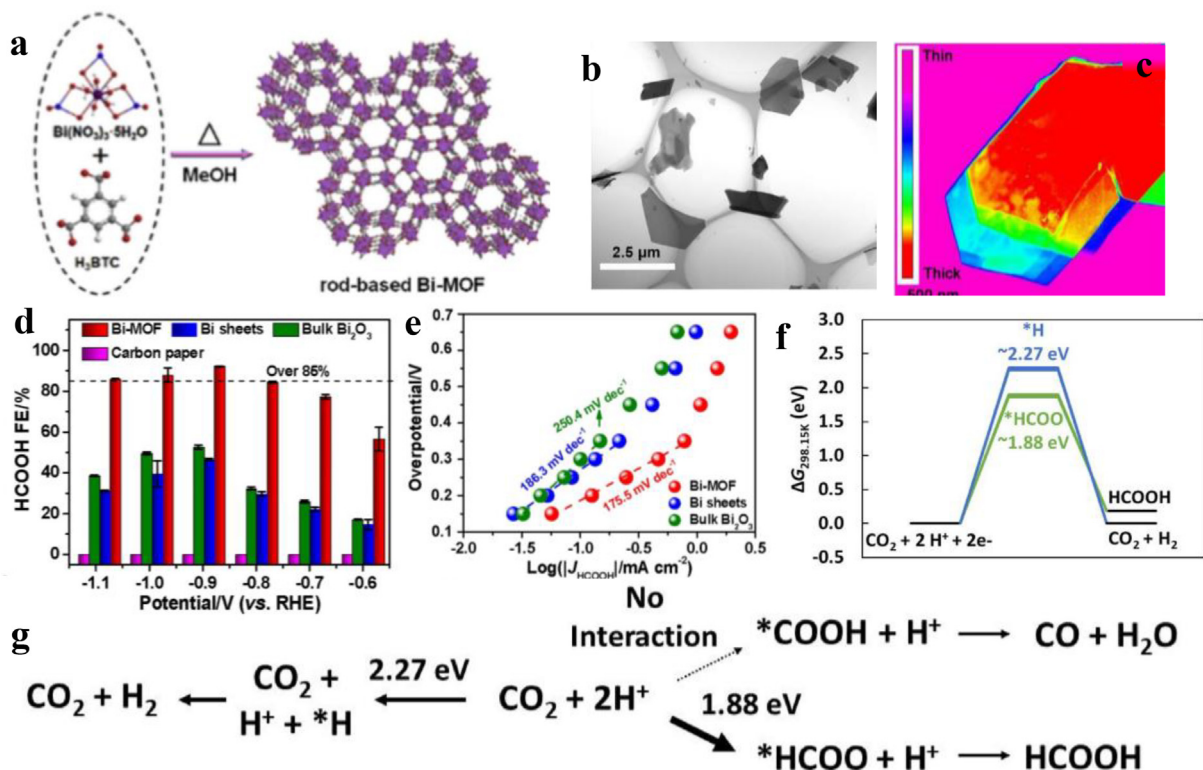


Fig. 30. (a) Schematic depiction of Bi-MOF. (b) TEM image. (c) Transformed TEM image. (d) HCOOH FEs. (e) Tafel plots. (f) Free energy diagram. (g) Suggested reaction pathway. Reproduced with permission [262]. Copyright 2020, Elsevier Ltd.

Table 5
Comparison of CO₂RR performance.

Electrocatalyst	Substrate	Mass loading (mg cm ⁻²)	Electrolyte	Current density (mA·cm ⁻²)	Product	FE (%)	Stability (h)	Ref.
NiNPIC	CP	0.09	0.5 M KHCO ₃	10.2	CO	95.1	24	[269]
Ni(Im) ₂ -5 nm	CFP	1	0.5 M KHCO ₃	7.0	CO	78.8	14	[36]
NiPc-NiO ₄	CP	/	0.5 M KHCO ₃	34.5	CO	98.4	10	[270]
MOF-525 film	FTO	/	1 M TBAPF ₆	2.3	CO	100	5	[271]
PPy@MOF-545-Co	CP	1	0.1 M KHCO ₃	13	CO	98	10	[272]
CoCp ₂ @MOF-545-Co	CPE	1	0.5 M KHCO ₃	56.2	CO	97	/	[273]
PCN-222(Fe)/C	CP	3	0.5 M KHCO ₃	1.2	CO	91	10	[274]
PCN-223-AA	CP	0.5	0.5 M KHCO ₃	8.8	CO	90.7	20	[275]
PCN-223-FA	CP	0.5	0.5 M KHCO ₃	3.8	CO	81	/	[275]
PCN-223-FA	CP	0.5	0.5 M KHCO ₃	3.8	CO	76.8	/	[275]
PcCu-O ₈ -Zn	CP	/	0.1 M KHCO ₃	/	CO	88	/	[251]
Al ₂ (OH) ₂ TCPP-Co	CDE ^h	/	0.5 M KHCO ₃	5.9	CO	/	7	[276]
Re-SURMOF thin film	FTO	/	0.1 M TBAH	2.5	CO	93 ± 5	/	[277]
Zn-MOF/CP	CP	/	BmimOTf	2.1 ± 0.3	CO	4.6 ± 1.2	/	[278]
In ₂ O ₃ @In-Co PBA	CP	1.7	0.1 M KHCO ₃	31.5	HCOO ⁻	85	5	[279]
Zn-MOF/CP	CP	/	BmimOTf	2.1 ± 0.3	CH ₄	85.4 ± 3.2	/	[278]
HKUST-1 MOF	GDL ⁱ	0.56	1.0 M KOH	/	C ₂ H ₄	45	10	[268]
Cu/Cu ₂ O@NG	CP	1.1	0.2 M KI	19.0	C ₂ -C ₃	56	1.25	[69]

^h CDE: carbon disk electrodes, ⁱ GDL: gas diffusion layer.

1 %, mainly because the undermatching in copper clusters increased the formation of C₂H₄.

4.5. Nitrogen reduction reaction

As an environmentally friendly energy carrier, NH₃ is widely used in industrial and agricultural production, such as ammonia, dyes, plastics, explosives, agricultural and fertilizers. More than 200 million tons of ammonia are produced annually worldwide, 80 % of which is used for synthetic fertilizers, making an important contribution to rapid economic development and rapid population growth. There are three ways to synthesize ammonia: biological nitrogen fixation, Haber Bosch process and (photo)electrocatalysis. Compared with photocatalytic reduction method, electrochemical nitrogen reduction reaction (NRR) is more effective. In the electrocatalytic reduction process, renewable solar and wind energy are used to drive the fixed potential to produce the required products. NRR is a typical heterogeneous catalysis, which mainly includes three basic steps: N₂ adsorption and activation, protonation hydrogenation and NH₃ molecule separation. N₂ is an inert diatomic molecule with high strength N≡N, and only large energy input can make the triple bond break. In addition, the reaction enthalpy of N₂ molecule with one hydrogen proton to generate N₂H is as high as 37.6 kJ·mol⁻¹. During the NRR, HER is the main side reaction, and most electrons and protons tend to generate H₂ rather than NH₃. Hence, it is necessary to improve the catalytic activity and selectivity of NRR, and the key is to develop new and efficient electrocatalytic materials. Compared with bulk MOFs, 2D MOFs have higher specific surface area, more vacancy defects and more bare edge positions, which are beneficial for the adsorption and activation of N₂ molecules.

4.5.1. 2D MOFs for NRR

Compared with noble metal materials, non-noble metal materials have higher crustal content, and thereby they have greater application prospects as attractive NRR catalysts. Biological nitrogenases containing Mo, Fe and V are involved in natural N₂ fixation and a variety of NRR electrocatalysts made from these metals have been developed for the artificial electrochemical synthesis of NH₃ under environmental conditions Li et al. synthesized Co₃Fe-NH₂-BDC nanosheets, which can meet the requirements of both OER and NRR [166]. Co₃Fe-NH₂-BDC showed a uniform nanosheet morphology of about 10 nm, where Co, Fe, C, N and O elements are

highly evenly distributed. According to XPS analysis, partial charge was transferred from Fe to Co, indicating that the bimetallic synergistic effect of Co and Fe optimized the filling of e_g orbit. For the OER, the η₁₀ on the Co₃Fe-NH₂-BDC was 280 mV, which was lower than that on commercial ruthenium dioxide. For NRR, the Faraday efficiency was 25.64 % and the NH₃ yield was 8.79 μg·h⁻¹·mg⁻¹_{cat}. The high OER and NRR activity of Co₃Fe-NH₂-BDC could be attributed to the coupling between Co and Fe.

Sun et al. calculated the NRR activity of TM₃(HAB)₂ (TM: transition metal) prepared by reacting transition metal and hexaaminobenzene (HAB) [280]. The active site of TM₃(HAB)₂ was TM-N₄, and each TM atom combined with the surrounding four N atoms to form a square planar structure. After screening different transition metals, the total spin moment of Mo-based MOF was 2.19 MB, which was the highest ranked transition metal atom. Dai et al. found highly stable and reusable metal-based catalysts [281]. They reacted benzene hexathiol (BHT) with transition metal to form nitrogen-free MOF, which was called TM-BHT. TM-BHT showed planar network structure and high density TMS₄ as the active center of NRR (Fig. 31a-c). There was a bidirectional charge transfer between TM atoms and N₂ atoms (Fig. 31d). In monoatomic catalysts, metal atoms are prone to aggregation and the active center is unstable. As a new monoatomic catalyst, TM-BHT not only has high density of active center, but also has encouraging stability. After screening different transition metals, only Sc-BHT and Mo-BHT could be used as effective NRR catalysts (Fig. 31e-g), and their NH₃ desorption energies were 0.62 and 0.96 eV, respectively (Fig. 31h, i). At the same time, high temperature and high pressure could accelerate the desorption of NH₃ (Fig. 31j).

4.5.2. 2D MOFs derived electrocatalysts for NRR

In addition to the overwhelming competition of HER, high temperature and high pressure are required for nitrogen reduction reactions. The combination of NRR electrocatalysts and MOFs can improve the catalytic selectivity of NRR. Li et al. deposited MOFs thin films (ZIF) on Ag-Au nanoparticles [282]. ZIF was superhydrophobic, which can inhibit water molecules from entering the surface of Ag-Au catalyst, thereby inhibiting HER. The encapsulation of ZIF increased the FE of NH₃ by 10 %. This is an effective solution to inhibit HER in the NRR.

π-conjugated metal bis(dithiene) complexes (MC₄S₄) do not contain any N coordination, and thereby the ammonia produced only comes from the molecular dinitrogen. Liu et al. systematically

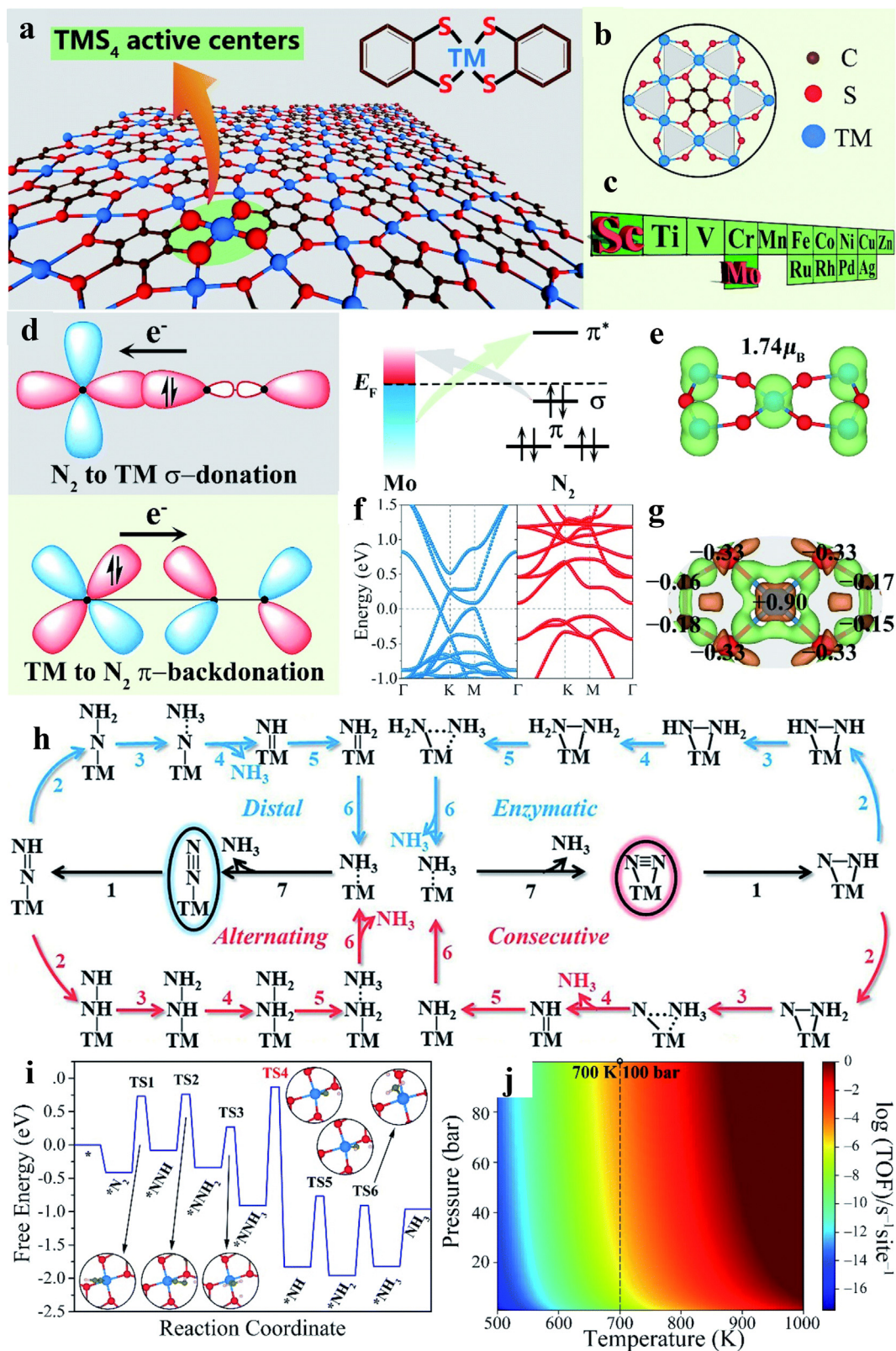


Fig. 31. (a) Structure of TMS_4 . (b) The perfect Kagome lattice. (c) The active TM. (d) Bidirectional charge transfer. The Mo-BHT of (e) band structure, (f) spin-resolved density, (g) charge density difference. (h) Schematic depiction of four pathways for N_2 reduction to NH_3 . (i) Minimum energy path. (j) TOF at various temperature and pressures. Reproduced with permission from ref. [281]. Copyright 2020, Royal Society of Chemistry.

studied the reduction of nitrogen on a series of MOF-derived MC_4S_4 (M stands for Fe, Co, Ni, Cu, Ru, Rh, Pd, Pt, Os, and Ag) nanosheets under acidic conditions [74]. Iron, osmium, iridium and ruthenium

could strongly interact with N_2 molecules. Metals anchored on the nanosheets had weak interaction with nitrogen molecules, and thus they could not be used as electrocatalysts for NRR, because

the ΔE_{N_2} was less than 0.50 eV. Then, $\Delta G_{N_2-N_2H}$ was calculated, and it was found that only OsC_4S_4 nanosheets could be used as electrocatalysts for the NRR. Nitrogen could be fully activated on the OsC_4S_4 nanosheets. It provided a prediction method for the development of new NRR electrocatalysts.

Transition metal carbides have similar electronic structure to noble metals, and d orbital provides an opportunity for adsorbate to enhance its adsorption capacity. Thus, transition metal carbides can replace noble metal electrocatalysts. Yang et al. prepared a periodic carbon vacancy NRR electrocatalyst with a vanadium carbide mesoporous structure that facilitates the conversion of N_2 to NH_3 [283]. They used vanadium pentoxide nanosheets to induce MOF growth and then formed vanadium carbide through carbothermal reaction. The electrocatalyst had a high $FE(NH_3)$ of up to 18.3 % at an overpotential of 0.1 V. NRR electrocatalysts with periodic carbon vacancies had higher electrocatalytic activity. Transition metal oxide (TMO) has high NRR catalytic activity in acidic and neutral media, but low activity in alkaline media due to difficult adsorption of protons. However, HER can be inhibited in alkaline medium. Luo et al. prepared hollow $C@NiO@Ni$ electrocatalysts using nickel-based MOF (Ni-BTC) [284]. $C@NiO@Ni$ showed NH_3 yield of $43.15 \mu g \cdot h^{-1} \cdot mg_{cat}^{-1}$. The NiO/Ni interface facilitated proton adsorption, which makes it easier to capture protons in alkaline media.

5. Strategies for optimizing the electrocatalytic performance of 2D MOFs and their derivatives

With high specific surface area, high porosity, ultra-thin structure and abundant active centers, 2D MOFs are expected to replace precious metals as electrocatalysts. However, 2D MOFs also have the disadvantage of low charge transfer rate, which requires fine-tuning the size of the pores, improving the defects and regulating the electronic structure. According to the scale of various regulation strategies, they can be divided into nanoscale pore structure regulation, sub-nanometer defect regulation and electronic scale electronic regulation.

5.1. Regulating pore structure

Most of the intrinsic pores in the crystal structure of 2D MOFs are micropores, and the reactants can be transmitted through the micropores. However, the mass transfer rate of the reactants will be restricted due to the small pore size. The addition of mesopores and macropores to 2D MOFs can increase the mass transfer rate. The construction of mesopores, macropores and even multi-level channels in 2D MOFs has become the most common strategy in pore structure regulation. Foamed MOFs can be rapidly synthesized under a certain condition to construct a loose and porous structure. In the case of unstable MOFs with low crystallinity, they are further treated to dissolve the unstable parts to form mesopores.

5.2. Defect engineering

The defect regulation of 2D MOFs mainly involves the regulation of point defects formed by metal nodes or organic ligand vacancies, and the formation of such defects favors the exposure of more coordination unsaturated sites, so that the electrocatalytic apparent activity can be improved to a certain extent. The defect regulation is closely related to the regulation of pore and electron structures. In the process of regulating defects, many new channels will be generated, so that the reaction mass transfer rate is faster. The change of pore structure caused by defect regulation can achieve the same effect as the regulation of pore structure. For

example, the ligand vacancy defect formed by the regulator can lead to the formation of multi-level pore structure in 2D MOFs, thus improving the reaction activity. In addition, the defects have a significant influence on the electronic structure of 2D MOFs. The point defects will cause periodic crystal defects in the local range, thus changing the electronic structure and electronic filling mode of the material. For example, the introduction of other substances will cause ligand vacancies and ligand deletion, which is helpful to form a new electronic state and improve the charge transfer performance.

5.3. Regulating electronic structure

The intrinsic activity of the electrocatalyst depends on the adsorption strength of reaction intermediates on the active site and the energy of the transition state, and the electronic structure of the active site directly determines such properties. Hence, the direct purpose of electronic regulation of 2D MOFs is to improve their intrinsic activity. In addition, in the process of charge transfer, the electronic structure plays an influential role. Through element doping and constructing heterogeneous interfaces, the energy of the adsorption and transition states can be effectively adjusted, and the intrinsic activity of the active site can be improved. In addition, the electronic structure can also be regulated by constructing planar conjugate structures, forming conductive composite materials and doping guest molecules to enhance the conductivity of 2D MOFs, of which the application of the plane conjugate structure is particularly extensive.

6. Summary and prospect

In this review, the preparation methods, strategies for tuning electrocatalytic performance and electrocatalytic applications of 2D MOFs and their derivatives are systematically reviewed. The preparation methods of 2D MOFs included the top-down and bottom-up synthesis, whose advantages and disadvantages were analyzed in depth. In terms of the preparation methods of 2D MOF derivatives, we focused on some typical synthesis methods, such as pyrolysis method and calcination method, and discussed the principles and effects. In addition, multi-scale pore regulation strategies, defect regulation and electronic regulation were discussed. Finally, the applications of 2D MOFs and their derivatives in electrochemical HER, OER, ORR, CO_2RR , and NRR were discussed.

At present, 2D MOFs and their derivatives are widely studied for the OER. For 2D MOFs, researchers purposefully adjusted the electronic structure of metal nodes by selecting appropriate organic ligands to obtain highly oxidized metal cations that can promote the oxidation reaction. In addition, 2D MOF nanosheets were grown on conductive substrates (nickel foam, carbon cloth, carbon fiber paper, etc.) to achieve rapid charge transfer. For 2D MOF derivatives, (1) Fe, Co and Ni are common active centers in alkaline OER catalysts. Nickel-based OER catalysts (including hydroxides, oxides, sulfides and phosphates) showed excellent OER catalytic activity in alkaline media. (2) Bimetallic or heterojunction catalysts have a modulated electronic structure or built-in electric field generated by the charge or atomic interface, which is more effective than single metal catalysts. Hence, the incorporation of iron into nickel-based compounds will further improve the electrocatalytic performance. (3) S has high electronegativity and can be used to modulate the electronic structure of metal sites. Therefore, 2D MOFs derived transition metal sulfides can promote the catalytic activity of OER [285]. Compared with OER, there are less reports on 2D MOFs for HER. Among them, 2D transition metal-based (Fe, Co and Ni) MOFs can be used as substitutes for noble metal catalysts for the HER. Co-based materials are widely used in HER due

to their high fixation and excellent electronic configuration [193]. For 2D MOFs, the catalytic activity of HER can be improved by changing the types of active metal centers, adjusting the electronic structure of metal sites and increasing the electron density. Furthermore, bimetallic and polymetallic MOF derivatives exhibit excellent HER catalytic performance due to the coupling effect. Among 2D MOF derivatives, metal disulfides are widely considered as the most effective HER catalysts [29,286]. For the ORR, porous graphene has abundant nanopores, generating abundant edge defects as the active sites. Therefore, the formation of nanonets using 2D MOFs as precursors can improve the ORR activity. In addition, the atoms in the single/paired non-noble metal M–N–C doped into carbon are highly dispersed, and the atomic utilization rate can be as high as 100 %, which are the most promising ORR materials to replace Pt-based catalysts [287]. The dominant M–N coordination is beneficial to ORR. 2D MOFs have porous structure and adjustable chemical compositions, which are ideal precursors for preparing single-atom M–N–C catalysts. CO₂RR is carried out through proton-coupled multi-electron transfer, which can be divided into multiple steps. Therefore, the products produced by different intermediates are also diverse, and the high selectivity of specific products is a key evaluation factor. Co porphyrins have high selectivity for CO production, Cu-based MOF nanosheets can directly convert CO₂ into hydrocarbons or alcohols, and Cu–N–C materials have high selectivity to C₂H₄. 2D M₃(HHTQ)₂ derived single-atom catalysts show high activity for CO₂RR, and when Cu₃(HHTQ)₂ catalyzes CO₂RR, CH₃OH is the only product [261]. Up to now, there are few studies on NRR-based 2D MOFs, but 2D MOFs with transition metals Cu, Co, Ni and Mo are promising to replace noble metal catalysts. In these materials, transition metals coordinate with four N atoms to form TMN₄ configuration, and the catalytic performance is similarly to that of noble metals [54]. In addition, SACs containing the VII metal (Cr, Mo and W) derived from 2D MOFs has high NRR catalytic activity [288–290].

MOFs usually exist in the form of 3D network structure, and the metal ion centers have large coordination numbers. Therefore, organic ligands with poor conductivity lead to low conductivity of most MOFs (10⁻¹⁰ S·m⁻¹) [280]. The tortuous channels in 3D MOFs hinder the exposure of active sites and reduce the contact probability between active centers and reactants, resulting in low catalytic activity. In addition, the 3D bulk structure makes massive active sites buried inside, and the mass transfer capacity of the catalyst is insufficient. The formation of ultra-thin 2D structure with high specific surface area and porosity is an attractive strategy. Compared with 3D MOFs, 2D MOFs nanosheets have larger transverse size, larger specific surface area and abundant surface unsaturated metal active sites, which are beneficial to the adsorption of reactants, the exposure of active sites and the acceleration of mass transfer in the reaction process. In addition, the formation of carbon layers in 2D MOF derivatives not only improves the conductivity, but also effectively slows down the corrosion of metal nanoparticles in the electrolyte and improves the stability. 2D MOF-derived materials can retain the 2D structure of 2D MOFs, but the surface and bulk compositions change. Compared with 3D bulk MOF derivatives, 2D MOF derivatives show more advantages, such as large specific surface area and porous structure, ultra-thin nanosheet structure accelerating electron transfer and more exposed active sites, which play an important role in improving the catalytic activity.

Although 2D MOFs have made great progress in the field of electrocatalysis, there are still many difficulties to be overcome:

(1) Each synthesis method has its drawbacks and limitations. The top-down method is relatively simple to operate and the applicability is widespread, but the repeatability is poor, and it often causes certain losses to 2D MOFs in the process of stripping. Moreover, it is difficult to control the thickness and size of 2D MOFs.

Although the bottom-up method achieves controllability through experimental optimization, it is complex, expensive and inefficient due to the complexity of the operation. Therefore, the development of a simple operation method to synthesize 2D MOFs with high yield and low cost is highly desirable.

(2) Although there are many MOFs, the commonly used 2D MOFs are still some ZIF, PBA and MIL series, which limit the improvement of the structure and catalytic properties of such materials. In the future, the compositions of 2D MOFs and derived materials are still needed to be enriched.

(3) Compared with bulk MOFs, the small thickness of 2D MOFs can shorten the electron/ion transmission distance, but the conductivity of 2D MOFs is still worse than graphene, and in the future electrochemical field, how to improve the conductivity of 2D MOFs and their derivatives is an important research topic. Optimizing the carbon defect structure and increasing the degree of graphitization in 2D MOF-derived carbon-based materials can improve the conductivity. In addition, supporting 2D MOFs on substrates with good electrical conductivity can improve the conductivity and catalytic activity.

(4) So far, 2D MOFs and their derived materials have poor stability and are prone to deactivate in electrocatalytic processes. From a practical point of view, it is more attractive to design durable catalysts that can be adapted to a variety of environments. It may be considered to wrap a protective film on the surface of 2D MOFs and their derivatives to improve their stability.

(5) In current studies, researchers rely too much on the adsorption results on the surface of the 'model' defined by DFT calculations, but DFT itself has some uncertainties related to functional selection. To avoid such problems, the surface should be strictly characterized to ensure that the electrode surface will not be reconstructed and remains in a hypothetical state during electrolysis.

In conclusion, 2D MOFs and their derivatives have the advantages of large surface area, high porosity and controllable structure, which show excellent performance in the field of electrocatalysis. However, the above progress is still limited to the laboratory research stage. Researchers need to carry out further research to find 2D MOFs and their derivatives with low cost, high preparation efficiency and good durability to promote practical applications.

Declaration of Competing Interest

The authors declare that they have no known competing financial interests or personal relationships that could have appeared to influence the work reported in this paper.

Acknowledgments

This work was supported by the National Natural Science Foundation of China (22075099) and the Education Department of Jilin Province (JJKH20220967KJ, JJKH20220968CY).

Appendix A. Supplementary data

Supplementary data to this article can be found online at <https://doi.org/10.1016/j.ccr.2022.214777>.

References

- [1] Y.C. He, L.Y. Xiao, Z.H. Yuan, J. Zhang, Y. Wang, N. Xu, Two coordination polymers constructed by 5-[(4-carboxyphenoxy)methyl]benzene-1,3-dicarboxylic acid and 2,2'-bipyridine: syntheses, structures and luminescence properties, *Acta Crystallogr. C Struct. Chem.* 75 (2019) 1562–1568.

- [2] N. Wang, A. Mundstock, Y. Liu, A. Huang, J. Caro, Amine-modified Mg-MOF-74/CPO-27-Mg membrane with enhanced H₂/CO₂ separation, *Chem. Eng. Sci.* 124 (2015) 27–36.
- [3] G. Xu, Z. Meng, Y. Liu, X. Guo, K. Deng, L. Ding, R. Lu, Porous MOF-205 with multiple modifications for efficiently storing hydrogen and methane as well as separating carbon dioxide from hydrogen and methane, *Int. J. Energy Res.* 43 (2019) 7517–7528.
- [4] J.R. Fu, T. Ben, S.L. Qiu, Fabrication of polymer-supported metal organic framework membrane and its gas separation performance, *Wuli Huaxue Xuebao* 36 (2020) 1901079.
- [5] K. Rui, G. Zhao, Y. Chen, Y. Lin, Q. Zhou, J. Chen, J. Zhu, W. Sun, W. Huang, S.X. Dou, Hybrid 2D dual-metal-organic frameworks for enhanced water oxidation catalysis, *Adv. Funct. Mater.* 28 (2018) 1801554.
- [6] X. Zhang, L. Chang, Z. Yang, Y. Shi, C. Long, J. Han, B. Zhang, X. Qiu, G. Li, Z. Tang, Facile synthesis of ultrathin metal-organic framework nanosheets for Lewis acid catalysis, *Nano Res.* 12 (2019) 437–440.
- [7] Z.Q. Gao, C.Y. Wang, J.J. Li, Y.T. Zhu, Z.C. Zhang, W.P. Hu, Conductive metal-organic frameworks for electrocatalysis: achievements, challenges, and opportunities, *Wuli Huaxue Xuebao* 37 (2021) 2010025.
- [8] H. Li, F. Li, J. Yu, S. Cao, 2D/2D FeNi-LDH/g-C₃N₄ Hybrid photocatalyst for enhanced CO₂ photoreduction, *Wuli Huaxue Xuebao* 37 (2020) 2010073.
- [9] H. Jin, L. Xiong, X. Zhang, Y. Lian, S. Chen, Y. Lu, Z. Deng, Y. Peng, Cu-based catalyst derived from nitrogen-containing metal organic frameworks for electroreduction of CO₂, *Wuli Huaxue Xuebao* 37 (2020) 2006017.
- [10] Y.H. Sun, M.D. Gao, H. Li, L. Xu, Q. Xue, X.R. Wang, Y. Bai, C. Wu, Application of metal-organic frameworks to the interface of lithium metal batteries, *Wuli Huaxue Xuebao* 37 (2021) 2007048.
- [11] J. Wang, J. Li, G. Yan, M. Gao, X. Zhang, Preparation of a thickness-controlled Mg-MOFs-based magnetic graphene composite as a novel hydrophilic matrix for the effective identification of the glycopeptide in the human urine, *Nanoscale* 11 (2019) 3701–3709.
- [12] X. Zhu, J. Gu, J. Zhu, Y. Li, L. Zhao, J. Shi, Metal-organic frameworks with Boronic acid suspended and their implication for cis-diol moieties binding, *Adv. Funct. Mater.* 25 (2015) 3847–3854.
- [13] Y. Yang, Z. Shi, Y. Chang, X. Wang, L. Yu, C. Guo, J. Zhang, B. Bai, D. Sun, S. Fan, Surface molecularly imprinted magnetic MOFs: A novel platform coupled with magnet electrode for high throughput electrochemical sensing analysis of oxytetracycline in foods, *Food Chem.* 363 (2021) 130337.
- [14] J. Wen, Y. Li, J. Gao, Two-dimensional metal-organic frameworks and derivatives for electrocatalysis, *Chem. Res. Chin. Univ.* 36 (2020) 662–679.
- [15] J. Huang, J.-Q. Wu, B. Shao, B.-L. Lan, F.-J. Yang, Y. Sun, X.-Q. Tan, C.-T. He, Z. Zhang, Ion-induced delamination of layered bulk metal-organic frameworks into ultrathin nanosheets for boosting the oxygen evolution reaction, *ACS Sustain. Chem. Eng.* 8 (2020) 10554–10563.
- [16] C. Chang, W. Chen, Y. Chen, Y. Chen, F. Ding, C. Fan, H. Jin Fan, Z. Fan, C. Gong, Y. Gong, Q. He, X. Hong, S. Hu, W. Hu, W. Huang, Y. Huang, W. Ji, D. Li, L.-J. Li, Q. Li, L. Lin, C. Ling, M. Liu, N. Liu, Z. Liu, K. Ping Loh, J. Ma, F. Miao, H. Peng, M. Shao, L. Song, S. Su, S. Sun, C. Tan, Z. Tang, D. Wang, H. Wang, J. Wang, X. Wang, X. Wang, A.T.S. Wee, Z. Wei, Y. Wu, Z.-S. Wu, J. Xiong, Q. Xiong, W. Xu, P. Yin, H. Zeng, Z. Zeng, T. Zhai, H. Zhang, H. Zhang, Q. Zhang, T. Zhang, X. Zhang, L.-D. Zhao, M. Zhao, Y. Zhao, K.-G. Zhou, X. Zhou, Y. Zhou, H. Zhu, H. Zhang, Z. Liu, Recent progress on two-dimensional materials, *Wuli Huaxue Xuebao* 37 (2021) 2108017.
- [17] T.R. Cook, Y.R. Zheng, P.J. Stang, Metal-organic frameworks and self-assembled supramolecular coordination complexes: comparing and contrasting the design, synthesis, and functionality of metal-organic materials, *Chem. Rev.* 113 (2013) 734–777.
- [18] X. Tang, L. Zhao, W. Sun, Y. Wang, Two-dimensional metal-organic framework materials for energy conversion and storage, *J. Power Sources* 477 (2020) 228919.
- [19] A. Zavabeti, A. Jannat, L. Zhong, A.A. Haidry, Z. Yao, J.Z. Ou, Two-dimensional materials in large-areas: synthesis, properties and applications, *Nano-Micro Lett.* 12 (2020) 66.
- [20] X. Chia, M. Puma, Characteristics and performance of two-dimensional materials for electrocatalysis, *Nat. Catal.* 1 (2018) 909–921.
- [21] D. Huang, Y. Luo, S. Li, L. Liao, Y. Li, H. Chen, J. Ye, Recent advances in tuning the electronic structures of atomically dispersed M-N-C materials for efficient gas-involving electrocatalysis, *Mater. Horizons* 7 (2020) 970–986.
- [22] C. Chen, N. Suo, X.Q. Han, X.Q. He, Z.Y. Dou, Z.H. Lin, L.L. Cui, Tuning the morphology and electron structure of metal-organic framework-74 as bifunctional electrocatalyst for OER and HER using bimetallic collaboration strategy, *J. Alloys Compd.* 865 (2021) 158795.
- [23] Q. Hu, X. Huang, Z. Wang, G. Li, Z. Han, H. Yang, X. Ren, Q. Zhang, J. Liu, C. He, Unconventionally fabricating defect-rich NiO nanoparticles within ultrathin metal-organic framework nanosheets to enable high-output oxygen evolution, *J. Mater. Chem. A* 8 (2020) 2140–2146.
- [24] Q.Y. Jiang, C.H. Zhou, H.B. Meng, Y. Han, X.F. Shi, C.H. Zhan, R.F. Zhang, Two-dimensional metal-organic framework nanosheets: synthetic methodologies and electrocatalytic applications, *J. Mater. Chem. A* 8 (2020) 15271–15301.
- [25] G. Chang, H. Zhang, X.-Y. Yu, 2D metal-organic frameworks and their derivatives for the oxygen evolution reaction, *J. Alloys Compd.* 919 (2022) 165823.
- [26] J. Zhou, Y. Dou, A. Zhou, L. Shu, Y. Chen, J.-R. Li, Layered metal-organic framework-derived metal oxide/carbon nanosheet arrays for catalyzing the oxygen evolution reaction, *ACS Energy Lett.* 3 (2018) 1655–1661.
- [27] R. Dong, M. Pfeiffermann, H. Liang, Z. Zheng, X. Zhu, J. Zhang, X. Feng, Large-area, free-standing, two-dimensional supramolecular polymer single-layer sheets for highly efficient electrocatalytic hydrogen evolution, *Angew. Chem. Int. Ed. Engl.* 54 (2015) 12058–12063.
- [28] Q. Wang, Z. Liu, H. Zhao, H. Huang, H. Jiao, Y. Du, MOF-derived porous Ni₂P nanosheets as novel bifunctional electrocatalysts for the hydrogen and oxygen evolution reactions, *J. Mater. Chem. A* 6 (2018) 18720–18727.
- [29] J. Cheng, X. Yang, X. Yang, R. Xia, Y. Xu, W. Sun, J. Zhou, Hierarchical Ni₃S₂@2D Co MOF nanosheets as efficient hetero-electrocatalyst for hydrogen evolution reaction in alkaline solution, *Fuel Process. Technol.* 229 (2022) 107174.
- [30] Q. Liu, J. Chen, P. Yang, F. Yu, Z. Liu, B. Peng, Directly application of bimetallic 2D-MOF for advanced electrocatalytic oxygen evolution, *Int. J. Hydrog. Energy* 46 (2021) 416–424.
- [31] X. Zheng, X. Song, X. Wang, Z. Zhang, Z. Sun, Y. Guo, Nickel-copper bimetal organic framework nanosheets as a highly efficient catalyst for oxygen evolution reaction in alkaline media, *New J. Chem.* 42 (2018) 8346–8350.
- [32] N. Liu, Q.Q. Zhang, J.Q. Guan, A binuclear Co-based metal-organic framework towards efficient oxygen evolution reaction, *Chem. Commun.* 57 (2021) 5016–5019.
- [33] X. Wang, L. Zou, H. Fu, Y. Xiong, Z. Tao, J. Zheng, X. Li, Noble metal-free oxygen reduction reaction catalysts derived from prussian blue nanocrystals dispersed in polyaniline, *ACS Appl. Mater. Interfaces* 8 (2016) 8436–8444.
- [34] Z. Li, M. Shao, L. Zhou, Q. Yang, C. Zhang, M. Wei, D.G. Evans, X. Duan, Carbon-based electrocatalyst derived from bimetallic metal-organic framework arrays for high performance oxygen reduction, *Nano Energy* 25 (2016) 100–109.
- [35] P. De Luna, W. Liang, A. Mallick, O. Shekha, F.P. Garcia de Arquer, A.H. Proppe, P. Todorovic, S.O. Kelley, E.H. Sargent, M. Eddaoudi, Metal-organic framework thin films on high-curvature nanostructures toward tandem electrocatalysis, *ACS Appl. Mater. Interfaces* 10 (2018) 31225–31232.
- [36] J.X. Wu, W.W. Yuan, M. Xu, Z.Y. Gu, Ultrathin 2D nickel zeolitic imidazolate framework nanosheets for electrocatalytic reduction of CO₂, *Chem. Commun. (Cambridge, U. K.)* 55 (2019) 11634–11637.
- [37] X.X. Huang, Y.J. Ma, L.J. Zhi, Ultrathin nitrogenated carbon nanosheets with single-atom nickel as an efficient catalyst for electrochemical CO₂ reduction, *Wuli Huaxue Xuebao* 38 (2022) 2011050.
- [38] C. Lv, Y. Qian, C. Yan, Y. Ding, Y. Liu, G. Chen, G. Yu, Defect engineering metal-free polymeric carbon nitride electrocatalyst for effective nitrogen fixation under ambient conditions, *Angew. Chem. Int. Ed. Engl.* 57 (2018) 10246–10250.
- [39] L. Zhang, X. Ren, Y. Luo, X. Shi, A.M. Asiri, T. Li, X. Sun, Ambient NH₃ synthesis via electrochemical reduction of N₂ over cubic sub-micron SnO₂ particles, *Chem. Commun. (Cambridge, U. K.)*, 54 (2018) 12966–12969.
- [40] K. Sun, Y. Zhao, J. Yin, J. Jin, H. Liu, P. Xi, Surface modification of NiCo₂O₄ nanowires using organic ligands for overall water splitting, *Wuli Huaxue Xuebao* 38 (2021) 2107005.
- [41] B. Nohra, H. El Moll, L.M. Rodriguez Albelo, P. Mialane, J. Marrot, C. Mellot-Drazniak, M. O'Keeffe, R. Ngo Biboum, J. Lemaire, B. Keita, L. Nadjo, A. Dolbecq, Polyoxometalate-based metal organic frameworks (POMOFs): structural trends, energetics, and high electrocatalytic efficiency for hydrogen evolution reaction, *J. Am. Chem. Soc.* 133 (2011) 13363–13374.
- [42] D. Senthil Raja, H.-W. Lin, S.-Y. Lu, Synergistically well-mixed MOFs grown on nickel foam as highly efficient durable bifunctional electrocatalysts for overall water splitting at high current densities, *Nano Energy* 57 (2019) 1–13.
- [43] H.-W. Lin, D. Senthil Raja, X.-F. Chuah, C.-T. Hsieh, Y.-A. Chen, S.-Y. Lu, Bimetallic MOFs possessing hierarchical synergistic effects as high performance electrocatalysts for overall water splitting at high current densities, *Appl. Catal. B* 258 (2019) 118023.
- [44] H. Wang, Y. Li, Y. Li, B. He, R. Wang, Y. Gong, MOFs-derived hybrid nanosheet arrays of nitrogen-rich CoS₂ and nitrogen-doped carbon for efficient hydrogen evolution in both alkaline and acidic media, *Int. J. Hydrog. Energy* 43 (2018) 23319–23326.
- [45] L. Zhang, X. Wang, A. Li, X. Zheng, L. Peng, J. Huang, Z. Deng, H. Chen, Z. Wei, Rational construction of macroporous CoFeP triangular plate arrays from bimetal-organic frameworks as high-performance overall water-splitting catalysts, *J. Mater. Chem. A* 7 (2019) 17529–17535.
- [46] Y. Xu, W. Tu, B. Zhang, S. Yin, Y. Huang, M. Kraft, R. Xu, Nickel nanoparticles encapsulated in few-layer nitrogen-doped graphene derived from metal-organic frameworks as efficient bifunctional electrocatalysts for overall water splitting, *Adv. Mater.* 29 (2017) 1605957.
- [47] X.P. Yin, H.J. Wang, S.F. Tang, X.L. Lu, M. Shu, R. Si, T.B. Lu, Engineering the coordination environment of single-atom platinum anchored on graphdiyne for optimizing electrocatalytic hydrogen evolution, *Angew. Chem. Int. Ed. Engl.* 57 (2018) 9382–9386.
- [48] Y. Zhou, G. Gao, J. Kang, W. Chu, L.W. Wang, Computational screening of transition-metal single atom doped C₆N₄ monolayers as efficient electrocatalysts for water splitting, *Nanoscale* 11 (2019) 18169–18175.
- [49] H. Over, Fundamental studies of planar single-crystalline oxide model electrodes (RuO₂, IrO₂) for acidic water splitting, *ACS Catal.* 11 (2021) 8848–8871.
- [50] Z.A. Cui, R.H. Qi, First-principles simulation of oxygen evolution reaction (OER) catalytic performance of IrO₂ bulk-like structures: Nanosphere, nanowire and nanotube, *Appl. Surf. Sci.* 554 (2021) 149591.
- [51] Q.H. Liang, A. Bieberle-Hutter, G. Brocks, Anti-Ferromagnetic RuO₂: a stable and robust OER catalyst over a large range of surface terminations, *J. Phys. Chem. C* 126 (2022) 1337–1345.

- [52] K.A. Stoerzinger, O. Diaz-Morales, M. Kolb, R.R. Rao, R. Frydendal, L. Qiao, X.R. Wang, N.B. Halck, J. Rossmeisl, H.A. Hansen, T. Vegge, I.E.L. Stephens, M.T.M. Koper, Y. Shao-Horn, Orientation-dependent oxygen evolution on RuO₂ without lattice exchange, *ACS Energy Lett.* 2 (2017) 876–881.
- [53] J.Q. Guan, X. Bai, T.M. Tang, Recent progress and prospect of carbon-free single-site catalysts for the hydrogen and oxygen evolution reactions, *Nano Res.* 15 (2021) 818–837.
- [54] Y. Yang, J. Liu, Z. Wei, S. Wang, J. Ma, Transition metal-dinitrogen complex embedded graphene for nitrogen reduction reaction, *ChemCatChem* 11 (2019) 2821–2827.
- [55] Y. Xu, B. Li, S. Zheng, P. Wu, J. Zhan, H. Xue, Q. Xu, H. Pang, Ultrathin two-dimensional cobalt-organic framework nanosheets for high-performance electrocatalytic oxygen evolution, *J. Mater. Chem. A* 6 (2018) 22070–22076.
- [56] C. Cao, D.D. Ma, Q. Xu, X.T. Wu, Q.L. Zhu, Semisacrificial template growth of self-supporting MOF nanocomposite electrode for efficient electrocatalytic water oxidation, *Adv. Funct. Mater.* 29 (2018) 1807418.
- [57] Z.Q. Xue, K. Liu, Q.L. Liu, Y.L. Li, M.R. Li, C.Y. Su, N. Ogiwara, H. Kobayashi, H. Kitagawa, M. Liu, G.Q. Li, Missing-linker metal-organic frameworks for oxygen evolution reaction, *Nat. Commun.* 10 (2019) 5048.
- [58] H.X. Jia, Y.C. Yao, J.T. Zhao, Y.Y. Gao, Z.L. Luo, P.W. Du, A novel two-dimensional nickel phthalocyanine-based metal-organic framework for highly efficient water oxidation catalysis, *J. Mater. Chem. A* 6 (2018) 1188–1195.
- [59] J.-Y. Zhao, R. Wang, S. Wang, Y.-R. Lv, H. Xu, S.-Q. Zang, Metal-organic framework-derived Co₉S₈ embedded in N, O and S-tridoped carbon nanomaterials as an efficient oxygen bifunctional electrocatalyst, *J. Mater. Chem. A* 7 (2019) 7389–7395.
- [60] H. Wu, J. Wang, J. Yan, Z. Wu, W. Jin, MOF-derived two-dimensional N-doped carbon nanosheets coupled with Co-Fe-P-Se as efficient bifunctional OER/ORR catalysts, *Nanoscale* 11 (2019) 20144–20150.
- [61] W. Zang, A. Sumboja, Y. Ma, H. Zhang, Y. Wu, S. Wu, H. Wu, Z. Liu, C. Guan, J. Wang, S.J. Pennycook, Single Co atoms anchored in porous N-doped carbon for efficient zinc-air battery cathodes, *ACS Catal.* 8 (2018) 8961–8969.
- [62] X. Wen, Q. Zhang, J. Guan, Applications of metal-organic framework-derived materials in fuel cells and metal-air batteries, *Coord. Chem. Rev.* 409 (2020) 213214.
- [63] T.Y. Ma, S. Dai, M. Jaroniec, S.Z. Qiao, Metal-organic framework derived hybrid Co₃O₄-carbon porous nanowire arrays as reversible oxygen evolution electrodes, *J. Am. Chem. Soc.* 136 (2014) 13925–13931.
- [64] E.M. Miner, T. Fukushima, D. Sheberla, L. Sun, Y. Surendranath, M. Dinca, Electrochemical oxygen reduction catalysed by Ni₃(hexaiminotriphenylene)₂, *Nat. Commun.* 7 (2016) 10942.
- [65] M. Jahan, Z. Liu, K.P. Loh, A Graphene oxide and copper-centered metal organic framework composite as a tri-functional catalyst for HER, OER, and ORR, *Adv. Funct. Mater.* 23 (2013) 5363–5372.
- [66] J.Y. Cheon, T. Kim, Y. Choi, H.Y. Jeong, M.G. Kim, Y.J. Sa, J. Kim, Z. Lee, T.H. Yang, K. Kwon, O. Terasaki, G.G. Park, R.R. Adzic, S.H. Joo, Ordered mesoporous porphyrinic carbons with very high electrocatalytic activity for the oxygen reduction reaction, *Sci. Rep.* 3 (2013) 2715.
- [67] Y. Lian, W. Yang, C. Zhang, H. Sun, Z. Deng, W. Xu, L. Song, Z. Ouyang, Z. Wang, J. Guo, Y. Peng, Unpaired 3d electrons on atomically dispersed cobalt centres in coordination polymers regulate both oxygen reduction reaction (ORR) activity and selectivity for use in zinc-air batteries, *Angew. Chem. Int. Ed. Engl.* 59 (2020) 286–294.
- [68] J. Wei, Y. Hu, Y. Liang, B. Kong, J. Zhang, J. Song, Q. Bao, G.P. Simon, S.P. Jiang, H. Wang, Nitrogen-doped nanoporous carbon/graphene nano-sandwiches: synthesis and application for efficient oxygen reduction, *Adv. Funct. Mater.* 25 (2015) 5768–5777.
- [69] W.-Y. Zhi, Y.-T. Liu, S.-L. Shan, C.-J. Jiang, H. Wang, J.-X. Lu, Efficient electroreduction of CO₂ to C₂–C₃ products on Cu/Cu₂O@N-doped graphene, *J. CO₂ Util.* 50 (2021) 101594.
- [70] L. Majidi, A. Ahmadiparidari, N. Shan, S.N. Misal, K. Kumar, Z. Huang, S. Rastegar, Z. Hemmat, X. Zou, P. Zapol, J. Cabana, L.A. Curtiss, A. Salehi-Khojin, 2D copper tetrahydroxyquinone conductive metal-organic framework for selective CO₂ electrocatalysis at low overpotentials, *Adv. Mater.* 33 (2021) e2004393.
- [71] Y.-S. Cheng, X.-P. Chu, M. Ling, N. Li, K.-L. Wu, F.-H. Wu, H. Li, G. Yuan, X.-W. Wei, An MOF-derived copper@nitrogen-doped carbon composite: the synergistic effects of N-types and copper on selective CO₂ electroreduction, *Catal. Sci. Technol.* 9 (2019) 5668–5675.
- [72] H.-M. Liu, S.-H. Han, Y. Zhao, Y.-Y. Zhu, X.-L. Tian, J.-H. Zeng, J.-X. Jiang, B.Y. Xia, Y. Chen, Surfactant-free atomically ultrathin rhodium nanosheet nanoassemblies for efficient nitrogen electroreduction, *J. Mater. Chem. A* 6 (2018) 3211–3217.
- [73] M.-M. Shi, D. Bao, S.-J. Li, B.-R. Wulan, J.-M. Yan, Q. Jiang, Anchoring PdCu amorphous nanocluster on graphene for electrochemical reduction of N₂ to NH₃ under ambient conditions in aqueous solution, *Adv. Funct. Mater.* 8 (2018) 1800124.
- [74] X. Liu, Z. Wang, J. Zhao, J. Zhao, Y. Liu, Two-dimensional π-conjugated osmium bis(dithiolenes) complex (OsC₄S₄) as a promising electrocatalyst for ambient nitrogen reduction to ammonia, *Appl. Surf. Sci.* 487 (2019) 833–839.
- [75] M. Zhao, Y. Huang, Y. Peng, Z. Huang, Q. Ma, H. Zhang, Two-dimensional metal-organic framework nanosheets: synthesis and applications, *Chem. Soc. Rev.* 47 (2018) 6267–6295.
- [76] K. Zhao, W. Zhu, S. Liu, X. Wei, G. Ye, Y. Su, Z. He, Two-dimensional metal-organic frameworks and their derivatives for electrochemical energy storage and electrocatalysis, *Nanoscale Adv.* 2 (2020) 536–562.
- [77] Y. Peng, Y. Li, Y. Ban, H. Jin, W. Jiao, X. Liu, W. Yang, Membranes. Metal-organic framework nanosheets as building blocks for molecular sieving membranes, *Science* 346 (2014) 1356–1359.
- [78] S. Wu, L. Qin, K. Zhang, Z. Xin, S. Zhao, Ultrathin 2D metal-organic framework nanosheets prepared via sonication exfoliation of membranes from interfacial growth and exhibition of enhanced catalytic activity by their gold nanocomposites, *RSC Adv.* 9 (2019) 9386–9391.
- [79] J.H. Qin, H. Zhang, P. Sun, Y.D. Huang, Q. Shen, X.G. Yang, L.F. Ma, Ionic liquid induced highly dense assembly of porphyrin in MOF nanosheets for photodynamic therapy, *Dalton Trans.* 49 (2020) 17772–17778.
- [80] Q. Li, Q. Wang, Y. Li, X. Zhang, Y. Huang, 2D bimetallic Ni/Fe MOF nanosheet composites as a peroxidase-like nanozyme for colorimetric assay of multiple targets, *Anal. Methods* 13 (2021) 2066–2074.
- [81] C. Tan, K. Yang, J. Dong, Y. Liu, Y. Liu, J. Jiang, Y. Cui, Boosting enantioselectivity of chiral organocatalysts with ultrathin two-dimensional metal-organic framework nanosheets, *J. Am. Chem. Soc.* 141 (2019) 17685–17695.
- [82] Y. Liu, L. Liu, X. Chen, Y. Liu, Y. Han, Y. Cui, Single-Crystalline ultrathin 2D porous nanosheets of chiral metal-organic frameworks, *J. Am. Chem. Soc.* 143 (2021) 3509–3518.
- [83] D. Liu, B. Liu, C. Wang, W. Jin, Q. Zha, G. Shi, D. Wang, X. Sang, C. Ni, Ionic liquid-assisted exfoliation of two-dimensional metal-organic frameworks for luminescent sensing, *ACS Sustain. Chem. Eng.* 8 (2020) 2167–2175.
- [84] Q. Qiu, H. Chen, Z. You, Y. Feng, X. Wang, Y. Wang, Y. Ying, Shear exfoliated metal-organic framework nanosheet-enabled flexible sensor for real-time monitoring of superoxide anion, *ACS Appl. Mater. Interfaces* 12 (2020) 5429–5436.
- [85] N.A. Jose, H.C. Zeng, A.A. Lapkin, Scalable and precise synthesis of two-dimensional metal organic framework nanosheets in a high shear annular microreactor, *Chem. Eng. J.* 388 (2020) 124133.
- [86] N.A. Jose, J.J. Varghese, S.H. Mushrif, H.C. Zeng, A.A. Lapkin, Assembly of two-dimensional metal organic framework superstructures via solvent-mediated oriented attachment, *J. Phys. Chem. C* 125 (2021) 22837–22847.
- [87] S. Jiang, X. Shi, F. Sun, G. Zhu, Fabrication of crystalline microporous membrane from 2D MOF nanosheets for gas separation, *Chem. - Asian J.* 15 (2020) 2371–2378.
- [88] Y. Peng, Y. Li, Y. Ban, W. Yang, Two-Dimensional metal-organic framework nanosheets for membrane-based gas separation, *Angew. Chem. Int. Ed. Engl.* 56 (2017) 9757–9761.
- [89] K. Cheng, Y. Li, Z. Gao, F. Chen, C. You, B. Sun, Two-dimensional metal organic framework for effective gas absorption, *Inorg. Chem. Commun.* 101 (2019) 27–31.
- [90] A. Abherve, S. Manas-Valero, M. Clemente-Leon, E. Coronado, Graphene related magnetic materials: micromechanical exfoliation of 2D layered magnets based on bimetallic anilate complexes with inserted [Fe(III)(acac₂-trien)]⁺ and [Fe(III)(sal₂-trien)]⁺ molecules, *Chem. Sci.* 6 (2015) 4665–4673.
- [91] X. Wang, C. Chi, K. Zhang, Y. Qian, K.M. Gupta, Z. Kang, J. Jiang, D. Zhao, Reversed thermo-switchable molecular sieving membranes composed of two-dimensional metal-organic nanosheets for gas separation, *Nat. Commun.* 8 (2017) 14460.
- [92] J. Xie, Y. Wang, D. Zhang, C. Liang, W. Liu, Y. Chong, X. Yin, Y. Zhang, D. Gui, L. Chen, W. Tong, Z. Liu, J. Diwu, Z. Chai, S. Wang, Photo-exfoliation of a highly photo-responsive two-dimensional metal-organic framework, *Chem. Commun. (Cambridge, U. K.)*, 55 (2019) 11715–11718.
- [93] Y. Yang, H. Hou, G. Zou, W. Shi, H. Shuai, J. Li, X. Ji, Electrochemical exfoliation of graphene-like two-dimensional nanomaterials, *Nanoscale* 11 (2018) 16–33.
- [94] J. Huang, Y. Li, R.K. Huang, C.T. He, L. Gong, Q. Hu, L. Wang, Y.T. Xu, X.Y. Tian, S. Y. Liu, Z.M. Ye, F. Wang, D.D. Zhou, W.X. Zhang, J.P. Zhang, Electrochemical exfoliation of pillared-layer metal-organic framework to boost the oxygen evolution reaction, *Angew. Chem. Int. Ed. Engl.* 57 (2018) 4632–4636.
- [95] B. Liu, X. Wang, H. Liu, Y. Zhai, L. Li, H. Wen, 2D MOF with electrochemical exfoliated graphene for nonenzymatic glucose sensing: Central metal sites and oxidation potentials, *Anal. Chim. Acta* 1122 (2020) 9–19.
- [96] M.-F. Qin, Q.-Q. Mu, S.-S. Bao, X. Liang, Y. Peng, L.-M. Zheng, Chemically exfoliated semiconducting bimetallic porphyrinylphosphonate metal-organic layers for photocatalytic CO₂ reduction under visible light, *ACS Appl. Energy Mater.* 4 (2021) 4319–4326.
- [97] Y. Ding, Y.P. Chen, X. Zhang, L. Chen, Z. Dong, H.L. Jiang, H. Xu, H.C. Zhou, Controlled intercalation and chemical exfoliation of layered metal-organic frameworks using a chemically labile intercalating agent, *J. Am. Chem. Soc.* 139 (2017) 9136–9139.
- [98] J. Fonseca, S. Choi, Electro- and photoelectro-catalysts derived from bimetallic amorphous metal-organic frameworks, *Catal. Sci. Technol.* 10 (2020) 8265–8282.
- [99] Z.H. Wang, H.H. Jin, T. Meng, K. Liao, W.Q. Meng, J.L. Yang, D.P. He, Y.L. Xiong, S.C. Mu, Fe, Cu-Coordinated ZIF-derived carbon framework for efficient oxygen reduction reaction and zinc-air batteries, *Adv. Funct. Mater.* 28 (2018) 1802596.

- [100] I.S. Aminiun, Z. Pu, X. Liu, K.A. Owusu, H.G.R. Monestel, F.O. Boakye, H. Zhang, S. Mu, Multifunctional Mo-N/C@MoS₂ electrocatalysts for HER, OER, ORR, and Zn-Air batteries, *Adv. Funct. Mater.* 27 (2017) 1702300.
- [101] J. Su, W. Wu, Z. Li, W. Li, Self-crystallization of uniformly oriented zeolitic imidazolate framework films at air-water interfaces, *Dalton Trans.* 48 (2019) 11196–11199.
- [102] W. Wu, M. Jia, J. Su, Z. Li, W. Li, Air–water interfacial synthesis of metal–organic framework hollow fiber membranes for water purification, *AIChE J.* 66 (2020) e16238.
- [103] R. Makiura, O. Konovalov, Interfacial growth of large-area single-layer metal–organic framework nanosheets, *Sci. Rep.* 3 (2013) 2506.
- [104] S. Sakaida, K. Otsubo, O. Sakata, C. Song, A. Fujiwara, M. Takata, H. Kitagawa, Crystalline coordination framework endowed with dynamic gate-opening behaviour by being downsized to a thin film, *Nat. Chem.* 8 (2016) 377–383.
- [105] X.H. Liu, Y.W. Yang, X.M. Liu, Q. Hao, L.M. Wang, B. Sun, J. Wu, D. Wang, Confined synthesis of oriented two-dimensional Ni₃(hexaiminotriphenylene) 2 films for electrocatalytic oxygen evolution reaction, *Langmuir* 36 (2020) 7528–7532.
- [106] T. Rodenas, I. Luz, G. Prieto, B. Seoane, H. Miro, A. Corma, F. Kapteijn, I.X.F.X. Llabres, J. Gascon, Metal–organic framework nanosheets in polymer composite materials for gas separation, *Nat. Mater.* 14 (2015) 48–55.
- [107] Y.P. Wu, W. Zhou, J. Zhao, W.W. Dong, Y.Q. Lan, D.S. Li, C. Sun, X. Bu, Surfactant-assisted phase-selective synthesis of new cobalt MOFs and their efficient electrocatalytic hydrogen evolution reaction, *Angew. Chem. Int. Ed. Engl.* 56 (2017) 13001–13005.
- [108] A. Pustovarenko, M.G. Goesten, S. Sachdeva, M. Shan, Z. Amghouz, Y. Belmabkhout, A. Dikhtiarenko, T. Rodenas, D. Keskin, I.K. Voets, B.M. Weckhuysen, M. Eddaoudi, L. de Smet, E.J.R. Sudholter, F. Kapteijn, B. Seoane, J. Gascon, Nanosheets of nonlayered aluminum metal–organic frameworks through a surfactant-assisted method, *Adv. Mater.* 30 (2018) e1707234.
- [109] Y. Sun, M. Amsler, S. Goedecker, A. Caravella, M. Yoshida, M. Kato, Surfactant-assisted synthesis of large Cu-BTC MOF single crystals and their potential utilization as photodetectors, *CrystEngComm* 21 (2019) 3948–3953.
- [110] S.L. Griffin, M.L. Briuglia, J.H. Ter Horst, R.S. Forgan, Assessing crystallisation kinetics of Zr Metal–organic frameworks through turbidity measurements to inform rapid microwave-assisted synthesis, *Chem. Eur. J.* 26 (2020) 6910–6918.
- [111] H. Jiang, W. Zhang, X. Kang, Z. Cao, X. Chen, Y. Liu, Y. Cui, Topology-based functionalization of robust chiral Zr-based metal–organic frameworks for catalytic enantioselective hydrogenation, *J. Am. Chem. Soc.* 142 (2020) 9642–9652.
- [112] J. Xu, X. Zhu, X. Jia, From low- to high-crystallinity bimetal–organic framework nanosheet with highly exposed boundaries: an efficient and stable electrocatalyst for oxygen evolution reaction, *ACS Sustain. Chem. Eng.* 7 (2019) 16629–16639.
- [113] L. Zhuang, L. Ge, H. Liu, Z. Jiang, Y. Jia, Z. Li, D. Yang, R.K. Hocking, M. Li, L. Zhang, X. Wang, X. Yao, Z. Zhu, A surfactant-free and scalable general strategy for synthesizing ultrathin two-dimensional metal–organic framework nanosheets for the oxygen evolution reaction, *Angew. Chem. Int. Ed. Engl.* 58 (2019) 13565–13572.
- [114] Q. Liu, X. Li, Y. Wen, Q. Xu, X.T. Wu, Q.L. Zhu, Twofold Interpenetrated 2D MOF nanosheets generated by an instant in situ exfoliation method: morphology control and fluorescent sensing, *Adv. Mater. Interfaces* 7 (2020) 2000813.
- [115] Y. Qian, Z. Hu, X. Ge, S. Yang, Y. Peng, Z. Kang, Z. Liu, J.Y. Lee, D. Zhao, A metal-free ORR/OER bifunctional electrocatalyst derived from metal–organic frameworks for rechargeable Zn-Air batteries, *Carbon* 111 (2017) 641–650.
- [116] Q. Wang, R. Yang, J. Li, Y. Yang, Y. Wu, X. Zhou, G. Ma, S. Ren, 2D DUT-8(Ni)-derived Ni@C nanosheets for efficient hydrogen evolution, *J. Solid State Electrochem.* 24 (2020) 2461–2467.
- [117] L. Huang, X. Zhang, Y. Han, Q. Wang, Y. Fang, S. Dong, In situ synthesis of ultrathin metal–organic framework nanosheets: a new method for 2D metal-based nanoporous carbon electrocatalysts, *J. Mater. Chem. A* 5 (2017) 18610–18617.
- [118] Y. Lin, G. Chen, H. Wan, F. Chen, X. Liu, R. Ma, 2D free-standing nitrogen-doped Ni-Ni₃S₂@carbon nanoplates derived from metal–organic frameworks for enhanced oxygen evolution reaction, *Small* 15 (2019) e1900348.
- [119] J.T. Ren, Y.L. Zheng, K. Yuan, L. Zhou, K. Wu, Y.W. Zhang, Self-templated synthesis of Co₃O₄ hierarchical nanosheets from a metal–organic framework for efficient visible-light photocatalytic CO₂ reduction, *Nanoscale* 12 (2020) 755–762.
- [120] F.L. Li, Q. Shao, X. Huang, J.P. Lang, Nanoscale trimetallic metal–organic frameworks enable efficient oxygen evolution electrocatalysis, *Angew. Chem. Int. Ed. Engl.* 57 (2018) 1888–1892.
- [121] W. Sun, Y. Du, G. Wu, G. Gao, H. Zhu, J. Shen, K. Zhang, G. Cao, Constructing metallic zinc–cobalt sulfide hierarchical core–shell nanosheet arrays derived from 2D metal–organic-frameworks for flexible asymmetric supercapacitors with ultrahigh specific capacitance and performance, *J. Mater. Chem. A* 7 (2019) 7138–7150.
- [122] B. Yuan, C. Li, L. Guan, K. Li, Y. Lin, Prussian blue analog nanocubes tuning synthesis of coral-like Ni₃S₂@MIL-53(NiFeCo) core-shell nanowires array and boosting oxygen evolution reaction, *J. Power Sources* 451 (2020) 227295.
- [123] P. He, Y. Xie, Y. Dou, J. Zhou, A. Zhou, X. Wei, J.R. Li, Partial sulfuration of a 2D MOF array for highly efficient oxygen evolution reaction, *ACS Appl. Mater. Interfaces* 11 (2019) 41595–41601.
- [124] K. Jayaramulu, D.P. Dubal, A. Schneemann, V. Ranc, C. Perez-Reyes, J. Stráská, Š. Kment, M. Otyepka, R.A. Fischer, R. Zbořil, Shape-assisted 2D MOF/graphene derived hybrids as exceptional lithium-ion battery electrodes, *Adv. Funct. Mater.* 29 (2019) 1902539.
- [125] Y. Yang, S. Li, W. Huang, S. Duan, P. Si, L. Ci, Rational construction of ternary ZnNiP arrayed structures derived from 2D MOFs for advanced hybrid supercapacitors and Zn batteries, *Electrochim. Acta* 387 (2021) 138548.
- [126] Y. Zhou, L. Zheng, D. Yang, H. Yang, Q. Lu, Q. Zhang, L. Gu, X. Wang, Enhancing CO₂ electrocatalysis on 2D porphyrin-based metal–organic framework nanosheets coupled with visible-light, *Small Methods* 5 (2020) 2000991.
- [127] X. Zhao, J. Bai, X. Bo, L. Guo, A novel electrochemical sensor based on 2D CuTCPP nanosheets and platelet ordered mesoporous carbon composites for hydroxylamine and chlorogenic acid, *Anal. Chim. Acta* 1075 (2019) 71–80.
- [128] T. Li, B. Ding, V. Malgras, J. Na, Z. Qin, X. Lu, Y. Bando, H. Nara, Z.A. Allothman, J. Wang, Y. Yamauchi, Hollow carbon architectures with mesoporous shells via self-sacrificial templating strategy using metal–organic frameworks, *Chem. Eng. J.* 420 (2021) 127635.
- [129] W.-C. Hu, Y. Shi, Y. Zhou, C. Wang, M.R. Younis, J. Pang, C. Wang, X.-H. Xia, Plasmonic hot charge carriers activated Ni centres of metal–organic frameworks for the oxygen evolution reaction, *J. Mater. Chem. A* 7 (2019) z10601–z10609.
- [130] C. Pan, Z. Liu, M. Huang, 2D iron-doped nickel MOF nanosheets grown on nickel foam for highly efficient oxygen evolution reaction, *Appl. Surf. Sci.* 529 (2020) 147201.
- [131] B. Shao, H.S. Chen, C.A.J. Cui, J. Li, R. Gonge, Research Progress on improvement of conductivity of MOFs and their application in biosensors: a review, *Chem. Lett.* 50 (2021) 714–723.
- [132] C. Li, L.L. Zhang, J.Q. Chen, X.L. Li, J.W. Sun, J.W. Zhu, X. Wang, Y.S. Fu, Recent development and applications of electrical conductive MOFs, *Nanoscale* 13 (2021) 485–509.
- [133] F.D. Wang, B.C. Wang, B.B. Hao, C.X. Zhang, Q.L. Wang, Designable guest-molecule encapsulation in metal–organic frameworks for proton conductivity, *Chem. Eur. J.* 28 (2022) e202103732.
- [134] B. Liu, X. Wang, Y. Zhai, Z. Zhang, H. Liu, L. Li, H. Wen, Facile preparation of well conductive 2D MOF for nonenzymatic detection of hydrogen peroxide: relationship between electrocatalysis and metal center, *J. Electroanal. Chem.* 858 (2020) 113804.
- [135] Q. Xia, H. Liu, M. Jin, L. Lai, Y. Qiu, H. Zhai, H. Li, X. Liu, Catalysts confined inside CNTs derived from 2D metal–organic frameworks for electrolysis, *Nanoscale* 12 (2020) 8969–8974.
- [136] R. Zhang, L. Jiao, W. Yang, G. Wan, H.-L. Jiang, Single-atom catalysts templated by metal–organic frameworks for electrochemical nitrogen reduction, *J. Mater. Chem. A* 7 (2019) 26371–26377.
- [137] T. Rodenas, S. Beeg, I. Spanos, S. Neugebauer, F. Girgsdies, G. Algara-Siller, P.P. M. Schlerer, P. Jakes, N. Pfänder, M. Willinger, M. Greiner, G. Prieto, R. Schlögl, S. Heumann, 2D metal organic framework-graphitic carbon nanocomposites as precursors for high-performance O₂-evolution electrocatalysts, *Adv. Energy Mater.* 8 (2018) 1802404.
- [138] Y. Wen, H. Rong, T. Zhan, A 2D MOF derived core-shell structured nanocomposite as effective electrocatalyst for oxygen reduction reaction, *J. Electroanal. Chem.* 833 (2019) 454–461.
- [139] F. Cheng, Z. Li, L. Wang, B. Yang, J. Lu, L. Lei, T. Ma, Y. Hou, In situ identification of the electrocatalytic water oxidation behavior of a nickel-based metal–organic framework nanoarray, *Mater. Horizons* 8 (2021) 556–564.
- [140] W.X. Li, W. Fang, W. Chen, K. Dinh, H. Ren, L. Zhao, C.T. Liu, Q.Y. Yan, Bimetal-MOF nanosheets as efficient bifunctional electrocatalysts for oxygen evolution and nitrogen reduction reaction, *J. Mater. Chem. A* 8 (2020) 3658–3666.
- [141] X. Zhang, R. Lin, X. Meng, W. Li, F. Chen, J. Hou, Iron phthalocyanine/two-dimensional metal–organic framework composite nanosheets for enhanced alkaline hydrogen evolution, *Inorg. Chem.* 60 (2021) 9987–9995.
- [142] T.M. Tang, Z.L. Wang, J.Q. Guan, A review of defect engineering in two-dimensional materials for electrocatalytic hydrogen evolution reaction, *Chin. J. Catal.* 43 (2022) 636–678.
- [143] J. Ding, T. Fan, K. Shen, Y. Li, Electrochemical synthesis of amorphous metal hydroxide microarrays with rich defects from MOFs for efficient electrocatalytic water oxidation, *Appl. Catal. B* 292 (2021) 120174.
- [144] C. Liu, X. Shen, G. Johnson, Y. Zhang, C. Zhang, J. Chen, L. Li, C. Sheehan, Z. Peng, S. Zhang, Two-dimensional metal organic framework nanosheets as bifunctional catalyst for electrochemical and photoelectrochemical water oxidation, *Front. Chem.* 8 (2020) 604239.
- [145] X. Bai, J. Guan, MXenes for electrocatalysis applications: modification and hybridization, *Chinese J. Catal.* 43 (2022) 2057–2090.
- [146] L. Zhang, L. Nie, S. Zhang, Z. Dong, Q. Zhou, Z. Zhang, G.-B. Pan, 2D conductive MOF modified MXene nanosheets for poly(vinylidene fluoride) nanocomposite with high permittivity, *Mater. Lett.* 314 (2022) 131820.
- [147] X. Liu, F. Liu, X. Zhao, L.-Z. Fan, Constructing MOF-derived CoP-NC@MXene sandwich-like composite by in-situ intercalation for enhanced lithium and sodium storage, *J. Materiomics* 8 (2022) 30–37.
- [148] S. Zhao, H. Wu, Y. Li, Q. Li, J. Zhou, X. Yu, H. Chen, K. Tao, L. Han, Core-shell assembly of carbon nanofibers and a 2D conductive metal–organic framework as a flexible free-standing membrane for high-performance supercapacitors, *Inorg. Chem. Front.* 6 (2019) 1824–1830.
- [149] T. Si, X. Lu, H. Zhang, X. Liang, S. Wang, Y. Guo, Fabrication of two-dimensional metal–organic framework nanosheets/PDA composites as

- mixed-mode stationary phase for chromatographic separation, *Microchim. Acta* 188 (2021) 360.
- [150] F. Schwotzer, I. Senkovska, V. Bon, S. Lochmann, J.D. Evans, D. Pohl, B. Rellinghaus, S. Kaskel, Solvent-assisted delamination of layered copper dithiophene-dicarboxylate (DUT-134), *Inorg. Chem. Front.* 8 (2021) 3308–3316.
- [151] R. Hardian, S. Dissegna, A. Ullrich, P.L. Llewellyn, M.V. Coulet, R.A. Fischer, Tuning the properties of MOF-808 via defect engineering and metal nanoparticle encapsulation, *Chem. Eur. J.* 27 (2021) 6804–6814.
- [152] Z. Chen, D. Guo, K. An, B. Zhang, X. Zhang, B. Zhao, Efficient and fair resource allocation scheme for cognitive satellite-terrestrial networks, *IEEE Access* 7 (2019) 145124–145133.
- [153] N. Heidary, D. Chartrand, A. Guet, N. Kornienko, Rational incorporation of defects within metal-organic frameworks generates highly active electrocatalytic sites, *Chem. Sci.* 12 (2021) 7324–7333.
- [154] Z. Lu, K. Wang, Y. Cao, Y. Li, D. Jia, Amino-functionalized iron-based MOFs modified with 2D FeCo(OH) hybrids for boosting oxygen evolution, *J. Alloys Compd.* 871 (2021) 159580.
- [155] W. Chen, Y. Zhang, G. Chen, R. Huang, Y. Wu, Y. Zhou, Y. Hu, K.K. Ostrikov, Hierarchical porous bimetal-sulfide bi-functional nanocatalysts for hydrogen production by overall water electrolysis, *J. Colloid Interface Sci.* 560 (2020) 426–435.
- [156] J. Wang, L. Han, B. Huang, Q. Shao, H.L. Xin, X. Huang, Amorphization activated ruthenium-tellurium nanorods for efficient water splitting, *Nat. Commun.* 10 (2019) 5692.
- [157] W. Huang, J. Tang, F. Diao, C. Engelbrekt, J. Ulstrup, X. Xiao, K. Mølhave, Recent progress of two-dimensional metal-organic frameworks and their derivatives for oxygen evolution electrocatalysis, *ChemElectroChem* 7 (2020) 4695–4712.
- [158] H.Y. Zheng, D. Xie, H. Li, S.Y. Wu, B.W. Qin, Z. Cui, X.Y. Zhang, J.P. Zhang, 2D metal-organic framework derived Co₃O₄ for the oxygen evolution reaction and high-performance lithium-ion batteries, *ChemNanoMat* 6 (2020) 1770–1775.
- [159] B.Y. Xu, Y. Zhang, Y.C. Pi, Q. Shao, X.Q. Huang, Research progress of nickel-based metal-organic frameworks and their derivatives for oxygen evolution catalysis, *Wuli Huaxue Xuebao* 37 (2021) 2009074.
- [160] D.Q. Yan, L. Zhang, Z.P. Chen, W.P. Xiao, X.F. Yang, Nickel-based metal-organic framework-derived bifunctional electrocatalysts for hydrogen and oxygen evolution reactions, *Wuli Huaxue Xuebao* 37 (2021) 2009054.
- [161] A. Goswami, D. Ghosh, V.V. Chernyshev, A. Dey, D. Pradhan, K. Biradha, 2D MOFs with Ni(II), Cu(II), and Co(II) as efficient oxygen evolution electrocatalysts: rationalization of catalytic performance vs structure of the MOFs and potential of the redox couples, *ACS Appl. Mater. Interfaces* 12 (2020) 33679–33689.
- [162] H. Jia, Y. Yao, J. Zhao, Y. Gao, Z. Luo, P. Du, A novel two-dimensional nickel phthalocyanine-based metal-organic framework for highly efficient water oxidation catalysis, *J. Mater. Chem. A* 6 (2018) 1188–1195.
- [163] P. Thangasamy, S. Shanmuganathan, V. Subramanian, A NiCo-MOF nanosheet array based electrocatalyst for the oxygen evolution reaction, *Nanoscale Adv.* 2 (2020) 2073–2079.
- [164] A. Joshi, A. Gaur, P. Sood, M. Singh, One-pot crystallization of 2D and 3D cobalt-based metal-organic frameworks and their high-performance electrocatalytic oxygen evolution, *Inorg. Chem.* 60 (2021) 12685–12690.
- [165] C. Yang, W.-J. Cai, B.-B. Yu, H. Qiu, M.-L. Li, L.-W. Zhu, Z. Yan, L. Hou, Y.-Y. Wang, Performance enhancement of oxygen evolution reaction through incorporating bimetallic electrocatalysts in two-dimensional metal-organic frameworks, *Catal. Sci. Technol.* 10 (2020) 3897–3903.
- [166] W. Li, W. Fang, C. Wu, K.N. Dinh, H. Ren, L. Zhao, C. Liu, Q. Yan, Bimetal-MOF nanosheets as efficient bifunctional electrocatalysts for oxygen evolution and nitrogen reduction reaction, *J. Mater. Chem. A* 8 (2020) 3658–3666.
- [167] M. Lu, Y. Li, P. He, J. Cong, D. Chen, J. Wang, Y. Wu, H. Xu, J. Gao, J. Yao, Bimetallic metal-organic framework nanosheets as efficient electrocatalysts for oxygen evolution reaction, *J. Solid State Chem.* 272 (2019) 32–37.
- [168] C. Zhang, Z. Chen, Y. Lian, Y. Chen, Q. Li, Y. Gu, Y. Lu, Z. Deng, Y. Peng, Copper-based conductive metal organic framework in-situ grown on copper foam as a bifunctional electrocatalyst, *Wuli Huaxue Xuebao* 35 (2019) 1404–1411.
- [169] Q. Liu, J. Chen, F. Yu, J. Wu, Z. Liu, B. Peng, Multifunctional book-like CuCo-MOF for highly sensitive glucose detection and electrocatalytic oxygen evolution, *New J. Chem.* 45 (2021) 16714–16721.
- [170] N.K. Shrestha, S.A. Patil, S. Cho, Y. Jo, H. Kim, H. Im, Cu-Fe-NH₂ based metal-organic framework nanosheets via drop-casting for highly efficient oxygen evolution catalysts durable at ultrahigh currents, *J. Mater. Chem. A* 8 (2020) 24408–24418.
- [171] J. Ma, B. Lu, S. Wang, W. He, X. Bai, T. Wang, X. Zhang, Y. Li, L. Zhang, J. Chen, F. Meng, Y. Fu, MOF-derived CuCoNi trimetallic hybrids as efficient oxygen evolution reaction electrocatalysts, *New J. Chem.* 44 (2020) 2459–2464.
- [172] Y. Li, M. Lu, P. He, Y. Wu, J. Wang, D. Chen, H. Xu, J. Gao, J. Yao, Bimetallic metal-organic framework-derived nanosheet-assembled nanoflower electrocatalysts for efficient oxygen evolution reaction, *Chem. - Asian J.* 14 (2019) 1590–1594.
- [173] W. Chen, Y. Zhang, G. Chen, R. Huang, Y. Zhou, Y. Wu, Y. Hu, K. Ostrikov, Mesoporous cobalt-iron-organic frameworks: a plasma-enhanced oxygen evolution electrocatalyst, *J. Mater. Chem. A* 7 (2019) 3090–3100.
- [174] X. Hu, P. Tan, R. Dong, M. Jiang, L. Lu, Y. Wang, H. Liu, Y. Liu, J. Xie, J. Pan, A novel metal-organic framework intermediated synthesis of heterogeneous CoS₂/CoS porous nanosheets for enhanced oxygen evolution reaction, *Energy Technol.* 9 (2021) 2000961.
- [175] X. Bai, Z. Duan, B. Nan, L. Wang, T. Tang, J. Guan, Unveiling the active sites of ultrathin Co-Fe layered double hydroxides for the oxygen evolution reaction, *Chinese J. Catal.* 43 (2022) 2240–2248.
- [176] J.-M. Huo, Y. Wang, J. Meng, X.-Y. Zhao, Q.-G. Zhai, Y.-C. Jiang, M.-C. Hu, S.-N. Li, Y. Chen, π - π interaction directed 2D FeNi-LDH nanosheets from 2D Hofmann-MOFs for the oxygen evolution reaction, *J. Mater. Chem. A* 10 (2022) 1815–1820.
- [177] R. Yu, D. Liu, M. Yuan, Y. Wang, C. Ye, J. Li, Y. Du, Universal MOF-Mediated synthesis of 2D CoNi-based layered triple hydroxides electrocatalyst for efficient oxygen evolution reaction, *J. Colloid Interface Sci.* 602 (2021) 612–618.
- [178] K. Ge, S. Sun, Y. Zhao, K. Yang, S. Wang, Z. Zhang, J. Cao, Y. Yang, Y. Zhang, M. Pan, L. Zhu, Facile synthesis of two-dimensional iron/cobalt metal-organic framework for efficient oxygen evolution electrocatalysis, *Angew. Chem. Int. Ed.* 60 (2021) 12097–12102.
- [179] X. Mu, H. Yuan, H. Jing, F. Xia, J. Wu, X. Gu, C. Chen, J. Bao, S. Liu, S. Mu, Superior electrochemical water oxidation in vacancy defect-rich 1.5 nm ultrathin trimetal-organic framework nanosheets, *Appl. Catal. B* 295 (2021) 120095.
- [180] D. Zhu, J. Liu, L. Wang, Y. Du, Y. Zheng, K. Davey, S.-Z. Qiao, A 2D metal-organic framework/Ni(OH)₂ heterostructure for an enhanced oxygen evolution reaction Electronic supplementary information (ESI) available. See DOI: 10.1039/c8nr09680e, *Nanoscale* 11 (2019) 3599–3605.
- [181] Y. Song, Y. Yang, S. Mo, D. Guo, L. Liu, Fast construction of (Fe₂O₃)_x@Ni-MOF heterostructure nanosheets as highly active catalyst for water oxidation, *J. Alloys Compd.* 892 (2022) 162149.
- [182] J. Wang, Y. Jiang, C. Liu, Y. Wu, B. Liu, W. Jiang, H. Li, G. Che, In situ growth of hierarchical bimetal-organic frameworks on nickel-iron foam as robust electrodes for the electrocatalytic oxygen evolution reaction, *J. Colloid Interface Sci.* 614 (2022) 532–537.
- [183] Y. Lin, M. Zhang, L. Zhao, L. Wang, D. Cao, Y. Gong, Ru doped bimetallic phosphide derived from 2D metal organic framework as active and robust electrocatalyst for water splitting, *Appl. Surf. Sci.* 536 (2021) 147952.
- [184] K. Srinivas, Y. Lu, Y. Chen, W. Zhang, D. Yang, FeNi₃-Fe₃O₄ heterogeneous nanoparticles anchored on 2D MOF nanosheets/1D matrix as highly efficient bifunctional electrocatalysts for wafer splitting, *ACS Sustain. Chem. Eng.* 8 (2020) 3820–3831.
- [185] C.-F. Du, Q. Song, Q. Liang, X. Zhao, J. Wang, R. Zhi, Y. Wang, H. Yu, The passive effect of MXene on electrocatalysis: a case of Ti₃C₂Tx/CoNi-MOF nanosheets for oxygen evolution reaction, *ChemNanoMat* 7 (2021) 539–544.
- [186] W.-C. Hu, Y. Shi, Y. Zhou, C. Wang, M.R. Younis, J. Pang, C. Wang, X.-H. Xia, Plasmonic hot charge carriers activated Ni centres of metal-organic frameworks for the oxygen evolution reaction, *J. Mater. Chem. A* 7 (2019) 10601–10609.
- [187] C. Cui, J. Wang, Z. Luo, J. Wang, C. Li, Z. Li, MOF-mediated synthesis of monodisperse Co(OH)₂ flower-like nanosheets for enhanced oxygen evolution reaction, *Electrochim. Acta* 273 (2018) 327–334.
- [188] Q. Zha, F. Yuan, G. Qin, Y. Ni, Cobalt-based MOF-on-MOF two-dimensional heterojunction nanostructures for enhanced oxygen evolution reaction electrocatalytic activity, *Inorg. Chem.* 59 (2020) 1295–1305.
- [189] J. Meng, Y. Zhou, H. Chi, K. Li, J. Wan, Z. Hu, Bimetallic porphyrin MOF anchored onto rGO nanosheets as a highly efficient 2D electrocatalyst for oxygen evolution reaction in alkaline conditions, *Chemistryselect* 4 (2019) 8661–8670.
- [190] J. Greeley, T.F. Jaramillo, J. Bonde, I.B. Chorkendorff, J.K. Nørskov, Computational high-throughput screening of electrocatalytic materials for hydrogen evolution, *Nat. Mater.* 5 (2006) 909–913.
- [191] C.G. Morales-Guio, L.A. Stern, X.L. Hu, Nanostructured hydrotreating catalysts for electrochemical hydrogen evolution, *Chem. Soc. Rev.* 43 (2014) 6555–6569.
- [192] N. Contreras-Pereda, F. Moghzi, J. Baselga, H. Zhong, J. Janczak, J. Soleimannejad, R. Dong, D. Ruiz-Molina, Ultrasound-assisted exfoliation of a layered 2D coordination polymer with HER electrocatalytic activity, *Ultrason. Sonochem.* 70 (2021) 105292.
- [193] Y.-S. Li, J.-W. Yi, J.-H. Wei, Y.-P. Wu, B. Li, S. Liu, C. Jiang, H.-G. Yu, D.-S. Li, Three 2D polyhalogenated Co(II)-based MOFs: Syntheses, crystal structure and electrocatalytic hydrogen evolution reaction, *J. Solid State Chem.* 281 (2020) 121052.
- [194] Y. Xu, S. Yu, T. Ren, S. Liu, Z. Wang, X. Li, L. Wang, H. Wang, Hydrophilic/aerophobic hydrogen-evolving electrode: NiRu-Based metal-organic framework nanosheets in situ grown on conductive substrates, *ACS Appl. Mater. Interfaces* 12 (2020) 34728–34735.
- [195] L. Qi, Y.-Q. Su, Z. Xu, G. Zhang, K. Liu, M. Liu, E.J.M. Hensen, R.-Y.-Y. Lin, Hierarchical 2D yarn-ball like metal-organic framework NiFe(dobpdc) as bifunctional electrocatalyst for efficient overall electrocatalytic water splitting, *J. Mater. Chem. A* 8 (2020) 22974–22982.
- [196] Y. Sun, S. Ding, S. Xu, J. Duan, S. Chen, Metallic two-dimensional metal-organic framework arrays for ultrafast water splitting, *J. Power Sources* 494 (2021) 229733.
- [197] H. Zhang, H. Guo, J. Ren, X. Jin, X. Li, R. Song, Synergistic engineering of morphology and electronic structure in constructing metal-organic framework-derived Ru doped cobalt-nickel oxide heterostructure towards efficient alkaline hydrogen evolution reaction, *Chem. Eng. J.* 426 (2021) 131300.

- [198] Y. Wang, A. Wang, Z. Xue, L. Wang, X. Li, G. Wang, Ultrathin metal-organic framework nanosheet arrays and derived self-supported electrodes for overall water splitting, *J. Mater. Chem. A* 9 (2021) 22597–22602.
- [199] S.S. Li, J.R. Sun, J.Q. Guan, Strategies to improve electrocatalytic and photocatalytic performance of two-dimensional materials for hydrogen evolution reaction, *Chin. J. Catal.* 42 (2021) 511–556.
- [200] D. Zhu, J. Liu, Y. Zhao, Y. Zheng, S.Z. Qiao, Engineering 2D metal-organic framework/MoS₂ interface for enhanced alkaline hydrogen evolution, *Small* 15 (2019) e1805511.
- [201] Q. Li, Y. Zhou, C. Chen, Q. Liu, J. Huo, H. Yi, Building CoP/Co-MOF heterostructure in 2D nanosheets for improving electrocatalytic hydrogen evolution over a wide pH range, *J. Electroanal. Chem.* 895 (2021) 115514.
- [202] X. Shi, P. Yang, Y. Cao, C. Dai, W. Ye, L. Zheng, Z. Zhao, J. Wang, H. Zheng, Ultrathin 2D flower-like CoP@C with the active (211) facet for efficient electrocatalytic water splitting, *CrystEngComm* 23 (2021) 1777–1784.
- [203] L. Qi, Y.-Q. Su, Z. Xu, G. Zhang, K. Liu, M. Liu, E.J.M. Hensen, R.-Y.-Y. Lin, Hierarchical 2D yarn-ball like metal-organic framework NiFe(dobpdc) as bifunctional electrocatalyst for efficient overall electrocatalytic water splitting, *J. Mater. Chem. A* 8 (2020) 22974–22982.
- [204] K. Rui, G. Zhao, M. Lao, P. Cui, X. Zheng, X. Zheng, J. Zhu, W. Huang, S.X. Dou, W. Sun, Direct hybridization of noble metal nanostructures on 2D metal-organic framework nanosheets to catalyze hydrogen evolution, *Nano Lett.* 19 (2019) 8447–8453.
- [205] D. Wang, Y. Zhang, T. Fei, C. Mao, Y. Song, Y. Zhou, G. Dong, NiCoP/NF 1D/2D biomimetic architecture for markedly enhanced overall water splitting, *ChemElectroChem* 8 (2021) 3064–3072.
- [206] Y. Zhou, Y. Chen, M. Wei, H. Fan, X. Liu, Q. Liu, Y. Liu, J. Cao, L. Yang, 2D MOF-derived porous NiCoSe nanosheet arrays on Ni foam for overall water splitting, *CrystEngComm* 23 (2021) 69–81.
- [207] K. Chhetri, A. Muthurasu, B. Dahal, T. Kim, T. Mukhiya, S.H. Chae, T.H. Ko, Y.C. Choi, H.Y. Kim, Engineering the abundant heterointerfaces of integrated bimetallic sulfide-coupled 2D MOF-derived mesoporous CoS₂ nanoarray hybrids for electrocatalytic water splitting, *Mater. Today Nano* 17 (2022) 100146.
- [208] N. Yao, T. Tan, F. Yang, G. Cheng, W. Luo, Well-aligned metal-organic framework array-derived CoS₂ nanosheets toward robust electrochemical water splitting, *Mater. Chem. Front.* 2 (2018) 1732–1738.
- [209] D. Zhu, J. Liu, Y. Zhao, Y. Zheng, S.-Z. Qiao, Engineering 2D metal-organic framework/MoS₂ interface for enhanced alkaline hydrogen evolution, *Small* 15 (2019) 1805511.
- [210] Y. Li, B. Jia, B. Chen, Q. Liu, M. Cai, Z. Xue, Y. Fan, H.-P. Wang, C.-Y. Su, G. Li, MOF-derived Mn doped porous CoP nanosheets as efficient and stable bifunctional electrocatalysts for water splitting, *Dalton Trans.* 47 (2018) 14679–14685.
- [211] Z. Pan, N. Pan, L. Chen, J. He, M. Zhang, Flower-like MOF-derived Co-N-doped carbon composite with remarkable activity and durability for electrochemical hydrogen evolution reaction, *Int. J. Hydrog. Energy* 44 (2019) 30075–30083.
- [212] M. Zhu, Q. Ma, S.-Y. Ding, Y.-Z. Zhao, W.-Q. Song, H.-P. Ren, X.-Z. Song, Z.-C. Miao, A molybdenum disulfide and 2D metal-organic framework nanocomposite for improved electrocatalytic hydrogen evolution reaction, *Mater. Lett.* 239 (2019) 155–158.
- [213] R. Dong, Z. Zheng, D.C. Tranca, J. Zhang, N. Chandrasekhar, S. Liu, X. Zhuang, G. Seifert, X. Feng, Immobilizing molecular metal dithiolene-diamine complexes on 2D metal-organic frameworks for electrocatalytic H₂ production, *Chem. Eur. J.* 23 (2017) 2255–2260.
- [214] H.H. Do, L. Quyet Van, M.A. Tekalgne, T. Anh Vy, T.H. Lee, S.H. Hong, S.M. Han, S.H. Ahn, Y.J. Kim, H.W. Jang, S.Y. Kim, Metal-organic framework-derived MoS_x composites as efficient electrocatalysts for hydrogen evolution reaction, *J. Alloys Compd.*, 852 (2021) 156952.
- [215] Z. Chen, Y. Cui, C. Ye, L. Liu, X. Wu, Y. Sun, W. Xu, D. Zhu, Highly conductive cobalt perthiolated coronene complex for efficient hydrogen evolution, *Chem. Eur. J.* 26 (2020) 12868–12873.
- [216] G. Yilmaz, T. Yang, Y. Du, X. Yu, Z.P. Feng, L. Shen, G.W. Ho, Stimulated electrocatalytic hydrogen evolution activity of MOF-Derived MoS₂ basal domains via charge injection through surface functionalization and heteroatom doping, *Adv. Sci.* 6 (2019) 1900140.
- [217] H. Li, F. Ke, J. Zhu, MOF-derived ultrathin cobalt phosphide nanosheets as efficient bifunctional hydrogen evolution reaction and oxygen evolution reaction electrocatalysts, *Nanomaterials* 8 (2018) 89.
- [218] J.S. Qin, D.Y. Du, W. Guan, X.J. Bo, Y.F. Li, L.P. Guo, Z.M. Su, Y.Y. Wang, Y.Q. Lan, H.C. Zhou, Ultrastable polymolybdate-based metal-organic frameworks as highly active electrocatalysts for hydrogen generation from water, *J. Am. Chem. Soc.* 137 (2015) 7169–7177.
- [219] B. Lv, X.L. Li, K. Guo, J. Ma, Y.Z. Wang, H.T. Lei, F. Wang, X.T. Jin, Q.X. Zhang, W. Zhang, R. Long, Y.J. Xiong, U.P. Apfel, R. Cao, Controlling oxygen reduction selectivity through steric effects: electrocatalytic two-electron and four-electron oxygen reduction with cobalt porphyrin atropisomers, *Angew. Chem. Int. Ed.* 60 (2021) 12742–12746.
- [220] A. Radwan, H.H. Jin, D.P. He, S.C. Mu, Design engineering, synthesis protocols, and energy applications of MOF-derived electrocatalysts, *Nano-Micro Lett.* 13 (2021) 132.
- [221] R. Iqbal, S. Ali, G. Yasin, S. Ibraheem, M. Tabish, M. Hamza, H. Chen, H. Xu, J. Zeng, W. Zhao, A novel 2D Co₃(HADQ)2 metal-organic framework as a highly active and stable electrocatalyst for acidic oxygen reduction, *Chem. Eng. J.* 430 (2022) 132642.
- [222] H. Xia, J. Zhang, Z. Yang, S. Guo, S. Guo, Q. Xu, 2D MOF nanoflake-assembled spherical microstructures for enhanced supercapacitor and electrocatalysis performances, *Nano-Micro Lett.* 9 (2017) 43.
- [223] H. Yoon, S. Lee, S. Oh, H. Park, S. Choi, M. Oh, Synthesis of bimetallic conductive 2D metal-organic framework (Cox Niy -CAT) and its mass production: enhanced electrochemical oxygen reduction activity, *Small* 15 (2019) e1805232.
- [224] K. Huang, S. Guo, R. Wang, S. Lin, N. Hussain, H. Wei, B. Deng, Y. Long, M. Lei, H. Tang, H. Wu, Two-dimensional MOF/MOF derivative arrays on nickel foam as efficient bifunctional coupled oxygen electrodes, *Chin. J. Catal.* 41 (2020) 1754–1760.
- [225] M. Wang, N. Zhang, Y. Feng, Z. Hu, Q. Shao, X. Huang, Partially pyrolyzed binary metal-organic framework nanosheets for efficient electrochemical hydrogen peroxide synthesis, *Angew. Chem., Int. Ed. Engl.* 59 (2020) 14373–14377.
- [226] L. Zheng, S. Yu, X. Lu, W. Fan, B. Chi, Y. Ye, X. Shi, J. Zeng, X. Li, S. Liao, Two-Dimensional bimetallic Zn/Fe-metal-organic framework (MOF)-derived porous carbon nanosheets with a high density of single/paired Fe atoms as high-performance oxygen reduction catalysts, *ACS Appl. Mater. Interfaces* 12 (2020) 13878–13887.
- [227] S. Wan, J. Wu, D. Wang, H. Liu, Z. Zhang, J. Ma, C. Wang, Co/N-doped carbon nanotube arrays grown on 2D MOFs-derived matrix for boosting the oxygen reduction reaction in alkaline and acidic media, *Chin. Chem. Lett.* 32 (2021) 816–821.
- [228] I.S. Amiin, X. Liu, Z. Pu, W. Li, Q. Li, J. Zhang, H. Tang, H. Zhang, S. Mu, From 3D ZIF nanocrystals to Co-Nx/C nanorod array electrocatalysts for ORR, OER, and Zn-Air batteries, *Adv. Funct. Mater.* 28 (2018) 1704638.
- [229] T.T. Wang, Z.K. Kou, S.C. Mu, J.P. Liu, D.P. He, I.S. Amiin, W. Meng, K. Zhou, Z. X. Luo, S. Chaemchuen, F. Verpoort, 2D Dual-Metal Zeolitic-Imidazolate-Framework-(ZIF)-derived bifunctional air electrodes with ultrahigh electrochemical properties for rechargeable zinc-air batteries, *Adv. Funct. Mater.* 28 (2018) 1705048.
- [230] F. Lu, K. Fan, L. Cui, Y. Yang, W. Wang, G. Zhang, C. Wang, Q. Zhang, B. Li, L. Zong, L. Wang, Cu-N₄ single atoms derived from metal-organic frameworks with trapped nitrogen-rich molecules and their use as efficient electrocatalysts for oxygen reduction reaction, *Chem. Eng. J.* 431 (2022) 133242.
- [231] Y. Hou, T. Huang, Z. Wen, S. Mao, S. Cui, J. Chen, Metal-organic framework-derived nitrogen-doped core-shell-structured porous Fe/Fe₃C@C nanoboxes supported on graphene sheets for efficient oxygen reduction reactions, *Adv. Energy Mater.* 4 (2014) 1400337.
- [232] Y. Chen, S. Ji, Y. Wang, J. Dong, W. Chen, Z. Li, R. Shen, L. Zheng, Z. Zhuang, D. Wang, Y. Li, Isolated single iron atoms anchored on N-doped porous carbon as an efficient electrocatalyst for the oxygen reduction reaction, *Angew. Chem. Int. Ed. Engl.* 56 (2017) 6937–6941.
- [233] B.Y. Guan, L. Yu, X.W. Lou, A dual-metal-organic-framework derived electrocatalyst for oxygen reduction, *Energy Environ. Sci.* 9 (2016) 3092–3096.
- [234] J. Guo, Y. Li, Y. Cheng, L. Dai, Z. Xiang, Highly efficient oxygen reduction reaction electrocatalysts synthesized under nanospace confinement of metal-organic framework, *ACS Nano* 11 (2017) 8379–8386.
- [235] T. Liu, P. Zhao, X. Hua, W. Luo, S. Chen, G. Cheng, An Fe–N–C hybrid electrocatalyst derived from a bimetal-organic framework for efficient oxygen reduction, *J. Mater. Chem. A* 4 (2016) 11357–11364.
- [236] W. Gu, L. Hu, J. Li, E. Wang, Hybrid of g-C₃N₄ assisted metal-organic frameworks and their derived high-efficiency oxygen reduction electrocatalyst in the whole pH range, *ACS Appl. Mater. Interfaces* 8 (2016) 35281–35288.
- [237] L. Huang, X. Zhang, Y. Han, Q. Wang, Y. Fang, S. Dong, In situ synthesis of ultrathin metal-organic framework nanosheets: a new method for 2D metal-based nanoporous carbon electrocatalysts, *J. Mater. Chem. A* 5 (2017) 18610–18617.
- [238] L. Lin, X. Du, J. Wang, H. Chen, X. He, W. Fang, Y. Li, Z. Chen, L. Zhao, High-pressure vapor-solid transformation of 2D template to derive 2D Co-N-C electrocatalysts for oxygen reduction reaction, *Nanotechnology* 33 (2022) 105601.
- [239] T. Zhan, S. Lu, H. Rong, W. Hou, H. Teng, Y. Wen, Metal-organic-framework-derived Co/nitrogen-doped porous carbon composite as an effective oxygen reduction electrocatalyst, *J. Mater. Sci.* 53 (2018) 6774–6784.
- [240] F. Wang, Y. Xu, Y. Wang, Z. Liang, R. Zhang, Y. Wang, H. Zhang, W. Zhang, R. Cao, H. Zheng, Space-confined construction of two-dimensional nitrogen-doped carbon with encapsulated bimetallic nanoparticles as oxygen electrocatalysts, *ChemComm* 57 (2021) 8190–8193.
- [241] M.A. Ahsan, T. He, K. Eid, A.M. Abdullah, M.F. Sanad, A. Aldalbahi, B. Alvarado-Tenorio, A. Du, A.R.P. Santiago, J.C. Novoron, Controlling the interfacial charge polarization of MOF-derived 0D–2D vdW architectures as a unique strategy for bifunctional oxygen electrocatalysis, *ACS Appl. Mater. Interfaces* 14 (2022) 3919–3929.
- [242] D. Chen, J. Yu, Z. Cui, Q. Zhang, X. Chen, J. Sui, H. Dong, L. Yu, L. Dong, Hierarchical architecture derived from two-dimensional zeolitic imidazolate frameworks as an efficient metal-based bifunctional oxygen electrocatalyst for rechargeable Zn-air batteries, *Electrochim. Acta* 331 (2020) 135394.
- [243] H. Li, M. Zhang, W. Zhou, J. Duan, W. Jin, Ultrathin 2D catalysts with N-coordinated single Co atom outside Co cluster for highly efficient Zn-air battery, *Chem. Eng. J.* 421 (2021) 129719.

- [244] K. Zhao, S. Liu, G. Ye, X. Wei, Y. Su, W. Zhu, Z. Zhou, Z. He, Ultrasmall 2D CoxZn_{2-x}(Benzimidazole)₄ metal-organic framework nanosheets and their derived Co nanodots@Co, N-codoped graphene for efficient oxygen reduction reaction, *ChemSuschem* 13 (2020) 1556–1567.
- [245] J. Li, W. Xia, J. Tang, H. Tan, J. Wang, Y.V. Kaneti, Y. Bando, T. Wang, J. He, Y. Yamauchi, MOF nanoleaves as new sacrificial templates for the fabrication of nanoporous Co-N-x/C electrocatalysts for oxygen reduction, *Nanoscale Horiz.* 4 (2019) 1006–1013.
- [246] L. Yan, Y. Xu, P. Chen, S. Zhang, H. Jiang, L. Yang, Y. Wang, L. Zhang, J. Shen, X. Zhao, L. Wang, A freestanding 3D heterostructure film stitched by MOF-derived carbon nanotube microsphere superstructure and reduced graphene oxide sheets: a superior multifunctional electrode for overall water splitting and Zn-Air batteries, *Adv. Mater.* 32 (2020) 2003313.
- [247] H. Zhong, K.H. Ly, M. Wang, Y. Krupskaya, X. Han, J. Zhang, J. Zhang, V. Kataev, B. Buechner, I.M. Weidinger, S. Kaskel, P. Liu, M. Chen, R. Dong, X. Feng, A phthalocyanine-based layered two-dimensional conjugated metal-organic framework as a highly efficient electrocatalyst for the oxygen reduction reaction, *Angew. Chem. Int. Ed.* 58 (2019) 10677–10682.
- [248] T.M. Tang, Z.L. Wang, J.Q. Guan, Optimizing the electrocatalytic selectivity of carbon dioxide reduction reaction by regulating the electronic structure of single-atom M-N-C materials, *Adv. Funct. Mater.* 32 (2022) 2111504.
- [249] Z.Z. Qin, J. Wu, B. Li, T.M. Su, H.B. Ji, Ultrathin layered catalyst for photocatalytic reduction of CO₂, *Wuli Huaxue Xuebao* 37 (2021) 2005027.
- [250] W.J. Zhang, Y. Hu, L.B. Ma, G.Y. Zhu, Y.R. Wang, X.L. Xue, R.P. Chen, S.Y. Yang, Z. Jin, Progress and perspective of electrocatalytic CO₂ reduction for renewable carbonaceous fuels and chemicals, *Adv. Sci.* 5 (2018) 1700275.
- [251] H. Zhong, M. Ghorbani-Asl, K.H. Ly, J. Zhang, J. Ge, M. Wang, Z. Liao, D. Makarov, E. Zschech, E. Brunner, I.M. Weidinger, J. Zhang, A.V. Krasheninnikov, S. Kaskel, R. Dong, X. Feng, Synergistic electroreduction of carbon dioxide to carbon monoxide on bimetallic layered conjugated metal-organic frameworks, *Nat. Commun.* 11 (2020) 1409.
- [252] L. Xie, X.P. Zhang, B. Zhao, P. Li, J. Qi, X. Guo, B. Wang, H. Lei, W. Zhang, U.P. Apfel, R. Cao, Enzyme-inspired iron porphyrins for improved electrocatalytic oxygen reduction and evolution reactions, *Angew. Chem. Int. Ed.* 60 (2021) 7576–7581.
- [253] X.L. Li, H.T. Lei, L.S. Xie, N. Wang, W. Zhang, R. Cao, Metalloporphyrins as catalytic models for studying hydrogen and oxygen evolution and oxygen reduction reactions, *Acc. Chem. Res.* 55 (2022) 878–892.
- [254] X. Li, X.P. Zhang, M. Guo, B. Lv, K. Guo, X. Jin, W. Zhang, Y.M. Lee, S. Fukuzumi, W. Nam, R. Cao, Identifying intermediates in electrocatalytic water oxidation with a manganese corrole complex, *J. Am. Chem. Soc.* 143 (2021) 14613–14621.
- [255] X. Li, B. Lv, X.P. Zhang, X. Jin, K. Guo, D. Zhou, H. Bian, W. Zhang, U.P. Apfel, R. Cao, Introducing water-network-assisted proton transfer for boosted electrocatalytic hydrogen evolution with cobalt corrole, *Angew. Chem. Int. Ed.* 61 (2022) e202114310.
- [256] X.D. Zhang, S.Z. Hou, J.X. Wu, Z.Y. Gu, Two-dimensional metal-organic framework nanosheets with cobalt-porphyrins for high-performance CO₂ electroreduction, *Chem. - Eur. J.* 26 (2020) 1604–1611.
- [257] J.D. Yi, R. Xie, Z.L. Xie, G.L. Chai, T.F. Liu, R.P. Chen, Y.B. Huang, R. Cao, Highly selective CO₂ electroreduction to CH₄ by in situ generated Cu₂O single-type sites on a conductive MOF: stabilizing key intermediates with hydrogen bonding, *Angew. Chem., Int. Ed. Engl.* 59 (2020) 23641–23648.
- [258] Y. Xiao, D. Chen, R. Chen, Mechanistic study of efficient producing CO₂ electroreduction via 2D metal-organic frameworks M₃(2,3,6,7,10,11-hexamino)triphenylene₂ surface, *Electrochim. Acta* 378 (2021) 138028.
- [259] Y. Tian, C. Zhu, L. Yan, J. Zhao, Z. Su, Two-dimensional π -conjugated metal bis(dithiolene) nanosheets as promising electrocatalysts for carbon dioxide reduction: a computational study, *J. Mater. Chem. A* 7 (2019) 15341–15346.
- [260] Y. Tian, Y. Wang, L. Yan, J. Zhao, Z. Su, Electrochemical reduction of carbon dioxide on the two-dimensional M₃(Hexamino)triphenylene₂ sheet: a computational study, *Appl. Surf. Sci.* 467–468 (2019) 98–103.
- [261] J. Liu, D. Yang, Y. Zhou, G. Zhang, G. Xing, Y. Liu, Y. Ma, O. Terasaki, S. Yang, L. Chen, Tricycloquinazoline-based 2D conductive metal-organic frameworks as promising electrocatalysts for CO₂ reduction, *Angew. Chem., Int. Ed. Engl.* 60 (2021) 14473–14479.
- [262] F. Li, G.H. Gu, C. Choi, P. Kolla, S. Hong, T.S. Wu, Y.L. Soo, J. Masa, S. Mukerjee, Y.S. Jung, J.S. Qiu, Z.Y. Sun, Highly stable two-dimensional bismuth metal-organic frameworks for efficient electrochemical reduction of CO₂, *Appl. Catal., B* 277 (2020) 119241.
- [263] I. Ledezma-Yanez, E.P. Gallent, M.T.M. Koper, F. Calle-Vallejo, Structure-sensitive electroreduction of acetaldehyde to ethanol on copper and its mechanistic implications for CO and CO₂ reduction, *Catal. Today* 262 (2016) 90–94.
- [264] S. Hanselman, M.T.M. Koper, F. Calle-Vallejo, Computational comparison of late transition metal (100) surfaces for the electrocatalytic reduction of CO to C₂ species, *ACS Energy Lett.* 3 (2018) 1062–1067.
- [265] A.R. Woldu, Z. Huang, P. Zhao, L. Hu, D. Astruc, Electrochemical CO₂ reduction (CO₂RR) to multi-carbon products over copper-based catalysts, *Coord. Chem. Rev.* 454 (2022) 214340.
- [266] K. Xiang, F. Shen, Y. Fu, L. Wu, Z. Wang, H. Yi, X. Liu, P. Wang, M. Liu, Z. Lin, H. Liu, Boosting CO₂ electroreduction towards C₂⁺ products via CO* intermediate manipulation on copper-based catalysts, *Environ. Sci.: Nano* 9 (2022) 911–953.
- [267] E.L. Clark, A.T. Bell, Direct observation of the local reaction environment during the electrochemical reduction of CO₂, *J. Am. Chem. Soc.* 140 (2018) 7012–7020.
- [268] D.H. Nam, O.S. Bushuyev, J. Li, P. De Luna, A. Seifitokaldani, C.T. Dinh, F.P. Garcia de Arquer, Y. Wang, Z. Liang, A.H. Proppe, C.S. Tan, P. Todorovic, O. Shekhah, C.M. Gabardo, J.W. Jo, J. Choi, M.J. Choi, S.W. Baek, J. Kim, D. Sinton, S.O. Kelley, M. Eddaoudi, E.H. Sargent, Metal-organic frameworks mediate Cu coordination for selective CO₂ electroreduction, *J. Am. Chem. Soc.* 140 (2018) 11378–11386.
- [269] Z. Ma, D. Wu, X. Han, H. Wang, L. Zhang, Z. Gao, F. Xu, K. Jiang, Ultrasonic assisted synthesis of Zn-Ni bi-metal MOFs for interconnected Ni-N-C materials with enhanced electrochemical reduction of CO₂, *J. CO₂ Util.* 32 (2019) 251–258.
- [270] J.-D. Yi, D.-H. Si, R. Xie, Q. Yin, M.-D. Zhang, Q. Wu, G.-L. Chai, Y.-B. Huang, R. Cao, Conductive two-dimensional phthalocyanine-based metal-organic framework nanosheets for efficient electroreduction of CO₂, *Angew. Chem. Int. Ed.* 60 (2021) 17108–17114.
- [271] I. Hod, M.D. Sampson, P. Deria, C.P. Kubiak, O.K. Farha, J.T. Hupp, Porphyrin-based metal-organic framework films as high-surface concentration, heterogeneous catalysts for electrochemical reduction of CO₂, *ACS Catal.* 5 (2015) 6302–6309.
- [272] Z.F. Xin, J.J. Liu, X.J. Wang, K.J. Shen, Z.B. Yuan, Y.F. Chen, Y.Q. Lan, Implanting polypyrrole in metal-porphyrin MOFs: enhanced electrocatalytic performance for CO₂RR, *ACS Appl. Mater. Interfaces* 13 (2021) 54949–54956.
- [273] Z. Xin, Y.-R. Wang, Y. Chen, W.-L. Li, L.-Z. Dong, Y.-Q. Lan, Metallocene implanted metalloporphyrin organic framework for highly selective CO₂ electroreduction, *Nano Energy* 67 (2020) 104233.
- [274] B.-X. Dong, S.-L. Qian, F.-Y. Bu, Y.-C. Wu, L.-G. Feng, Y.-L. Teng, W.-L. Liu, Z.-W. Li, Electrochemical reduction of CO₂ to CO by a heterogeneous catalyst of Fe-Porphyrin-based metal-organic framework, *ACS Appl. Energy Mater.* 1 (2018) 4662–4669.
- [275] X.D. Zhang, L.R. Huang, J.X. Wu, Z.Y. Gu, Enhancing selectivity through decrypting the uncoordinated zirconium sites in MOF electrocatalysts, *Chem. Commun.* 57 (2021) 5191–5194.
- [276] N. Kornienko, Y. Zhao, C.S. Kley, C. Zhu, D. Kim, S. Lin, C.J. Chang, O.M. Yaghi, P. Yang, Metal-organic frameworks for electrocatalytic reduction of carbon dioxide, *J. Am. Chem. Soc.* 137 (2015) 14129–14135.
- [277] L. Ye, J. Liu, Y. Gao, C. Gong, M. Addicoat, T. Heine, C. Wöll, L. Sun, Highly oriented MOF thin film-based electrocatalytic device for the reduction of CO₂ to CO exhibiting high faradaic efficiency, *J. Mater. Chem. A* 4 (2016) 15320–15326.
- [278] X.C. Kang, Q.G. Zhu, X.F. Sun, J.Y. Hu, J.L. Zhang, Z.M. Liu, B.X. Han, Highly efficient electrochemical reduction of CO₂ to CH₄ in an ionic liquid using a metal-organic framework cathode, *Chem. Sci.* 7 (2016) 266–273.
- [279] J.R. Zhai, Q.L. Kang, Q.Y. Liu, D.W. Lai, Q.Y. Lu, F. Gao, In-situ generation of In₂O₃ nanoparticles inside In Co(CN)₆ quasi-metal-organic-framework nanotubes for efficient electroreduction of CO₂ to formate, *J. Colloid Interface Sci.* 608 (2022) 1942–1950.
- [280] Q. Cui, G. Qin, W. Wang, G. K. R. A. Du, Q. Sun, Mo-based 2D MOF as a highly efficient electrocatalyst for reduction of N₂ to NH₃: a density functional theory study, *J. Mater. Chem. A*, 7 (2019) 14510–14518.
- [281] X. Lv, W. Wei, H. Wang, F. Li, B. Huang, Y. Dai, T. Jacob, Nitrogen-free TMS₄-centers in metal-organic frameworks for ammonia synthesis, *J. Mater. Chem. A* 8 (2020) 20047–20053.
- [282] H.K. Lee, C.S.L. Koh, Y.H. Lee, C. Liu, I.Y. Phang, X. Han, C.-K. Tsung, X.Y. Ling, Favoring the unfavored: selective electrochemical nitrogen fixation using a reticular chemistry approach, *Sci. Adv.* 4 (2018) eaar3208.
- [283] C. Zhang, D. Wang, Y. Wan, R. Lv, S. Li, B. Li, X. Zou, S. Yang, Vanadium carbide with periodic anionic vacancies for effective electrocatalytic nitrogen reduction, *Mater. Today* 40 (2020) 18–25.
- [284] S. Luo, X. Li, W. Gao, H. Zhang, M. Luo, An MOF-derived C@NiO@Ni electrocatalyst for N₂ conversion to NH₃ in alkaline electrolytes, *Sustain. Energy Fuels* 4 (2020) 164–170.
- [285] Y.P. Lv, S.B. Duan, Y.C. Zhu, P. Yin, R.M. Wang, Enhanced OER performances of Au@NiCo₂S₄ core-shell heterostructure, *Nanomaterials* 10 (2020) 611.
- [286] R. Dong, Z. Zheng, D.C. Tranca, J. Zhang, N. Chandrasekhar, S. Liu, X. Zhuang, G. Seifert, X. Feng, Immobilizing molecular metal dithiolene-diamine complexes on 2D metal-organic frameworks for electrocatalytic H₂ production, *Chem. Eur. J.* 23 (2017) 2255–2260.
- [287] X. Zhang, J. Luo, H.-F. Lin, P. Tang, J.R. Morante, J. Arbiol, K. Wan, B.-W. Mao, L.-M. Liu, J. Fransaer, Tailor-made metal-nitrogen-carbon bifunctional electrocatalysts for rechargeable Zn-air batteries via controllable MOF units, *Energy Stor. Mater.* 17 (2019) 46–61.
- [288] Y. Luo, M. Li, Y. Dai, X. Zhang, R. Zhao, F. Jiang, C. Ling, Y. Huang, Screening of effective NRR electrocatalysts among the Si-based MSi₂N₄ (M = Ti, Zr, Hf, V, Nb, Ta, Cr, Mo, and W) monolayers, *J. Mater. Chem. A* 9 (2021) 15217–15225.
- [289] R. Wang, C. He, W. Chen, L. Fu, C. Zhao, J. Huo, C. Sun, Design strategies of two-dimensional metal-organic frameworks toward efficient electrocatalysts for N₂ reduction: cooperativity of transition metals and organic linkers, *Nanoscale* 13 (2021) 19247–19254.
- [290] Y.M. Li, L. Li, R. Huang, Y.H. Wen, Computational screening of MBene monolayers with high electrocatalytic activity for the nitrogen reduction reaction, *Nanoscale* 13 (2021) 15002–15009.